Freie Universität Berlin

HZB Helmholtz Zentrum Berlin

Ultrafast Electron Dynamics in Transition Metal Complexes Studied in Solution by Means of Time-Resolved XUV Photoemission Spectroscopy

Im Fachbereich Physik der Freien Universität Berlin
eingereichte Dissertation

zur Erlangung des akademischen Grades
eines Doktors der Naturwissenschaften (Dr. rer. nat.)

vorgelegt von

Alexandre Moguilevski

Berlin 2017

Gutachter:

1. Prof. Dr. Karsten Heyne
   Freie Universität Berlin
2. Dr. Iain Wilkinson
   Helmholtz-Zentrum Berlin

Tag der Disputation: 12.03.2018

Abbreviations

ATI	above-threshold ionization
BBO	barium borate
CCD	charge-coupled device
CMA	cylindrical mirror analyzer
DFG	difference frequency generation
DFT	discrete Fourier-transformation
DLD	delayline detector
EAL	electron attenuation length
ESA	excited state absorption
FWHM	full width at half maximum
GSB	ground state bleach
GVD	group velocity dispersion
HHG	high harmonic generation
HPLC	High-performance liquid chromatography
HS	high-spin
IC	internal conversion
IMFP	inelastic mean free path
IR	infrared
ISC	intersystem crossing
LAPE	laser-assisted photoemission effect
LC	ligand centered
LF	ligand field
LMCT	ligand-to-metal charge transfer
LMT	liquid microjet technique
LS	low-spin
MC	metal centered
MCP	multichannel plate
MLCT	metal-to-ligand charge transfer
MPI	multiphoton ionization
NC	nonlinear crystal
OLED	organic light-emitting diode

OPA	optical parametric amplifier
PES	photoemission spectroscopy
PMA	plane mirror analyzer
SCO	spin crossover
SFG	sum frequency generation
SHG	second harmonic generation
THG	third harmonic generation
TOF	time-of-flight
UV	ultraviolet
WAM	wide-angle mode
XANES	X-Ray absorption near edge structure
XAS	X-Ray absorption spectroscopy
XUV	extreme ultraviolet

Table of contents

1 Introduction

The knowledge of the electronic structure of atoms and molecules is the key to understanding the chemical and physical properties of matter. This makes studies of the electronic structure of fundamental importance for the natural sciences. Different spectroscopic methods have been established to facilitate these studies, such as absorption, fluorescence, and photoemission spectroscopies that employ radiation in the optical and X-ray energy range. The electron photoemission spectroscopy (PES) is one of the most powerful methods in revealing the electronic structure, since it allows us to directly observe the projection of the electron charge density distribution among the populated energy levels to the continuum. The concept of PES is based on the photo-electric effect, the discovery of which was appreciated by two Nobel Prizes in physics, won by Albert Einstein in 1921 and by Robert A. Millikan in 1923. The methodology of PES was developed by another Nobel Prize winner, Kai Siegbahn, in the late 50s. Besides other different experimental techniques, which were developed and applied during the last 60 years, PES has been widely applied by many research groups to conduct studies on gas, solid, and liquid samples. The latter type of experiments was technically the most challenging task, since ultrahigh vacuum conditions are required for unperturbed photoelectron detection. The pioneering study on liquids was performed by Hans and Kai Siegbahn and co-workers in the early 70s, who reported the first photoemission spectrum of liquid formamide [1]. Later, this challenge was overcome by application of the liquid microjet technique developed by Faubel in 1988 [2].

However, the knowledge of the static electronic structure alone is not sufficient for a complete characterization of the chemical processes. Given the fact that some chemical processes occur on extremely short time scales in the sub-picosecond or femtosecond range, ultrafast time-resolved methods are necessary to reveal the vibronic dynamics. The development of ultrashort laser pulses and the pump-probe experimental technique enables us to monitor and to characterize the ultrafast chemical processes. The pump-probe method usually involves two synchronized coherent light pulses. The first pulse initiates changes in the sample, while the second pulse arrives to the sample with adjustable time delay and generates the detectable signal. This signal carries the information about the quantum state of the studied system and, thus, one can follow the evolution of the electron dynamics initially induced by the first pulse. This technique can

be used e.g. to study molecular vibrations, which usually occurs on a sub-picosecond time scale. PES can also be applied with the pump-probe technique [3-5]. Thus, on the as/fs time-scale, it can be used to reveal the electron dynamics of molecular and solid-state samples. The time-resolved photoemission spectroscopy (TRPES) studies were realized with the use of ultrashort laser pulses, where the effect of multi-photon ionization was exploited for generation of the photoelectrons [4, 6].

However, it is advantageous to probe the transient electronic structure by one-photon ionization transition, via applying radiation of sufficiently high photon energy to overcome the binding energy of the electrons in the sample. In this case, one does not need to apply the high radiation intensities required to drive multiphoton ionization. Also, the interpretation of the transient ionization spectra is more straightforward as spectral contributions from intermediate resonances with higher-lying excited states can be eliminated from the spectra; particularly when lower probe intensities can be adopted, resulting in negligible multiphoton ionization and probe-induced ponderomotive electron energy shifts. Ionization of the sample in a single-photon process can be achieved by application of X-Ray or extreme ultraviolet (XUV or EUV) pulses of radiation. While ultrashort pulses in the broad spectral range from X-Ray to IR can be generated in synchrotron or free electron laser facilities, XUV pulses can be generated by a table-top high harmonic generation (HHG) setup. The latter enables investigation of the electron dynamics in valence band of many samples, including solids and solvated transition metal complexes. Such a TRPES experiment with the use of the XUV pulses as a probe beam, performed with a transition metal complex in aqueous solution, forms the basis of the present work.

Nowadays functional materials find application in many different fields of modern life. Some examples are: consumer electronics, sophisticated medical devises, and solar energy conversion. The knowledge of the electronic structure and the electronic dynamics is important for designing new materials with the needed properties and for “tuning” of their functional characteristics. Development of functional materials often involves transition metal complexes because of their fascinating photochemistry. Here, the knowledge of the electronic dynamics can play a crucial role. For example, Ir(III) complexes are implemented in the production of organic light-emitting diodes (OLED), where they are employed as photosensitizers [7-9]. Ir(III) complexes typically exhibit high intersystem-crossing quantum yield from the excited singlet to the intermediate triplet states, which is the key parameter for the efficient OLED operation. However, not

all the complexes are equally effective because of the different deactivation pathways of the excited state, which depends on the choice of ligands. Thus, the study of the electron dynamics facilitates to design the molecular complex with specific ligands for optimal OLED performance. As another example, the electron dynamics plays a crucial role for the development of dye-sensitized solar cells. Here, the charge from the photoexcited states of the dye molecule should undergo a transition to the conduction band of the semiconductor electrode in the most efficient way. Recent publications [10, 11] demonstrate the capabilities of the TRPES in revealing injection kinetics and electronic structure of dye-sensitized TiO_2 and ZnO interfaces, employing a Ru(II) dye complex as the sensitizer.

In the last decades, the interest in the development of novel materials, the properties of which can be controlled by external perturbations, has considerably increased. This interest is largely associated with the development of the information technology which progressively requires the size reduction of the hardware components. Bistable functional materials, based on the spin-crossover (SCO) phenomenon, are very promising candidates for various applications in this technological field. SCO materials can be potentially applied in molecular electronics, data storage, display and sensor devices [12-18]. The SCO itself is a reversible effect, which appears in a number of transition metal coordination complexes and consist in the switching between two electronic states, with the lower and higher numbers of unpaired electrons, in the valence d-orbitals of a transition metal atom. As a result, for transition metal complexes the switching leads to a change of the magnetic properties, the color, and the size of the coordination complex. Among different ways to initiate this effect, it can be induced at room temperature by a light pulse within an extremely short time period. These properties make SCO compounds very attractive for the future practical applications mentioned above.

Besides the many-fold potential functional material applications, the SCO phenomenon additionally poses relevance to biology [19-21] and geology [22, 23]. E.g., in biology, it is associated with important fundamental processes, such as oxygen transport by hemoglobin. In geology, SCO is utilized to explain processes in the lower mantle of the earth.

Both the future technological applications and the necessity to understand the fundamental processes in nature make the study of the electron dynamics in the SCO compounds an important task for the scientific community. Since its discovery by Cambi in 1930s [24, 25], the SCO phenomenon was under extensive investigations. In this work,

TRPES was successfully applied to reveal the mechanism of the ultrafast SCO in iron(II) tris-bipyridine ($[Fe(bpy)_3]^{2+}$) in aqueous solution for the first time. Despite previous efforts over the last 40 years in studying this complex, the exact steps of the SCO process following photoexcitation by light were still disputed in the literature. The present work demonstrates the direct observation of the evolution of the electronic structure of photoexcited $[Fe(bpy)_3]^{2+}$(aq) on the femtosecond time scale, and it gives the final interpretation of the SCO mechanism, supported by theoretical calculations.

In general, this work incorporates two important objectives:

1. Development and application of the novel methodology for the TRPES studies, employing the table-top HHG setup as a source of the XUV probe beam in a pump-probe configuration, which can be applied to investigate photochemical processes in various transition metal complexes in solution.
2. Revealing, the previously disputed in the literature, mechanism of photoinduced SCO in $[Fe(bpy)_3]^{2+}$(aq) following excitation to the singlet metal-to-ligand charge transfer state (^{1}MLCT).

This thesis includes the following six chapters. Chapter 2 describes the scientific background, including the most relevant considerations of ligand field theory and the SCO phenomenon, and gives an overview of the previous studies by other research groups on the SCO mechanism in $[Fe(bpy)_3]^{2+}$. Chapter 3 introduces the methodological background relevant to the experimental procedure. Chapter 4 introduces the experimental setup. Chapter 5 incorporates the presentation and discussion of the experimental results. Chapter 6 describes briefly the preliminary results of the study of the photodissociation dynamics in $Fe(CO)_5$, which was performed by employing the developed TRPES approach. Finally, Chapter 7 gives a summary of the findings obtained in this work.

2 Scientific background

This chapter presents an overview of the properties of the iron(II) tris(bipyridine) ($[Fe(bpy)_3]^{2+}$) complex and gives the scientific background of the present work. The first section of the chapter will introduce the most important terms and concepts of the ligand-field theory, which provides an insight into the origin of the formation of energy levels and photochemistry of transition metal complexes. The second section will briefly introduce the spin crossover phenomenon, which was the focus of this study. And finally, the third section of this chapter will present the particular properties of $[Fe(bpy)_3]^{2+}$, including its electronic structure, and its photophysical and photochemical properties. Additionally, the over-40-year history of time-resolved experiments applied on the $[Fe(bpy)_3]^{2+}$ complex in order to reveal these properties, will be presented. At the end of the chapter, two actual and principally contradictory interpretations of the spin crossover (SCO) mechanism will be given and the main scientific question of the present study will be raised.

2.1 Transition metal complexes

2.1.1 Ligand-field theory

Transition metal complexes are a class of chemical compounds, which play an important role in modern chemistry. They consist of a transition metal center surrounded by a certain number of organic ligands, which can be ions or neutral molecules. Characteristically, transition metals have incompletely filled d-subshells in both ionic and neutral form. The nature of the bonding between the metal core and ligands is explained by the ligand-field theory, which builds on the more simplified crystal-field theory [26].

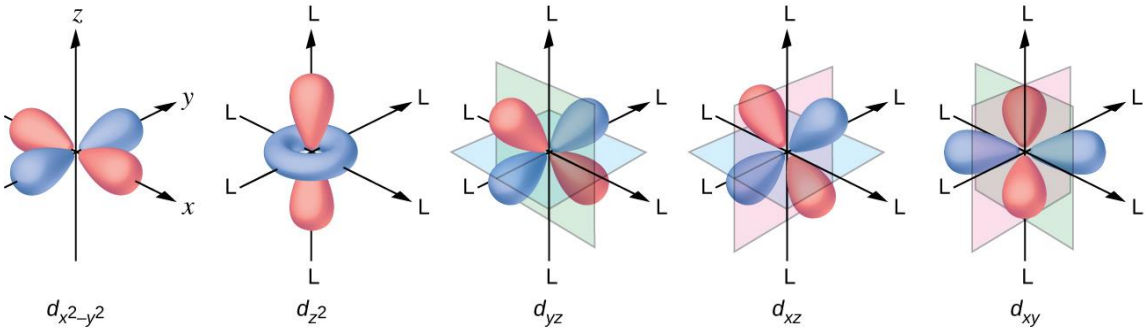

Figure 1. The shape and the orientation of d-orbitals with respect to the ligands (L) in an octahedral geometry. Figure is taken from Ref. [27].

In this work, transition metal complexes with octahedral symmetry are of particular interest. According to crystal-field theory, the original unperturbed energy level of a free atom undergoes a shift in an octahedral, spherically symmetric environment of 6 negative point charges. It defines the barycenter of the perturbed energy levels. In the perfect octahedral ligand field, the orientation of the d-orbitals with respect to the ligands (see Figure 1) leads to the splitting of the energy levels in two fractions. The d_{xy}, d_{yz} and d_{xz} orbitals - which are placed in-between the ligand axis - build the t_{2g} band lying energetically lower than the barycenter. The $d_{x^2-y^2}$ and d_{z^2} orbitals - which are placed closer to the ligands along their axis - build the e_g band lying higher than the barycenter. The splitting ratio between the t_{2g} an e_g orbitals in octahedral complexes is 2:3, respectively. The energy gap between the t_{2g} and e_g orbitals is given in the literature as ligand-field splitting parameters Δ_o [28] (in the literature also denoted as 10Dq). This is summarized

in the Figure 2. The value of Δ_o is specific for every complex and depends on the identity of the metal ion, strength of the ligands and the character of the metal-ligand bonding.

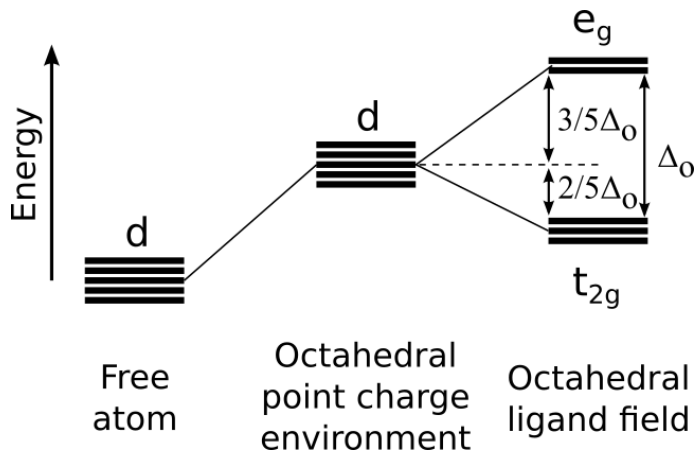

Figure 2. Splitting of the 3d orbitals of the central metal ion in an octahedral ligand field.

According to Hund's rules, the orbitals in the same subshell should be first filled with the electrons possessing parallel spins, so that the total spin angular momentum and the multiplicity acquire maximal values. After no free orbitals are left to accommodate a single electron, two electrons are paired with opposite spins in the same orbital. This way, the electronic configuration acquires the lowest energy and, therefore, is energetically more favorable. However, for d^4, d^5, d^6 and d^7 complexes, two different configurations are possible. If the Δ_o is lower than the energy needed for the pairing of electrons E_p, the configuration with the highest number of electrons with parallel spin will be energetically more favorable. Such a case ($\Delta_o<E_p$) is called a weak-field case and leads to the formation of the high-spin (HS) complex with HS electronic configuration. The opposite case, when the ligand-field splitting parameter is higher than the pairing energy and it requires less energy to fill one or more t_{2g} orbitals with paired electrons than to override the gap to e_g orbitals, is called a strong-field case. These latter compounds are called low-spin (LS) complexes with LS electronic configuration.

2.1.2 Electron transitions and excided states

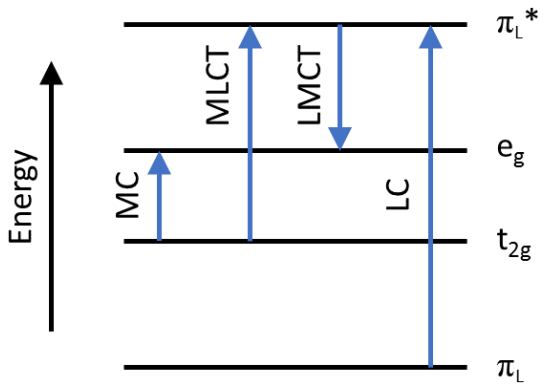

Figure 3. Electron transitions in a d^6 transition metal complex with O_h symmetry represented by blue arrows. π_L und π_L* denote the π orbitals of the ligands and e_g and t_{2g} denote orbitals originating from the splitting of the metal 3d orbitals in an octahedral ligand field. Notations are: MC – metal centered transition, MLCT – metal-to-ligand charge-transfer transition, LMCT – ligand-to-metal charge-transfer transition, LC – ligand centered transition.

One of the most important photochemical properties of transition metal complexes are electron transitions from one molecular orbital to another, which can be initiated by light irradiation. Intensities of the transitions depend on the spin and symmetry selection rules [29]. According to the selection rules, the spin is conserved under phototransition whereas the symmetry changes between "gerade" and "ungerade" by absorption of one photon. The electron transitions are responsible for the manifold of absorption bands in the absorption spectra of this class of chemical compounds. The classification is established according to the involved molecular orbitals. Thus, one can distinguish the following types of electron transitions [30]:

1. *Metal centered (MC) or Ligand Field (LF) transitions*. Transitions of this type take place between two orbitals mainly localized on the central metal atom. For example, the MC transition involves t_{2g} and e_g predominantly metal orbitals for the complexes in octahedral symmetry, as shown in the Figure 3. This transition leads to the formation of the LF excited states. Depending on the spin orientation and distribution of the electrons in the degenerate set of orbitals, the LF states can have different multiplicities, where the electron configuration gives rise to the formation of more than one state with given multiplicity. For octahedral complexes, transitions within d-orbitals are usually symmetry-forbidden, since the parity of both t_{2g} and e_g states is "gerade". Given this fact, LF states in octahedral complexes cannot be populated directly by absorption of a single

photon. However, these states still can be populated via decay from the higher photo-excited states by involving non-radiative relaxation mechanisms, such as intersystem crossing (ISC) or internal conversion (IC). ISC represents the transition within states with different spin multiplicity, while IC involves the states with the same multiplicity. Since in the latter process spin change doesn't take place, in many cases IC is notably faster than ISC.

2. *Charge-transfer transitions*. In these transitions, excitation of an electron occurs between two molecular orbitals, which mainly "belong" to two different atoms or groups of atoms, for example to the metal and to the ligands. The transition from predominantly metal orbital to predominantly ligand orbital (with σ or π character) is denoted as metal-to-ligand charge transfer (MLCT). Accordingly, the opposite variant of transition is denoted as ligand-to-metal charge transfer (LMCT). Removing (or adding) of an electron from (or to) predominantly metal orbitals leads to the change of its local oxidation state. MLCT transitions are especially typical for complexes with central atoms having low ionization potential and ligands with easy available empty π* orbitals, like in e.g. $[Fe(bpy)_3]^{2+}$, which lies in the focus of this work. Both MLCT and LMCT transitions are illustrated in the Figure 3. Besides these two charge-transfer transitions, one should also mention ion-pair charge transfer (IPCT), ligand-to-ligand charge-transfer (LLCT) and charge-transfer-to-solvent (CTTS) transitions. However, the latter three types of the charge-transfer transitions are not significant for this work. The description of these transitions can be found e.g. in the Ref. [30].

3. *Ligand centered (LC) or intraligand transitions*. LC transitions can be defined as transitions between two molecular orbitals predominantly localized on the ligand system. They commonly occur in transition metal complexes with ligands exhibiting extended π-systems. This is typical in the case of the aromatic ligands, such as e.g. pyridine, bipyridine and phenanthroline. The position of the corresponding bands in the spectra is rather independent from the central metal atom. The example of a typical $\pi \rightarrow \pi^*$ LC transition in an octahedral transition metal complex is illustrated in Figure 3 as well.

According to the Franck-Condon principle, photoexcitation at a specific wave-length often leads to the formation of vibrationally excited electronic states. Since the electronic transitions are much faster than nuclear motion, the excited state appears first with the ground state nuclear configuration. The initial photoexcitation is commonly followed by vibrational relaxation or IC to other thermally accessible electronic states

[29]. Besides, the spin-forbidden ISC can take place when spin-orbit coupling (SOC) is considered. The probability of ISC in this case can by described by equation:

$$W \sim \frac{\langle \Psi_i | \boldsymbol{P}_{SOC} | \Psi_j \rangle^2}{(E_i - E_j)^2}, \quad (1)$$

where $\langle \Psi_i | P_{SOC} | \Psi_j \rangle$ is the SOC matrix element between electronic states i and j, and E_i and E_j are there energies. Thus, for the higher probability of ISC, either the SOC should be strong, or the states should come closer to each other on the energy scale. The latter is the case for light elements, such as e.g. iron, where the SOC itself is relatively weak.

In general, fluorescence, phosphorescence and nonradiative decay can follow the photoexcitation. The decay from the electronically excited states can involve more than one step of these different types of de-excitation. The relaxation process can occur on a broad range of time scales, covering many orders of magnitude from femtoseconds to microseconds. Thus, the relaxation pathways of different transition metal complexes can take a manifold of different routes. Characterization of these pathways is crucial for understanding of photochemical and photophysical properties of transition metal complexes. Time-resolved spectroscopy methods enable us to solve this complicated task.

2.2 Spin crossover

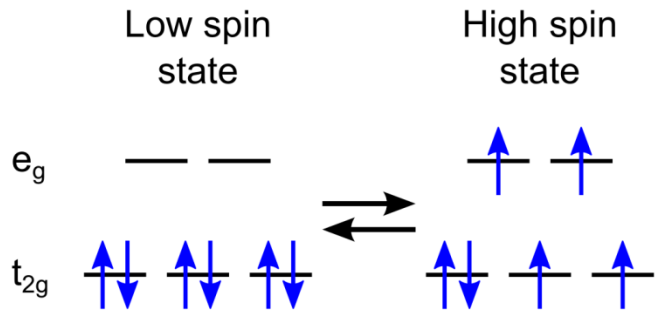

Figure 4. Schematic representation of the spin crossover in an octahedral d^6-metal complex according to the distribution of electrons in the 3d orbitals of the central metal ion.

Spin crossover (SCO) can be defined as a phenomenon of changing of spin multiplicity of the transition metal complexes due to switching between LS and HS electron configuration. The process can be initiated by temperature, light or pressure in

solid state or in liquid solution. SCO is accompanied with the changing of the metal-ligand bond length, magnetic properties and absorption spectrum of the transition metal complex. The latter leads to the change of color in some compounds. The phenomenon occurs in complexes with electron configurations d^4 to d^7 of the 3d metal center and in d^8 metal complexes with lower than octahedral molecular symmetry [31]. Figure 4 illustrates an example of changes in the electronic structure due to the SCO process in a d^6-metal complex with octahedral molecular symmetry. Besides the properties of the ligands, the ligand field strength is strongly related to the metal-ligand distance, what can be expressed by the following equation [31]:

$$\frac{\Delta_0^{\mathrm{LS}}}{\Delta_0^{\mathrm{HS}}} = \left(\frac{r_{\mathrm{HS}}}{r_{\mathrm{LS}}}\right)^6, \qquad (2)$$

where Δ_0^{LS} and Δ_0^{HS} represent the ligand field splitting in LS and HS states, respectively, and r_{LS} and r_{HS} denote the metal-ligand distances in LS and HS states, respectively. This fact makes the metal-ligand bond elongation an important physical characteristic of the SCO process.

The SCO phenomenon was discovered for the first time in the 1930s by Cambi et al. [24, 25], who observed unusual magnetic behavior for the iron(III) tris(dithiocarbamate) complexes. Later, the process was described with the use of ligand field theory, which gave rise to a growing interest in new bi-stable coordination compounds exhibiting thermally induced transformation of the electronic structure. Particularly, the family of Fe(II) SCO complexes attracted much attention in the 60s-70s, since ^{57}Fe Mössbauer spectroscopy (which became available in that period) was very well suited for characterization of electronic and molecular structure of Fe(II) compounds. Observation of the characteristic resonance signal in the Mössbauer spectra clearly showed the temperature-depended change between LS and HS structure [32-38]. Detailed discussion of the thermally induced spin transitions can be found e.g. in the Ref. [31].

The first light-induced SCO was discovered in 1984 by Decurtins et al. [39] in $[Fe(ptz)_6](BF_4)_2$ by means of optical spectroscopy. In this experiment, the optically excited (at the wavelength of 514.5 nm) HS state could be "frozen" and investigated at low temperature. The effect was termed as light-induced, excited spin state trapping (LIESST) and was extensively studied in Refs. [40-54]. Decurtins et al. [40] predicted a two-step ISC mechanism, involving an initially excited singlet LF state and a triplet LF state as an intermediate step on the way to the quintet HS state. Moreover, a reverse

transition was observed in the trapped HS state initially populated by photoexcitation with green light. The reverse transition was induced by irradiation of the sample with infrared light at the wavelength of 820 nm [42].

During the last 40 years, the development of ultrafast spectroscopy techniques with continuously improving time resolution made the extensive characterization of the SCO mechanism in the solid state and in solution feasible without application of LIESST. Promising perspectives of the practical application of SCO heighten the profile of this fascinating phenomenon. Since the first report of Cambi et al., several hundreds of SCO complexes were synthesized and characterized [16]. One of these complexes, iron(II) tris(bipyridine) ($[Fe(bpy)_3]^{2+}$), where the SCO process can be induced by light irradiation, is the focus of the present study.

2.3 Iron(II) tris(bipyridine)

2.3.1 Electronic structure and properties of $[Fe(bpy)_3]^{2+}$

$[Fe(bpy)_3]^{2+}$ belongs to a large family of polypyridine complexes. It occurs in a form of deep red crystals that are soluble in water. The deep red color of the solution makes the complex suitable for colorimetric analysis [55]. On account of its photochemical properties, $[Fe(bpy)_3]^{2+}$ can be used as a photosensitizer. For example, this complex can be used to improve the photocatalytic properties of graphitic carbon nitride for the light assisted oxidative coupling of benzylamines [56].

$[Fe(bpy)_3]^{2+}$ can be synthesized in a chemical lab from $FeCl_2$ and bipyridine with different counterions. In the sample used in this work, the counterion was chlorine and the complete molecular formula was $C_{30}H_{24}Cl_2FeN_6$.

Figure 5(a) demonstrates the 3D model representing the geometrical structure of the $[Fe(bpy)_3]^{2+}$. The iron atom is placed in the center of the molecule and is surrounded by three bidental bipyridine ligands. This results in a predominantly O_h symmetry with a trigonal (D_3) distortion [57, 58]. In the ground state, the molecule exhibits a LS structure, where all 6 outermost electrons are distributed in pairs in the t_{2g} orbitals. Lowering of the molecular symmetry by the trigonal distortion of the ligand field leads to lifting the degeneracy of the electronic structure of the iron(II) atom. Consequently, the t_{2g} orbitals split slightly in two e_g orbitals and one a_{1g} orbital, as shown in the Figure 6. Since the energy difference between them is rather small (~0.1 eV), these orbitals will

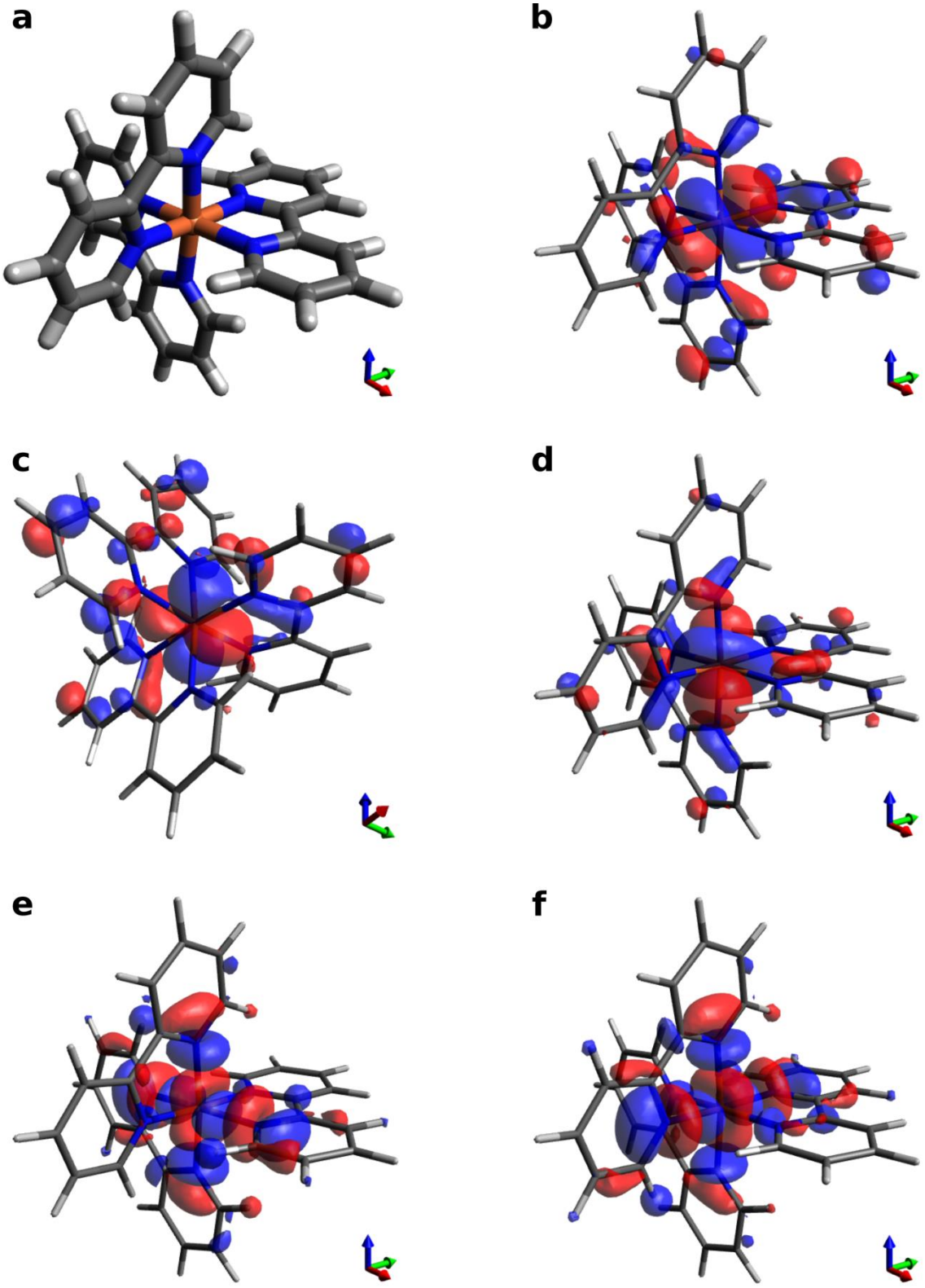

Figure 5. (a) 3D model representing the geometrical structure of the $[Fe(bpy)_3]^{2+}$ molecule. Red color denotes the iron atom. Blue, grey and light grey colors denote nitrogen, carbon and hydrogen atoms of the bipyridine ligands, respectively. (b, c, d) Calculated electron density distributions of t_{2g} orbitals of the $[Fe(bpy)_3]^{2+}$ molecule in the LS ground state. (e, f) Calculated electron density distributions of e_g orbitals of the $[Fe(bpy)_3]^{2+}$ molecule in the LS ground state. All illustrations were carried out with the use of Avogadro molecule editor [59].

be termed as t_{2g} further in text. Figure 5(b-f) demonstrate the shape of the electron density distribution of the t_{2g} and e_g orbitals according to the DFT ground-state calculations. The calculations were carried out by Dr. Kaan Atak (Helmholtz-Zentrum Berlin) with the use ORCA software package [60]. Doubly occupied t_{2g} orbitals (see Figure 5 (b, c, d)) are non-bonding and exhibit mainly metal character, while empty e_g orbitals (see Figure 5 (e, f)) are antibonding and exhibit σ-character, which results from the metal-ligand interactions.

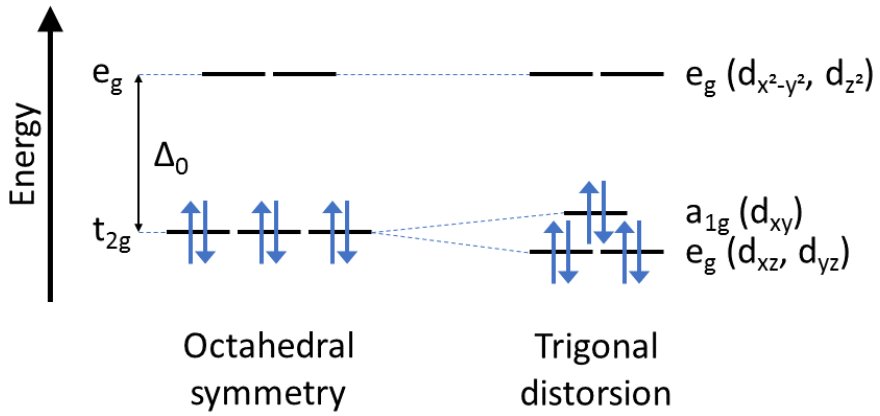

Figure 6. Splitting of the 3d orbitals of the iron(II) atom in an iron tris(bipyridine) molecule upon symmetry lowering due to the trigonal (D_3) distortion.

2.3.2 Absorption spectra of $[Fe(bpy)_3]^{2+}$

The steady-state UV-Vis absorption spectrum of the $[Fe(bpy)_3]^{2+}$ shown in Figure 7 reveals a manifold of absorption bands between 200 nm and 600 nm. One can point out three main regions in the spectrum and assign them to the different charge-transfer transitions, according to the Refs. [61-63]. Two bands between 320 and 420 nm and between 420 and 600 nm arise due to the MLCT transition from the 3d(t_{2g}) orbitals of iron to the lowest unoccupied π^* molecular orbitals of bipyridine, where we distinguish between the asymmetric and symmetric π^* orbitals, respectively. Symmetric and asymmetric orbitals can be classified with respect to a twofold rotation axis, bisecting the chelate angle [64]. The MLCT absorption band in the visible region of the spectrum is responsible for the deep red color of the complex. A trident structure in the UV region of the spectrum between 200 and 320 nm is assigned to LC transitions from π to π^* orbitals of the bipyridine ligands.

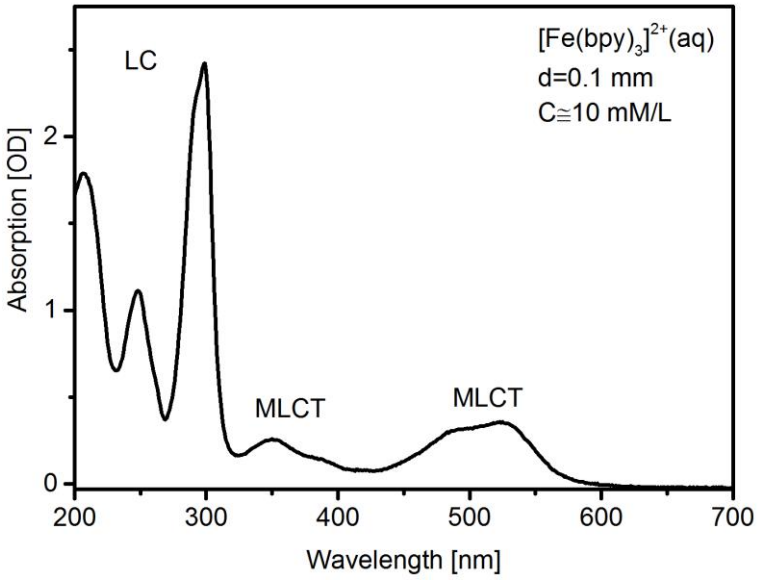

Figure 7. Absorption spectrum of the ~10 mM aqueous solution of $[Fe(bpy)_3]^{2+}$ recorded with the use of commercial spectrophotometer JENWAY 7315.

2.3.3 Previous studies on spin crossover dynamics

The manifold of potential applications and the fascinating photochemical and photophysical properties, which were described above, made $[Fe(bpy)_3]^{2+}$ an attractive object in numerous studies. The history of time-resolved investigation of the complex begins in the middle of 70s. An early picosecond absorption spectroscopy study by Kirk et al. [65], applied on a number of different transition metal complexes in solution, revealed ground-state bleaching of $[Fe(bpy)_3]^{2+}$ caused by photoexcitation at a wavelength of 530 nm. The recovery time of the ground state was measured to be 0.83 ± 0.07 ns. That time the excited states could not be assigned unambiguously to particular charge-transfer transitions. By the end of the 70s, Creutz at al. [66] examined transient absorption spectra of $[Fe(bpy)_3]^{2+}$ in the 300–500 nm wavelength range with the use of picosecond absorption spectroscopy and came to the conclusion that the excited states exhibit ligand-field character and they can be either triplet or quintet ligand-field states. In the following studies the same research group attempted to describe the excited-state decay mechanism in Fe(II) complexes, nowdays known as a part of the SCO process [67-69]. The latter experiments were based on transient absorption spectroscopy with nanosecond and sub-nanosecond resolution. Later, Bergkamp et al. [67] confirmed the ligand-field nature of the excited state formed due to the depopulation of the initially

photoinduced MLCT states within <10 ps, and Hauser et al [68] suggested triplet LF states as a possible intermediate step in the decay from MLCT to the quintet LF state. Finally, in 1993 McCusker et al. [69] proposed the mechanism of the interconversion between the ground state ($^1A_1$) and the quintet LF state ($^5T_2$). This mechanism involved initial excitation of the ^{1}MLCT state, direct population of the $^5T_2$ excited state from the ^{1}MLCT state within ~700 fs, and vibrational cooling in the $^5T_2$ excited state within 2-3 ps.

These early experiments prepared the base for the understanding of the SCO mechanism in $[Fe(bpy)_3]^{2+}$. However, the poor time resolution was a crucial limitation for tracking the process, which as we know today occurs on the femtosecond time-scale. Application of different modern time-resolved methods and experimental strategies, triggered by the appearance of femtosecond laser systems, in the last ten years precipitated the detailed characterization of the photocycle of the SCO process in $[Fe(bpy)_3]^{2+}$. However, fundamental question, which will be outlined below, remained open.

The following experimental methods were applied during the last 10 years to study the SCO process in $[Fe(bpy)_3]^{2+}$:

- Femtosecond fluorescence up-conversion spectroscopy [70]
- Transient UV and visible absorption spectroscopy in solution [70-72] and in single crystals [73]
- Picosecond hard X-Ray absorption spectroscopy [74]
- Femtosecond X-Ray absorption near edge structure (XANES) studies [75, 76]
- Femtosecond X-Ray powder diffraction [77]
- Combination of X-Ray emission spectroscopy with X-Ray diffuse scattering [78]
- Ultrafast transient soft X-Ray absorption spectroscopy [79]
- Ultrafast X-Ray fluorescence spectroscopy [80]

Besides the experimental studies listed above, one should also mention a number of theoretical works dedicated to the reviewed topic that were performed in this time period [58, 63, 81-85].

Femtosecond fluorescence spectroscopy performed by Gawelda and co-workers [70] with a temporal resolution of ~100 fs revealed two spectral emission peaks, which were assigned to the singlet and triplet MLCT states. The data analyses yielded lifetimes of <30 fs and ~130 fs for ^{1}MLCT and ^{3}MLCT, respectively. Transient absorption studies

performed in the visible range with a time resolution of ~140 fs [70] exhibited the ground state bleach (GSB) signal, originating from the depletion of the LS ground state under photoexcitation by the 400 nm pump laser pulse. Global analyses of the data obtained in this experiment delivered three time constants: 115 ± 10 fs, 960 ± 100 fs and 665 ± 35 ps. The first time constant was assigned to the life time of the ^{3}MLCT state and the third one to the recovery of the ground LS state. The second time constant could not be associated by the authors with any of given states of $[Fe(bpy)_3]^{2+}$. Later, Consani and co-workers [71] revealed vibrational dynamics in the excited HS state by means of UV transient absorption spectroscopy. This study, performed with a time resolution of ~130 fs, uncovered the bimodal dynamics with 1.1 ± 0.17 ps and 3.4 ± 1.2 ps time constants in the process of vibrational cooling of the HS state.

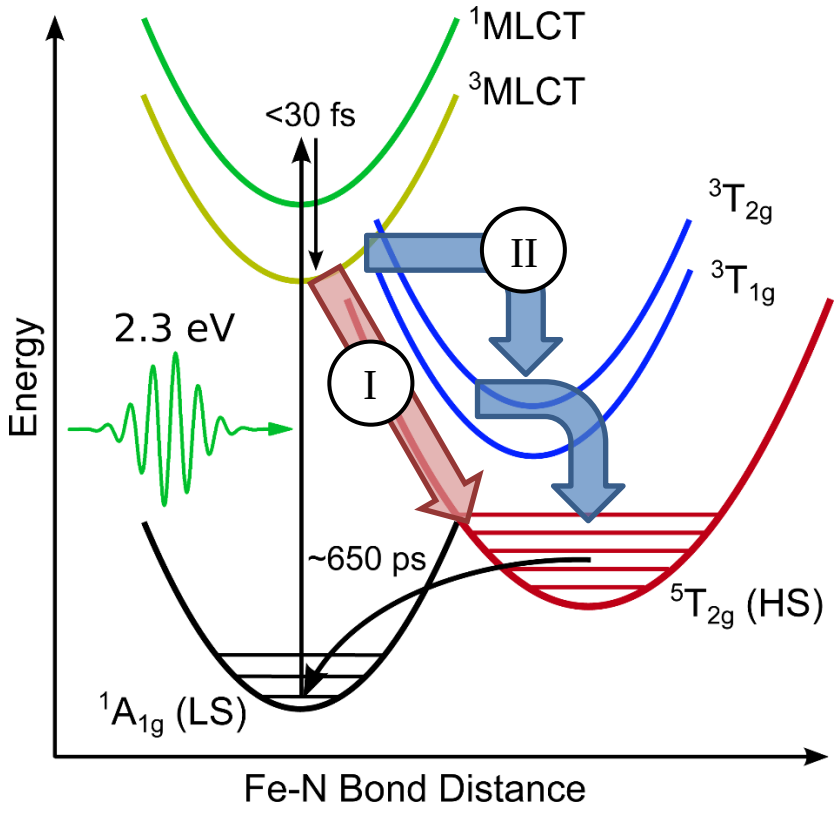

Figure 8. Photocycle of the SCO in $[Fe(bpy)_3]^{2+}$: following the photoexcitation at the wavelength of 530 nm (photon energy of 2.3 eV) the electron populates first the ^{1}MLCT state and then is transferred via the intersystem crossing to the ^{3}MLCT within <30 fs. The following relaxation to the metastable quintet HS state can occur either stepwise via the intermediate triplet LF states (II) or directly (I). The direct transition is mediated by non-totally-symmetric vibrational modes. Finally, the system relaxes from the HS state to the ground LS state within ~650 ps. Vibrational cooling within the HS state is not shown in the figure.

In contrast to the visible absorption experiment, spectra recorded in this study exhibited excited state absorption (ESA) signal associated with the formation and decay of the MLCT and quintet LF states besides the GSB signal. The interesting result of this study was the fact, that the MLCT ESA decays on the same time scale of 130 fs as the rise time of the HS state ESA. Additionally, this experiment delivered the time constant of 650 - 700 ps for the recovery of the ground state, which was consistent with Ref. [70].

Apart from the studies mentioned above, XANES experiments with few-picosecond and femtosecond time resolution were applied in order to reveal the SCO mechanism in aqueous solution of $[Fe(bpy)_3]^{2+}$. Distinct from UV and visible transient absorption spectroscopy, time-resolved X-Ray absorption spectroscopy (XAS) employs the absorption properties of the atomic core electrons and allows us to monitor the structural changes induced in the molecule by the excitation due to optical laser pulse. The probe pulses in these experiments were produced with the use of the synchrotron facility [74, 75] and by application of the free electron laser [76]. The results highlighted the elongation of the Fe-N bonding by ~0.2 Å in the excited HS state, which is also typical for other Fe(II)-based SCO complexes [86-97] despite the different life-times of the HS state. Time-resolved XANES also revealed the decay time of the ^{3}MLCT and the rise time of the HS state on the scale of ~150 fs, and the time constant of 650 ps for the HS state decay.

Figure 8 schematically represents the photocycle, which summarizes the results of the studies described above. The first event after the photoexcitation from the ground LS state to the ^{1}MLCT state is the ultrafast intersystem crossing from the ^{1}MLCT to the ^{3}MLCT within <30 fs. In the second step, the population of the ^{3}MLCT undergoes the transition to the vibrationally excited HS state either directly (Figure 8, I) or via the population of intermediate triplet LF states ($^3T_{1,2}$) (Figure 8, II) within <130 fs, accompanied by the elongation of the Fe-N bond length by ~0.2 Å. The HS state vibrationally relaxes in a bimodal way, where the modes suggested to be assigned to relaxation of the Fe-N elongation and to the bending and chelate angles [98]. Finally, the population returns to the ground LS state on the time-scale of 650 ps.

2.3.4 Two different interpretations

The studies described above could partly characterize the photocycle of the SCO process in $[Fe(bpy)_3]^{2+}$. Nevertheless, the question whether the triplet LF states are

involved in the deactivation mechanism following the population of the MLCT states remains open. The two latest experimental studies dedicated to this subject presented two contradictory interpretations. Zhang and co-workers are convinced of the presence of signatures of the triplet intermediate LF states in their transient X-ray fluorescence spectra and propose the *sequential (or cascaded) model* of the excited state population decay as follows: ^{1,3}MLCT→^{3}T→^{5}T. The experiment employed Kβ X-ray fluorescence spectroscopy, which is highly sensitive to the iron spin multiplicity, with the use of free electron laser for the probe pulse generation and delivered time constants of 150 ± 50 fs and 70 ± 30 fs for the decay of MLCT and of the triplet LF states, respectively. The time resolution of these measurements was ~150 fs. On the other hand, Auböck and Chergui [72] proposed the *direct model*, where the population undergoes the transition from ^{3}MLCT to quintet HS state mediated by non-totally-symmetric vibrational modes. Thus, the whole ^{1}MLCT→^{3}MLCT→^{5}T conversion is complete in <50 fs. The authors applied transient absorption spectroscopy with the time resolution of <60 fs in the UV and of <40 fs in the visible probe range in this study. Essentially, this experiment repeats previously published and above mentioned transient absorption studies of Gawelda et al. [70] and Consani et al. [71] with the superior time resolution. In Figure 8, the direct and the sequential de-excitation pathways are denoted with I and II, respectively.

The direct model has been suggested earlier by Chergui and co-workers in Refs. [75, 98] and even earlier by McCusker et al. [69], however, the latter proposed the direct decay to ^{5}T from ^{1}MLCT without involving the ^{3}MLCT. The main arguments for rejecting the triplet LF states were the above mentioned population of the HS state and decay of the MLCT state on the same time scale and the 100% quantum yield for the MLCT→^{5}T conversion. According to Chergui et al., the latter would not be possible with the ^{3}T intermediate state, since a leak back to the ground LS state should occur in this case. In the recently published article [72], the authors argue that the whole process is completed so fast that if the other LF states would be involved, they would have lifetimes of <20 fs.

However, Gaffney and co-workers, who support the concept of the sequential model, presume that stepwise relaxation should occur faster than the direct one. This is because the sequential model involves single electronic transitions coupled by a spin-orbit operator, unlike the direct model that involves a simultaneous spin change of two electrons and cannot occur when considering the first-order spin-orbit operator [79]. Moreover, the same rise time of the HS state as the decay time of the MLCT states, despite including the triplet LF states in the model, can be possible if the population of the latter

decays faster than their population grows. The cascaded model is also supported by theoretical calculations performed by Sousa et al. [82], which predict the sequential relaxation pathway involving triplet LF states as most probable.

In the end of this chapter, one should mention that the different methods, which were previously applied to study the SCO, are sensitive to different specific properties of the sample and could not give the complete picture of the process. The novel method, which will be presented in the next chapters of this work, provides a completely new insight into the SCO phenomenon.

3 Experimental methods

The present work combines different experimental methods and techniques. The following chapter gives an overview of these methods and techniques as well as describes the peculiarities of their application in practice. It starts with the basic aspects of nonlinear optics, since such knowledge is necessary for accomplishing the first task of preparation of a TRPES experiment: the generation of the pump and probe laser pulses and delivering them to the interaction region of the setup. This part of the chapter includes a general description of the method of parametric amplification of ultrashort laser pulses, and it also presents the method of generation of XUV light via high-order harmonics of laser radiation. Additionally, the effects accompanying the propagation of ultrashort light pulses in a dispersive medium will be discussed. Application of this knowledge allowed us to achieve the time resolution of a few tens of femtosecond in the conducted experiment.

Another section of this chapter is dedicated to the main aspects of photoelectron spectroscopy. This includes the scientific background and the different techniques of photoelectron detection. The time-of-flight technique applied in this work is described in detail along with relevant physical processes which can influence the results of the TRPES measurements. The PES requires vacuum conditions, which represents a challenging technical task. In the last section of this chapter, the solution for this problem is presented, based on the application of a liquid microjet technique. The peculiarities of applications of this technique will be described as well.

3.1 Generation of ultrashort laser pulses

3.1.1 Basic aspects of nonlinear optics

During the propagation of intense laser light through optical media, diverse nonlinear optical processes can take place. These processes can be utilized for the creation of light sources needed for spectroscopy experiments. They originate from the nonlinear dependency of the polarization density of light as a function of the electric field strength. The light-induced polarization **P** can be represented by a Taylor series expended in terms of the electric field **E**:

$$\begin{aligned} \mathbf{P} &= \chi_1 : \mathbf{E} + \chi_2 : \mathbf{EE} + \chi_3 : \mathbf{EEE} + \cdots = \\ &= \mathbf{P}_{\text{lin}} + \mathbf{P}_2 + \mathbf{P}_3 + \cdots = \mathbf{P}_{\text{lin}} + \mathbf{P}_{\text{NL}} \end{aligned} \tag{3}$$

For a weak field strength **E**, the nonlinear components of the polarization $\mathbf{P}_{\text{NL}}$ can be neglected, which is the case of trivial linear optics. In the case of high intensities of the propagating light, which is characteristic of ultrashort laser pulses form modern laser systems, the role of the nonlinear component increases dramatically. Electromagnetic waves can interact with each other in a non-linear medium. As a simple case, we consider two waves with the electric field vectors $\mathbf{E}_1$ and $\mathbf{E}_2$ and with the frequencies ω_1 and ω_2, respectively. They can be represented as:

$$\begin{aligned} \mathbf{E}_1 &= \frac{1}{2}\mathbf{e}_1 \{A_1 \exp[i(2\omega_1 t - 2\mathbf{k}_1\mathbf{r})] + c.c.\} \\ \mathbf{E}_2 &= \frac{1}{2}\mathbf{e}_2 \{A_2 \exp[i(2\omega_2 t - 2\mathbf{k}_2\mathbf{r})] + c.c.\}, \end{aligned} \tag{4}$$

where $\mathbf{e}_1$ and $\mathbf{e}_2$ are the unit vectors, and $\mathbf{k}_1$ and $\mathbf{k}_2$ are the corresponding wave vectors. Considering the second order component $\mathbf{P}_2$ of the polarization induced in the presence of the superposed electric fields $\mathbf{E} = \mathbf{E}_1 + \mathbf{E}_2$, it can be represented as:

$$\begin{aligned} \mathbf{P}_2 = \frac{1}{4}\chi_2 : \{ & \mathbf{e}_1\mathbf{e}_1 A_1^2 \exp[i(2\omega_1 t - 2\mathbf{k}_1\mathbf{r})] + \\ & + \mathbf{e}_2\mathbf{e}_2 A_2^2 \exp[i(2\omega_2 t - 2\mathbf{k}_2\mathbf{r})] + c.c.\} + \\ + \frac{1}{2}\chi_2 : \mathbf{e}_1\mathbf{e}_2 \{ & A_1 A_2 \exp[i(\omega_1 + \omega_2)t - i(\mathbf{k}_1 + \mathbf{k}_2)\mathbf{r}] + \\ & + A_1 A_2^* \exp[i(\omega_1 - \omega_2)t - i(\mathbf{k}_1 - \mathbf{k}_2)\mathbf{r}] + c.c.\} + \end{aligned} \tag{5}$$

$$+\frac{1}{2}\chi_2 : (\mathbf{e}_1\mathbf{e}_1 A_1 A_1^* + \mathbf{e}_2\mathbf{e}_2 A_2 A_2^*)$$

Thus, it leads to the formation of the new frequencies $2\omega_1$, $2\omega_2$, $\omega_1+\omega_2$ and $\omega_1-\omega_2$. The formation of photons with the frequency $\omega_1 + \omega_2$ and $\omega_1 - \omega_2$ is called sum frequency generation (SFG) and difference frequency generation (DFG), respectively. The frequencies $2\omega_1$ and $2\omega_2$ represent the second harmonics of the incident frequencies ω_1 and ω_2. This process is called second harmonic generation (SHG), which is a special case of the SFG. The processes obey the energy conservation in terms of photon energies. For example, the SFG process can be described by the following equation:

$$\hbar\omega_3 = \hbar\omega_1 + \hbar\omega_2 \qquad (6)$$

The second order nonlinear processes are schematically presented in the Figure 9.

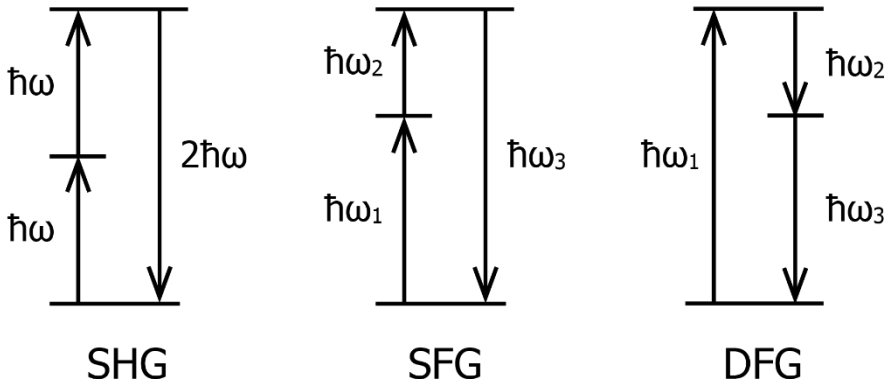

Figure 9. Schematic representation of the 2nd order nonlinear processes: second harmonic, sum frequency and difference frequency generation.

The highest efficiency for the SFG process can be achieved in the case if $\mathbf{k}_3 = \mathbf{k}_1 + \mathbf{k}_2$, where $\mathbf{k}_3$ is the wave vector of the generated wave. This equation represents the phase matching condition. In practice, it can be achieved in birefringent crystals. Electromagnetic waves of different polarization propagate in such crystals with different velocities due to the difference in the refractive index which depends on the angle between the optical axis of the crystal and the polarization of the traveling wave. Thus, the birefringence and the symmetry of the media can be used to fulfill the phase-matching condition, via adjusting the angle of the optical axis of the crystal with respect to the propagation direction of the lineally polarized laser beam. In practice, the nonlinear crystals are typically cut relative to its optical axis so that the input surface of the crystal

is nearly perpendicular to the incoming beams. This way the geometry of the interaction of the crystal with the laser light is optimized for a specific nonlinear process. Also, time and spatial overlap between the laser pulses should be ensured, which can be achieved by adjusting the optomechanical components of the setup.

3.1.2 Parametric amplification process

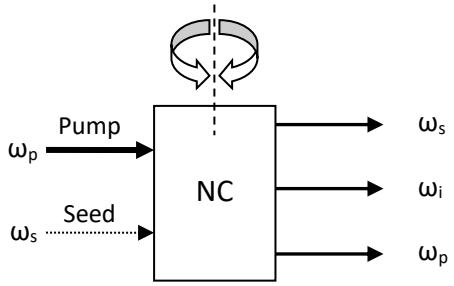

Figure 10. Schematic presentation of collinear parametric amplification process in a nonlinear crystal (NC). Signal and idler pulses are generated by splitting of the pump pulse photons with the frequency ω_p in two photons with frequencies ω_s and ω_i in the presence of the seed pulse with the frequency ω_s. By adjusting the angle between the optical axis of the NC and polarization direction of incoming pump and seed beams, the phase-matching condition can be achieved for the parametric process. The relation $\omega_p=\omega_s+\omega_i$ reflects the energy conservation rule.

The optical parametric amplification process is similar to DFG in terms of the energy conservation. A representation of this process is shown in Figure 9 (see the right panel). The higher energy photon $\hbar\omega_p$, referred to as the pump, is converted into two photons with lower energies, $\hbar\omega_s$ and $\hbar\omega_i$, where one of them with the higher frequency is traditionally called signal and another with the lower frequency is called idler. The parametric amplification process is schematically presented in the Figure 10. The intense pump laser pulse is propagating in the nonlinear crystal in the presence of a weak laser pulse, referred to as the *seed*. If the spatial and the time overlap between the pump and the seed pulses is achieved and the phase-matching condition is fulfilled, the energy from the intense pump beam can be efficiently converted into energy of the signal and idler beams. The phase matching can be achieved here by choosing the orientation of the optical axis of the nonlinear crystal with respect to the polarization of the incident laser light. Figure 11 shows that the rotation of the BBO crystal axis by only ~3°, in the range of the crystal angle between 25.5° and 28.5°, can cover the wavelength range of

parametrically generated light between 1200 nm and 2200 nm when a pump beam of 800 nm wavelength is applied.

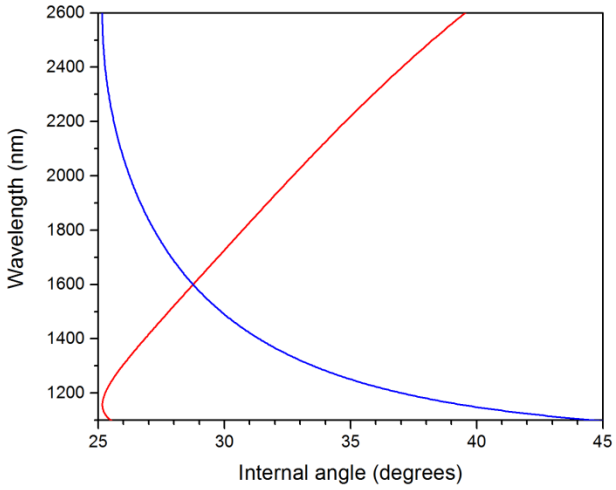

Figure 11. Calculated wavelengths of the signal and idler beams generated in a collinear parametric amplification process induced in a type II BBO crystal by a pump beam of 800 nm wavelength and their dependency on the internal angle of the crystal. The red curve represents the signal beam and the blue curve represents the idler beam. The calculations were performed with the use of SNLO software [SNLO nonlinear optics code available from A. V. Smith, AS-Photonics, Albuquerque, NM].

3.1.3 Optical Kerr-effect

Among the third-order nonlinear processes, the optical Kerr effect plays an important role in the scope of this work. This effect consists of a change of the refractive index as a linear function of the intensity of the light propagating through the optical media. It can be described by the equation:

$$n = n_0 + \beta I \,, \tag{7}$$

where n_0 represents the linear refractive index and βI represents the nonlinear second-order term of the refractive index which is proportional to the laser intensity *I*. This nonlinear term becomes important only at high optical intensities, and the value of critical intensity depends on the properties of the optical media, specifically χ_3 (see Equation (3)). The optical Kerr effect is an origin of two other effects: *self-focusing* and *self-phase modulation*, both of which are relevant to the operation of the laser setup in the present work.

The spatial intensity distribution of the laser pulse is commonly described by a Gaussian envelope. It means that the intensity in the center of the beam is higher than on the sides and, according to Equation (7), the refractive index is also higher in the center. It leads to the distortion of the wavefronts and the media starts acting like an optical lens. This effect is called self-focusing and is widely used in laser systems to generate ultrashort laser pulses. Namely, the method of passive mode-locking commonly applied to synchronize generated modes in a laser oscillator is based on the optical Kerr-effect. It can be understood in terms of energy losses of a pulse propagating in the resonator cavity and passing through an aperture. A shorter pulse possesses a higher peak intensity and, therefore, it experiences a stronger self-focusing and consequently less losses on the aperture. This ultimately leads to generation of short pulses.

Another consequence of the nonlinear modification of the refractive index can be the time domain and is significant for ultrashort laser pulses, where the intensity is inhomogeneously distributed in time. The phase modification induced by the nonlinear refractive index can be described as follows:

$$\Delta\varphi(x,t) = \frac{\omega_0}{c}\beta I(t)x\,, \tag{8}$$

where $\Delta\varphi$ represents a difference in the temporal phase of the electromagnetic wave as a function of the propagation coordinate x and the local time of the laser pulse, *t*. This self-phase modulation can be used for the generation of a supercontinuum, a process also known as a white light continuum. In 1970 Alfano and Shapiro demonstrated this effect for the first time in some crystals and glasses [99]. The ultrashort, white light pulses can cover wavelengths ranging from the UV to NIR [100], and nowadays are commonly applied as a seed in optical parametric amplifiers [101] and as probe pulses in broadband transient absorption spectroscopy [102, 103]. From the other side, the consequences of the optical Kerr-effect can be disturbing, since it can lead to the unwanted modulations of the laser pulse in the spectral and time domains. Therefore, this effect represents an important issue, which should be taken into account in the design of optical setups employing high-power laser sources. To avoid possible problems caused by the Kerr-effect, the peak intensity of the laser pulse can be decreased by increasing the laser beam diameter.

3.1.4 Dispersion of optical pulses

A laser pulse is typically described by a product of a harmonic function, which represents the time-dependent optical oscillation of the electric field, and the Gaussian envelope function, which represents the time-dependent intensity distribution of the laser field:

$$E(t) = \mathrm{Re}\left(E_0 \cdot exp[i\omega_0 t] \cdot \exp\left[\frac{-t^2}{2\tau^2}\right]\right), \tag{9}$$

where E_0 is the amplitude of the electric field, ω_0 is the central (carrier) frequency, and τ is the width parameter of the Gaussian envelope. The pulse duration $\Delta\tau$ of the Gaussian pulse is defined by the full width at half maximum (FWHM) of the intensity profile and can be calculated as $\Delta\tau = \tau \cdot 2\sqrt{\ln 2}$. The relation between the spectral width $\Delta\omega$ (FWHM of the spectral intensity envelope) and the pulse duration $\Delta\tau$ can be expressed by the following uncertainty:

$$\frac{\Delta\omega}{2\pi} \cdot \Delta\tau \geq K\,, \tag{10}$$

where *K* is a numerical constant, which is equal to 0.441 for Gaussian profiles. When the minimum of the product of the bandwidth and the pulse duration is achieved, the pulse is considered to be *bandwidth-limited* or *transform-limited* [104]. By measuring the spectral width of the laser beam and considering the equality relation in Equation (10), the minimal possible value of the pulse duration can be easily estimated.

To consider how the spectral content of the laser pulse is changing during the pulse propagation over the distance z in the dispersive medium, one can apply a Fourier transformation to the time envelope of the pulse. The result can be written as:

$$E(z,\omega) = A \cdot \exp\left[-\frac{1}{2}(\omega - \omega_0)^2\tau^2\right] \cdot \exp[-ik(\omega)z]\,, \tag{11}$$

where the frequency-dependent propagation factor is given by $k(\omega) = n(\omega)\omega/c$. The pulse dispersion can be presented by a Taylor's series of $k(\omega)$ expanded in the vicinity of the central frequency ω_0:

$$k(\omega) = k(\omega_0) + k'(\omega_0)(\omega - \omega_0) + \frac{1}{2}k''(\omega_0)(\omega - \omega_0)^2 + \cdots \qquad (12)$$

The third term in Equation (12) is known as group velocity dispersion (GVD) with the coefficient:

$$k''(\omega_0) = \frac{\mathrm{d}^2 k(\omega)}{\mathrm{d}\omega^2}\bigg|_{\omega_0} = \frac{\mathrm{d}}{\mathrm{d}\omega}\frac{1}{v_{gr}} = \frac{\lambda^3}{2\pi c^2}\frac{\mathrm{d}^2 n(\lambda)}{\mathrm{d}\lambda^2}, \qquad (13)$$

where $v_{gr} = \mathrm{d}\omega/\mathrm{d}k$ is the group velocity value and λ is the wavelength of the laser light. Practically, GVD means that the spectral components of the laser pulse propagate through a dispersive medium with different velocities. The dispersion gives rise to a phase modulation, known as chirp. Positive GVD ($k''(\omega_0) > 0$) causes positive chirp or *up-chirp*: the spectral components of the pulse with the longer wavelengths propagate faster than the components with shorter wavelengths (see Figure 12 for illustration). Negative GVD ($k''(\omega_0) < 0$) causes negative chirp or *down-chirp*: the spectral components with the shorter wavelengths propagate faster [104]. As a consequence of this material-dependent effect, the pulse duration can be significantly increased or decreased. Since the laser pulse duration is a crucial parameter for time-resolved experiments, GVD should be taken into account when choosing the optical components for the experimental setup.

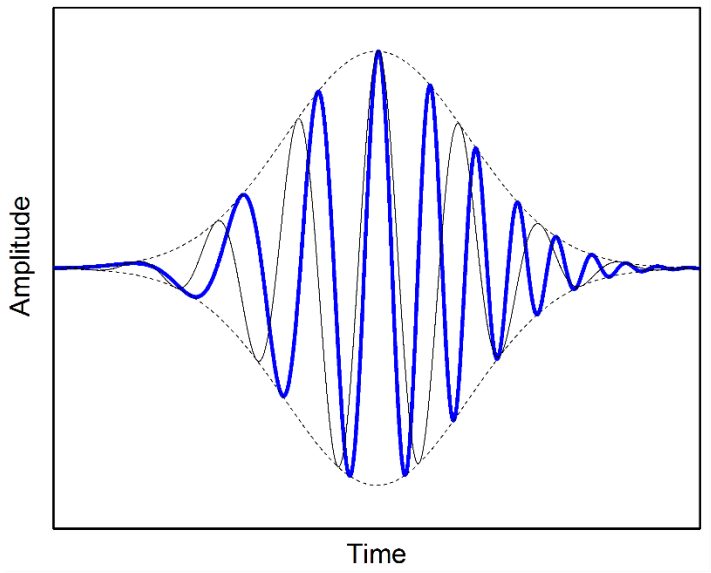

Figure 12. Chirped laser pulse. Blue curve denotes the up-chirped laser pulse in the time domain. Black curve denotes the unchirped pulse with the same pulse duration.

3.1.5 Generation of high-order harmonics

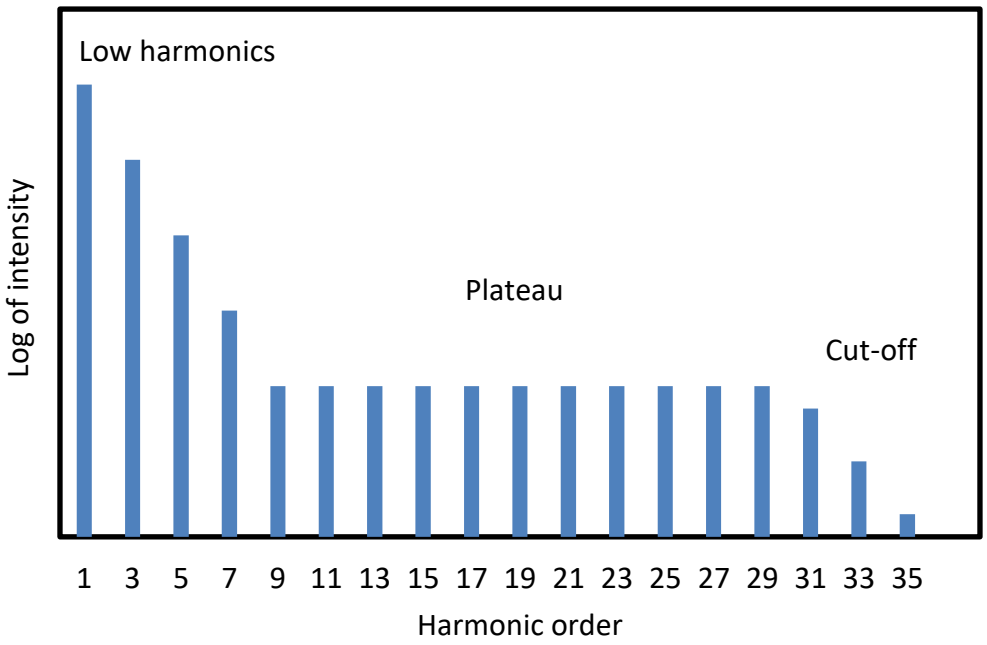

Figure 13. Schematic representation of a typical HHG spectrum. The vertical axis is shown on a logarithmic scale. For the low harmonics in the perturbative regime, the HHG intensity decreases rapidly with the harmonic order. For the higher harmonics, the spectrum exhibits a plateau followed by a pronounced cut-off.

A HHG setup represents a powerful table-top source of coherent XUV and soft X-Ray light with the pulse duration suitable for studying ultrafast processes in molecules. Both the size of the setup and the short pulse duration represent a big advantage in comparison with bulky and very expensive synchrotron and free electron laser facilities. The first observation of high-order harmonics generation (HHG) was reported in 1977 [105]. It was achieved in the perturbative regime of the laser intensity. HHG was initiated in a plasma by focusing of a nanosecond laser pulse onto a solid aluminium target. The further development of laser technology enabled the application of much higher intensities (due to the availability of much shorter pulses) and, thereby, led by the late 1980s to a variety of successful HHG experiments on noble gases [106, 107]. The results of these experiments indicated that a new strong-field, nonperturbative regime was reached [104]. A typical spectrum of high-order harmonics, obtained by focusing an intense laser pulse in a noble gas, is schematically presented in Figure 13. The spectrum consists of odd harmonic peaks, separated by twice the photon energy of the fundamental laser beam. The low-order harmonics arise in the perturbative regime and exhibit a rapid decrease of intensity with increasing of the harmonic order. This decrease occurs typically

up to the 7th or 9th harmonic with 800 nm driving laser wavelength, and beyond this range the HHG signal forms a plateau of peaks with approximately equal amplitudes. The spectral range covered by the plateau depends on the pump pulse parameters, such as the wavelength and the peak intensity, and can extend over 500 eV [108]. This spectral plateau is a signature of the nonperturbative interaction regime of the laser field with the nonlinear medium [109]. In the high-order region, the signal exhibits a well-defined cut-off.

The single-oscillator HHG process can be described by a simple semiclassical model, also known as "three-step model" [104, 109, 110]. In this model, the process is divided into the three following steps:

Step 1: Tunnel ionization. As the initial condition, the active electron is located in the Coulomb potential of the parent atom. The external electric field of the laser $\vec{E}(t)$ induces an additional potential, which is superposed with the atomic potential. Thus, the modified potential experienced by the active electron has the form:

$$V(\vec{r},t) = -\frac{e^2}{4\pi\epsilon_0 r} + e\vec{E}(t)\vec{r}\,, \tag{14}$$

where the first term represents the Coulomb potential, and the second term represents the potential energy due to the electron interaction with the laser field. In Equation (14), r denotes the distance between the core of the atom and the electron. Thus, the presence of a strong electric field leads to the tilting of the potential, as shown in the Figure 14(a), and gives rise to the probability of tunnel ionization. Tunnel ionization removes the electron from the atom and, as an approximation, the electron can be considered as a free particle in the presence of the external electric field.

Step 2: Electron acceleration in the laser field. The oscillating electric field changes direction, which leads to the acceleration of the electron. During the electron drift in the presence of the electric field, the electron can gain a significant amount of kinetic energy. The motion of the electron as well as the energy obtained during this motion is strongly dependent on the phase of the external electric field at the moment of tunnel ionization. With the electric field $E(t) = E_0 \cos(\omega t + \varphi)$, where E_0 denotes the amplitude of the field and φ denotes the phase of the field, the motion of the electron can be described by the following equations for the velocity $v(t)$ and the position $x(t)$ of the electron along the laser polarization axis:

$$v(t) = \int_0^t -\frac{e}{m_e} E(t')\mathrm{d}t' = -\frac{E_0 e}{m_e \omega}(\sin(\omega t + \varphi) - \sin\varphi)\ , \qquad (15)$$

$$x(t) = \int_0^t v(t')\,\mathrm{d}t' = \frac{E_0 e}{m_e \omega^2}\big((\cos(\omega t + \varphi) - \cos\varphi) - \omega t \sin\varphi\big)\,. \qquad (16)$$

The initial magnitudes of the position and the velocity of the electron are considered to be zero ($v(t=0)=0,\ x(t=0)=0$). The constants e and m_e denote here the elementary charge and the electron mass, respectively, and ω represents the angular frequency of the laser field. The time-independent term in the Equation (15) represents the drift velocity.

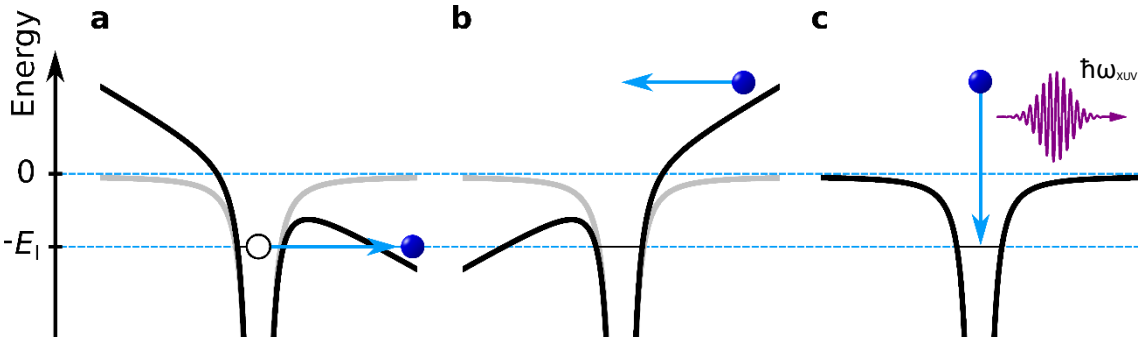

Figure 14. Schematic representation of the three-step model of HHG: (a) tunnel ionization from the distorted atomic potential, (b) acceleration of the electron by the electric field of the laser, (c) Recombination of the electron with the parent atom and emission of an XUV photon with frequency ω_{XUV}. For a, b, and c: blue ball denotes the electron; black curve denotes the atomic Coulomb potential; E_I denotes the ionization potential.

Step 3: Electron recombination with the parent core. Driven by the external field, the electron can return back to the atomic core. The moment of the return can be found as a root of the equation $x(t) = 0$. During the electron recollision with the atomic core, it can be recombined with the parent ion, leading to the emission of a high-energy photon. The energy of the photon represents a sum of the ionization energy E_I (ionization potential) from the first step and the kinetic energy E_kin gained during the motion in the electric field in the second step:

$$\hbar\omega_\mathrm{XUV} = E_\mathrm{kin} + E_\mathrm{I}\,. \qquad (17)$$

The validity condition for this semiclassical model is described by the following relation between the photon energy $\hbar\omega_l$ of the pump laser pulse, the ionization potential E_I, and the ponderomotive energy U_p:

$$\hbar\omega_l \ll E_I \ll U_p\,, \tag{18}$$

which also defines the so-called tunneling regime of ionization. The ponderomotive energy represents the average kinetic energy of a free electron in the oscillating electric field. For the laser field of frequency ω_l and of electric field amplitude E_0, it has the form:

$$U_p = \frac{e^2 E_0^2}{4 m_e \omega_l^2} \tag{19}$$

For a quantitative characterization of the tunnel regime of ionization, one can use the parameter

$$\gamma = \sqrt{\frac{E_I}{2U_p}}, \tag{20}$$

introduced by Keldysh in 1965 [111], and now called the "Keldysh parameter". For tunnel ionization, the condition $\gamma \ll 1$ must be satisfied with $\hbar\omega_l \ll E_I$, ($\gamma \gg 1$ corresponds to the multiphoton ionization regime) [110].

The ponderomotive energy represents an essential parameter used to characterize the electron kinetic energy at the moment of its recollision with the core. The maximum value of E_{kin} can be determined by finding roots of the equation $x(t) = 0$, which describes the electron return to the initial position for a given phase φ of the external field, and by calculating the return kinetic energy $m_e v^2(t)/2$ (see Equation (15) for $v(t)$) for different phases. As shown in the Figure 15, the analysis of these trajectories reveals that the maximum return kinetic energy is ~$3.17U_p$, and the cut-off law for single-oscillator HHG can be thereby expressed as:

$$E_{cut-off} = 3.17U_P + E_I \tag{21}$$

From the relation given above, one can see that both the ponderomotive energy and the ionization potential of the atom are the key parameters for the HHG process, where the

former represents the characteristics of the laser field and the latter represents the characteristics of the non-linear medium.

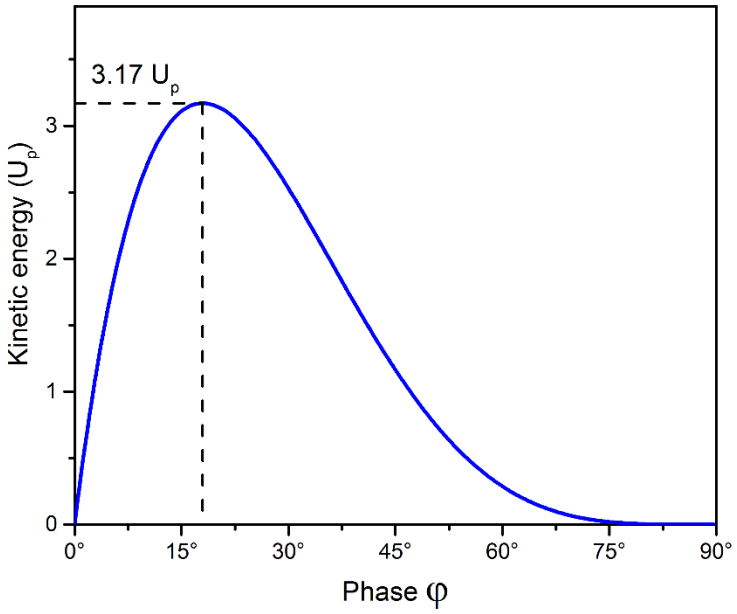

Figure 15. The dependency of the return kinetic energy on the phase φ of the external electric field.

The phase-matching condition is another important issue that needs to be taken into account. This condition implies that the harmonic waves generated at different positions in the generating medium interfere constructively with each other, leading to the increase of the harmonic intensity. The phase-matching condition of the HHG process can be expressed as follows:

$$\Delta k = nk(\omega_1) - k(n\omega_1) = 0\,, \tag{22}$$

where n is the order of generated harmonic and $k(\omega_1)$ and $k(n\omega_1)$ are the wavevectors of the laser and n^{th} harmonic beam, respectively. The Equation (22) is given in a scalar form, corresponding to the collinear geometry of the HHG and the pump beams. The dependency of the wavevector on frequency involves a variety of dispersion effects appearing during the HHG process. First, the gas used as the medium for HHG exhibits dispersion - the dependency of the refractive index on the frequency of the laser light. This leads to the change of the wavevector by Δk_{disp}. Second, since a large amount of electrons ejected from the parent atoms don't recombine with the residual ion, as described in the third step of the three-step model, the generated plasma gives rise to a

collective plasma resonance. It leads to a second change of the wavevector, $\Delta k_{\mathrm{plasma}}$, originating from the plasma dispersion. Additionally, the focusing and propagation geometry of the pump laser beam causes a geometrical change in the wavevector, Δk_{geom}. Adding up all three contributions, the wavevector mismatch can be represented as follows:

$$\Delta k_{\mathrm{total}} = \Delta k_{\mathrm{disp}} + \Delta k_{\mathrm{plasma}} + \Delta k_{\mathrm{geom}}\,, \tag{23}$$

where $\Delta k = nk(\omega_{\mathrm{l}}) - k(n\omega_{\mathrm{l}})$ is valid for every summand. The wavevector mismatch contributions are discussed in details in Ref. [110]. In order to fulfill the phase-matching condition, $\Delta k = 0$, all phase-mismatch contributions should compensate each other. In this case, the most efficient conversion of the laser light into the high harmonic radiation can be achieved.

A modern HHG setup typically consists of an ultrashort laser pulse source, the output of which is focused onto a noble gas target located in a vacuum chamber. The gas target can have the form of a gas jet or a gas cell, or it can be a gas-filled capillary. Vacuum conditions are necessary for the propagation of the emitted XUV light to the interaction region of the experimental chamber. Typical peak intensities at the focus of the pump laser beam used for the HHG process are of the order of 10^{14} W·cm^{-2}. A specific harmonic can be selected with the use of a monochromator. The optimization of the setup performance accrues by means of adjustment of parameters affecting the phase-mismatch contributions described above. This includes the adjustment of the position of the focus waist in the conversion medium and tuning of the backing gas pressure of the gas jet or the gas pressure in the gas cell or capillary. The plasma density can be optimized by tuning the laser power and pulse duration.

3.2 Photoelectron Spectroscopy

3.2.1 Basics of Photoelectron Spectroscopy

Photoelectron spectroscopy (PES), also known as photoemission spectroscopy, is a widely used spectroscopic method, based on the photoelectric effect explained by Albert Einstein in 1905 in terms of quantum mechanics. The basic principle of PES consists of ionization of the gas, liquid or solid sample by UV, XUV or X-Ray radiation and the

detection of the ionized electrons. Recording the energy-resolved (as well as angle-resolved) distributions of unperturbed photoelectrons provides the information necessary to determine the binding energies (and the angular momentums) of occupied bound states and thereby to reveal the electronic structure of the sample. Depending on the energy of the incident photons, the photoemission can occur from the valence states of the sample at low photon energies and from both the valence and core states of the sample at high photon energies. The photoionization of the core-level electrons leads to a vacancy in the core shell, which in turn can be filled by an electron from the upper occupied energy level, leading to the release of energy. The released energy can be transferred to another electron, initiating an ejection of this second electron from the atom which also contributes to the photoemission. The secondary ejected electron is called an Auger electron. For the description of the photoemission process in dense media, a three-step model is commonly used in the literature [112-114]:

(1) photoexcitation of an electron in the bulk of the sample by absorbing a photon,
(2) motion of the photoexcited electron through the bulk to the surface of the sample,
(3) escape of the electron from the sample surface into vacuum.

In first-order perturbation theory, the probability of the photoexcitation of an electron per unit time from the initial state *i* is given by the Fermi's golden rule [112-114]:

$$W \propto \frac{2\pi}{\hbar} \left|\langle \Psi_f | \hat{V} | \Psi_i \rangle\right|^2 \delta\left(E_f - E_i - \hbar\omega\right), \tag{24}$$

where Ψ_i and Ψ_f are the electron wave functions of the initial and the final state, respectively, E_i and E_f are the energies of these states, $\hbar\omega$ is the photon energy, $\hat{V}$ represents the dipole operator of the electron interaction with the external field. The delta function $\delta\left(E_f - E_i - \hbar\omega\right)$ in the Equation (24) reflects the energy conservation rule. If the length gauge is used to describe the interaction with the electromagnetic field, the dipole operator has the form of the scalar product, $\hat{V} = e\vec{E} \cdot \vec{r}$, where $\vec{E}$ is the electric field amplitude and $\vec{r}$ is the vector of spatial coordinates.

The kinetic energy of the ejected electron carries the information about its binding energy in the sample, which can be expressed by the simple equation:

$$E_{\text{kin}} = \hbar\omega - E_{\text{B}} - \phi\,, \tag{25}$$

where E_B is the binding energy and ϕ is the work function of the sample. However, the work function is only relevant for the solid and liquid samples and should be omitted for gases, while the extraction of the work function of a liquid sample is a complex issue and is the subject of ongoing research [115]. The Equation (25) reflects the energy conservation, whereas the binding energy is defined by the difference $E_B = E_{N-1} - E_N$, where E_N and E_{N-1} are the total energies of the initial state with N electrons and final state with N-1 electrons, respectively. The distribution of the measured kinetic energies of the photoionized electrons forms a photoelectron spectrum, where each spectral component reflects the binding energy of a particular state which is initially occupied and is accessible to ionization by photons of energy $\hbar\omega$. One can consider that the ionization process maps the electron population distribution among bound states into the kinetic energy spectrum of photoelectrons.

3.2.2 Photoemission Analysis Techniques

There are three basic techniques which can be applied to analyze the kinetic energy of electrons produced in a photoionization process:

(1) the deceleration of the charged particles by a retarding electric field,

(2) the change of the trajectory of a particle via applying an electric or magnetic field,

(3) the time-of-flight (TOF) technique.

The technique (1) was employed at the early stages of the development of PES [112, 113] in retarding-type analyzers. The analyzers of this type had a very simple construction and the energy spectrum could be only derived by differentiating the measured signals while changing the retardation voltage [112]. Retarding-type analyzers became outdated and were replaced by more advanced analyzers employing methods (2) and (3). The deflection type analyzers are based on the technique (2) and exist in three common configurations: plane mirror analyzer (PMA), cylindrical mirror analyzer (CMA) and hemispherical analyzer, which differ in the geometry of the applied field which deflects electrons. The hemispherical analyzer is the most popular variant of them. The hemispherical analyzers consist of two electrodes in the form of concentric hemispheres. The spectrum can be recorded by varying the voltage between the electrodes, though it leads to the change in the energy resolution. In order to keep the resolution constant during the measurement, a combination of a several electrostatic lenses is usually applied between the sample and the analyzer entrance. The photoelectrons at the exit of the hemispheres are detected with

the use of a multichannel plate (MCP). MCPs represent a special type of electron multiplier. The main requirement for a good performance of MCP is that the work function should be equal for the entire active area of electron detection. MCPs can be used in combination with a phosphor screen and a CCD camera, providing the position sensitivity of the particle detector, or alternatively an anode-collector. The electron detector is electronically connected to a computer with suitable data acquisition hard- and software. The application of the hemispherical analyzers is particularly suitable for steady-state PES measurements with a high energy resolution. For all types of analyzers, the high vacuum conditions are obligatory to minimize the probability of the scattering of photoelectrons on the residual-gas particles on the way from the interaction region to the electron detector of spectrometer. Another requirement on the photoelectron spectrometers is the protection of the electron propagation region from the influence of magnetic fields, e.g. the Earth field or other external fields which can be produced by scientific equipment in the laboratory environment. This problem is usually solved by using μ-metal screening or by application of Helmholtz coils for compensation of external magnetic fields. The photoelectron spectrometer, which was used in the experiments presented in this work, is based on the TOF technique (3) and represents an alternative to the above described deflection type analyzers. It will be presented in detail in the following section.

3.2.3 Time-of-Flight Spectroscopy

In the simplest construction of a TOF analyzer, a photoelectron ejected from the sample by a light pulse drifts in a field-free environment to the detector, where its arrival time can be recorded. This spectroscopy technique is applicable when using pulsed sources of radiation such as synchrotron sources (operating in a “single bunch” mode [113]), free electron lasers, HHG-based XUV pulse sources, or pulsed lasers. The time window between the radiation pulses should be sufficiently long in order to detect photoelectrons in a wide range of arrival times corresponding to a wide range of their kinetic energies. The kinetic energy E_{kin} of photoelectrons can be directly determined from the arrival time t according to the following equation:

$$E_{\mathrm{kin}} = \frac{m_e}{2}\frac{L^2}{(t-t_0)^2}, \tag{26}$$

where t_0 is the time of the interaction event between the light pulse and the sample, m_e is the electron mass, and L is the length of the spectrometer. The fact that the TOF measurements take place in a time domain leads to two important advantages of TOF analyzers in comparison to deflection type analyzers [116]. The first advantage is the relatively low background noise, which is equally distributed over the whole spectrum. The second advantage is the possibility to record the full spectrum simultaneously. The latter advantage makes TOF spectroscopy especially attractive for time-resolved experiments.

The energy resolution of the TOF analyzer depends on three uncertainties: in the flight time $(t - t_0)$ of the electrons, in the length L of the drift path of the electrons from the sample to the detector, and in the wavelength λ of the ionizing radiation [117]. It can be expressed by the following equation:

$$\frac{\Delta E}{E} = \sqrt{\left(\frac{2\Delta(t - t_0)}{t - t_0}\right)^2 + \left(\frac{2\Delta L}{L}\right)^2 + \left(\frac{\Delta\lambda}{\lambda}\right)^2} \qquad (27)$$

The uncertainty in the spectrometer length L can be reduced to some extent by calibration of the energy scale of the spectrometer. The calibration procedure consists of detection of electrons generated with a well-known kinetic energy. Ionization of a noble gas by monochromatized light is usually used for this purpose.

As a common configuration, a TOF spectrometer consists of a drift tube equipped with a skimmer with a small orifice (which should be close to the light-source-sample interaction region) an electron detector at the end of the drift tube, and connections to the vacuum pumps providing the high vacuum conditions during the experiment. Similar to hemispherical analyzers, a combination of MCPs with a phosphor screen and a CCD camera or with an anode-collector can be used as a detector in TOF spectrometers. The electron collection efficiency can be increased by applying a non-uniform magnetic field, like for example in a magnetic bottle type spectrometer described in Ref. [118]. Alternatively, the collection efficiency and the energy resolution can be improved with the use of electrostatic lenses. In the classical field-free TOF spectrometers, the typical energy resolution is moderate in comparison with the resolution of hemispherical analyzers. However, novel design of electrostatic lenses, applied in the latest generation of TOF spectrometers, allowed to be achieved energy resolutions comparable to that of hemispherical analyzers.

3.2.4 Angular Distribution of Photoelectrons

The angular distribution of directly photoemitted electrons from randomly oriented molecules in a gas phase sample by linearly polarized light is described by the standard equation for the differential cross section of ionization [114, 119, 120]:

$$\frac{\mathrm{d}\sigma}{\mathrm{d}\Omega} = \frac{\sigma}{4\pi}\left[1 + \frac{\beta}{2}\left(3\cos^2\Theta - 1\right)\right], \tag{28}$$

where σ is the total photoionization cross section, Ω the solid angle of detection, Θ is the polar emission angle with respect to the polarization vector of the ionizing light, and β is the anisotropy parameter. The anisotropy parameter is defined by the angular momentum of the ionized states and the states in the continuum spectrum populated in the process of ionization. For a given angular momentum quantum number of the initial bound state, different states of the continuum spectrum can be excited according to the angular momentum selection rules of bound-to-continuum state phototransitions. The outgoing electron wave functions are described by different spherical harmonics. Here the laser polarization direction is commonly considered as the angular momentum quantization axis. The spherical harmonics interfere with each other, whereas their amplitudes are determined by the radial overlap of the wave functions of the initial and final states. In general, since the radial wave function overlap and relative photoemission phases vary with the change in the excitation level in the continuum spectrum, the anisotropy parameter is a function of the electron kinetic energy. It can acquire values in the range between -1 and 2. Figure 16 shows the photoelectron angular distributions for a chosen set of values of the anisotropy parameter, $\beta = -1, 0, 1, 1.5, 2$. This figure demonstrates that the photoemission occurs preferentially along the laser polarization axis for positive values of β, and perpendicular to the laser polarization for $\beta < 0$. One can easily derive from Equation (28) that the angular-dependent term of the differential cross section is independent of the anisotropy parameter at $\theta = 54.7°$, which is called the "magic angle". At this angle, the angular-dependent factor of the photoemission yield is equal for all ionization channels involving different initial states. However, in the experimental setup presented in this work the light polarization is parallel to the spectrometer axis and, thus, the photoelectrons are detected at emission angles close to $\theta = 0°$.

The application of modern 2D photoelectron detectors in hemispherical or TOF analyzers allows us to gain information about the angular distribution of the photo-

electrons and represents a technical solution for angle-resolved PES studies. This method enables simultaneous measurement of both the binding energy and the angular momentum of electrons. Angle-resolved PES is of particular interest for the experiments on solid samples possessing a periodic structure, but also for experiments with liquid samples with randomly oriented molecules in the bulk and possible structural order on the surface. The experiment of Thürmer at al. [120], accomplished with the use of angle-resolved PES, shows that the description of the angular distribution of photoelectrons for a gas-phase sample, presented above, is also valid for s-orbitals of oxygen in liquid water.

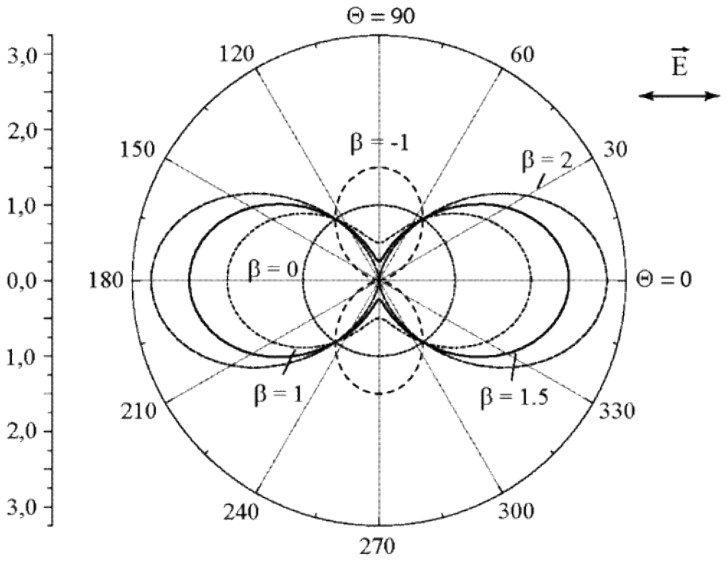

Figure 16. Angular distributions of photoelectrons for different values of the anisotropy parameter ($\beta = -1, 0, 1, 1.5, 2$) generated by linearly polarized light. The polarization axis of light is denoted by $\vec{E}$. Reprinted with permission from the Ref. [114]. Copyright 2006 American Chemical Society.

3.2.5 Time-Resolved Photoemission Spectroscopy

Time-resolved photoemission spectroscopy (TRPES) is a method, which enables vibronic dynamics to be monitored in gas, liquid or solid samples. Modern experimental apparatuses allow temporal resolutions down to a few hundreds of attoseconds to be achieved [121]. Experimentally, this method involves the conventional pump-probe configuration employing synchronized pulsed light sources. The pump pulse initiates changes in the electronic structure of the sample, like, for example, excitation of a nonstationary electronic state. The probe pulse generates a photoelectron spectrum by

ionization of the photoexcited sample at a given time delay. The time delay results from the difference between arrival times of the pump and probe pulses. The photoelectron spectra recorded as a function of time delay reflect the changes in the distribution of kinetic energies of electrons and, thereby, reveal the evolution of the electronic population of states in the sample after the photoexcitation event. The principle of the TRPES is schematically presented in Figure 17.

In the quantum-mechanical approach, TRPES can be described as a generation of an excited state wavepacket by the pump pulse. The evolution of this wavepacket can be interrogated using a time-delayed probe pulse, which projects the evolving wavepacket onto a set of final states. Furthermore, two important approximations are considered in the context of the TRPES measurements. The first one is the Born-Oppenheimer approximation, which is applied to separate slow nuclear dynamics and the fast dynamics of electrons. The second one, the Koopmans approximation, assumes that the orbital energies in the residual ion after the photoionization remains unchanged after the photoionization event. This leads to the concept of Koopmans correlations: the removal of an electron from an atom or molecule due to ionization leads to formation of a specific cation with a correlated "one-electron-less" configuration. Due to multiple ionization channels correlating with each electronic state, each of these states is represented by a set of peaks in the photoelectron spectrum recorded at the chosen time delay position. The intensities of these peaks differ according to the nature of the initial molecular orbitals and the final states of the ejected electrons. It makes the interpretation of the spectra especially, for large molecules, a very complicated issue. Thus, ideally, the TRPES experiments should be supported by the theoretical calculations.

The sensetivity of the TRPES method to both electronic and vibrational dynamics, makes it an especially powerful tool for studying non-adiabatic processes in molecules and, thus, highly suitable to achieve the scientific objectives which were presented in the introduction (Chapter 1) to this work. An extensive description of the TRPES method can be found i.e. in the review article by Albert Stolow and co-workers [122].

The most common type of analyzer in such experiments is the TOF spectrometer with enhanced collection efficiency, such as, for example, the magnetic bottle type spectrometer [118]. The time resolution is limited by the duration of the pump and probe pulses. The current advances in laser technology allow measurements with a femtosecond time resolution.

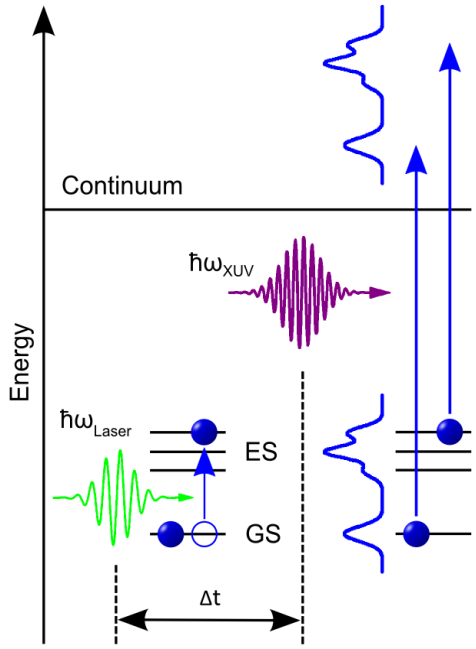

Figure 17. Illustration of the principle of TRPES: the optical pump pulse transfers a portion of the electron population from the initial ground state (GS) to an excited state (ES) of the molecular complex; applied at a variable time delay Δt, the XUV probe pulse maps the electronic spectrum of bound states (blue curve) to the kinetic energy spectrum of photoelectrons.

3.2.6 Space-charge effect

Space-charge effect is one of the most important issues, which needs to be taken into account in TRPES experiments. Practically, the effect manifests itself as a positive or negative time-dependent kinetic energy shift and broadening of the spectral components. The shift is defined as a difference in the position on the kinetic energy scale of a certain spectral component, measured in the pump-probe configuration, as compared to its initial energy position in a probe-only measurement. Since these changes in the spectra could overlap with the transient signal, the issue represents a serious problem and should be considered in the data analysis. The origin of the effect lies in the local electrostatic charge induced by the pump and probe beams at the sample surface. The electrostatic interaction between the charged sample and the cloud of electrons ejected during the photoionization process, as well as the interaction between the electron clouds produced by the pump and probe beams in a pump-probe experiment, lead to a change of the initial value of the photoelectron kinetic energy. The space-charge effect can also occur in solids without photoemission, when the light causes a surface photovoltage in the sample [123, 124]. However, the effect of this type is not relevant to this work and

will be not discussed further. The space-charge effect was extensively studied in the gas and solid samples with the use of a single laser pulse [125-128] and in the solid samples in several TRPES experiments with the use of XUV [129, 130], soft x-ray [131], and hard x-ray [132] radiation. Recently, it was also reported in a TRPES experiment with a liquid sample, where the UV and XUV laser pulses were employed as a pump and probe, respectively [133]. The latter report is the most relevant, since TRPES on liquids is in the focus of this work.

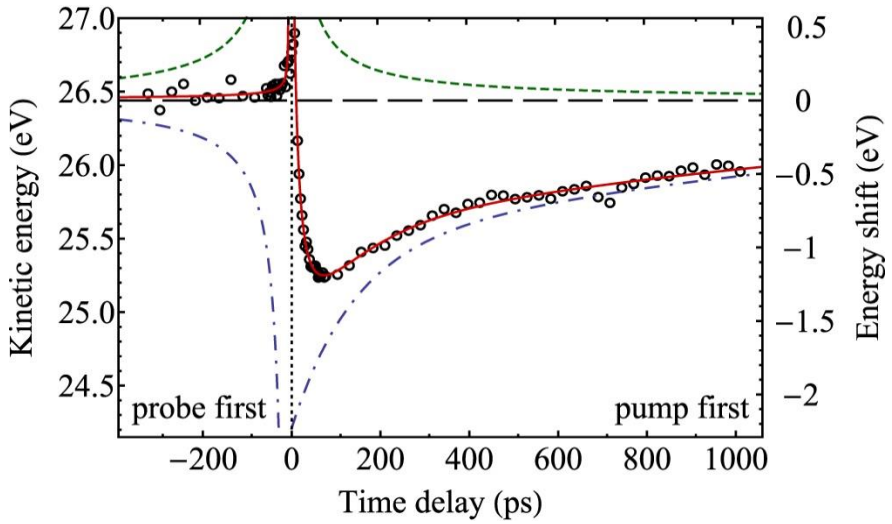

Figure 18. Central kinetic energy of the XUV ionization peak from the Fe 3d(t_{2g}) orbitals of ferrocyanide as a function of time delay between the laser pump and the XUV probe pulses in a TRPES experiment on aqueous solution of $[Fe(CN)_6]^{4-}$, performed by Al-Obaidi *et al.* [133]. An XUV photon energy of 32.55 eV was applied in the experiment. Experimental data are shown by circles. The dashed horizontal line indicates the peak position obtained without applying the pump pulse. The vertical scale on the right hand side provides a measure of the spectral energy shift due to the space-charge effect. The red curve represents the fit of experimental data to the classical model described in this chapter. Calculated individual contributions from the negative and positive charge effects are represented by green (dashed) and blue (dotted–dashed) lines, respectively. The figure is reprinted from Ref. [133].

The central kinetic energy of the chosen spectral peak in the TRPES experiment with the liquid sample, plotted as a function of time delay, typically exhibits a positive shift at negative values of time delay (see Figure 18). A negative delay means that the probe pulse arrives to the interaction region before the pump pulse. At the zero time delay, the energy shift shows a prominent positive peak, followed by a sudden drop to negative values when the delay becomes positive. At larger positive time delays, the energy shift decreases, indicative of charge dissipation. Eventually, the spectral peak acquires its

initial central kinetic energy in the limit of large positive time delays, which can extend to a nanosecond scale (see Figure 18).

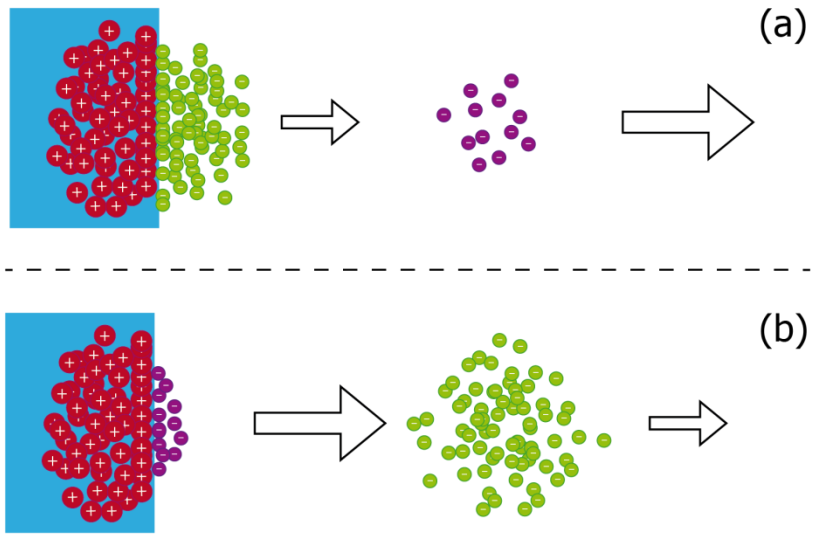

Figure 19. Schematic illustration of the space-charge effect close to the interaction region: (a) Probe pulse interacts with the sample before pump pulse, (b) Pump pulse interacts with the sample before probe pulse.

According to [127, 132, 134-137], the spectral shift produced by the space-charge effect can be predicted by a simple mean-field model. For the laser pump – XUV probe PES on liquid sample, under the assumption that the charge induced at the sample by the XUV pulse in negligible, one can consider two possible cases:

1. In the first case, the probe pulse interacts with the sample before the pump pulse (see Figure 19(a) for illustration), which is the case of a negative time delay. The pump pulse generates an electron cloud due to photoionization in the laser field and this cloud propagates from the sample towards the detector in the far field. Correspondingly, a positive charge is created by the pump pulse on the sample in the interaction region. This leads to the appearance of a positive time-dependent potential on the surface of the sample. At this moment, the electron cloud which was first produced by the XUV probe pulse has been already propagated over a certain distance from the interaction region in the direction of the detector, and this distance is dependent on the time delay. The Coulomb interaction with the positive potential on the surface decreases the initial kinetic energy of XUV electrons. However, the Coulomb interaction between both laser-generated and XUV-generated electron clouds increases the kinetic energy of the XUV

electrons. The sum of these two interactions results in a positive kinetic energy shift of XUV photoelectrons.

2. In the second case, the pump pulse interacts with the sample before the probe pulse, which corresponds to positive time delays (see Figure 19(b) for illustration). Similar to the previous case, the pump pulse produces a cloud of photoelectrons moving away from the interaction region and creates a positive time-dependent potential on the surface of the sample. The latter leads to the reduction of the initial kinetic energy of XUV electrons produced by the probe pulse. On the other hand, the electron cloud generated by the laser pump pulse is significantly slower than the cloud generated by the XUV pulse. Thus, the latter can reach the cloud generated by the pump pulse and passes through it. Thereby, due to Coulomb interaction between the clouds, the electrons generated by XUV radiation are accelerated as in the first case considered above. At short positive time delays, the acceleration effect prevails over the deceleration due to the interaction with the positive surface charge. However, at larger positive time delays the deceleration effect is stronger. The superposition of the interactions occurring at the two pump-probe pulse sequences discussed above results in the time-dependent evolution of the energy shift presented in the Figure 18. The negative energy shift is a special feature of liquid samples in such pump-probe experiments, in contrast to solids where only positive shift could be observed. This is because in the solid samples the positive charge induced by the pump beam quickly dissipated due to the conductive properties of solids.

The intensity dependent studies presented in the Ref. [133] showed that the spectral shift is directly proportional to the amount of electrons ejected due to photoionization by the pump beam. Thereby, the space-charge effect has a nonlinear dependence on the peak intensity of the laser pulse, which is a crucial parameter that determines the probability of multiphoton ionization. Consequently, the space-charge effect strongly depends on the pump pulse energy and the pulse duration. Also, the wavelength of the pump beam can be a crucial parameter. Indeed, the effect is significantly more pronounced for a pump laser beam with a wavelength in the UV range than for a pump beam in the visible range. This subject is further discussed in the Section 5.2.3.

Besides the above described space-charge effect, which is induced by the pump laser irradiation, one should also account for an effect caused by the Coulomb repulsion of electrons within the cloud produced by the probe XUV pulse alone. As a result of this

repulsive interaction, some part of the electrons can be accelerated and some part of them decelerated. Thus, some electrons gain an additional kinetic energy and some of them lose kinetic energy, or are not able to escape the sample at all [138]. This leads to significant broadening of the peaks in the photoelectron spectra. This effect becomes especially important for solid samples, where a huge amount of elections is produced from a very small area on the sample surface. The effect increases with the increasing of the number of photoemitted electrons, as was shown in [127, 139], and, consequently, it depends on the intensity of the incident light. According to theoretical [134] and experimental [127] studies, the broadening of kinetic energy peaks can be described by the relation

$$\Delta E_{\mathrm{kin}} \propto \sqrt{N}\,, \tag{29}$$

where N is a number of electrons photoemitted per laser pulse.

3.2.7 Photoemission in the presence of a strong laser field

Since the peak intensities of the pump laser beam in the time resolved PES experiments can achieve values in the order of hundreds of GW/cm^2, it is meaningful to discuss the most important aspects of photoemission in the presence of the strong laser field. There are two competing effects, which play a role in the experiments presented in this work.

The first effect is called above threshold ionization (ATI) and represents a multiphoton ionization (MPI) process in which an atom absorbs a number of photons which is larger than the minimal quantity necessary for photoionization. The effect is schematically shown in the Figure 20(a) and can be represented by two steps: the initial MPI with n_0 photons needed to bring the electrons to the continuum, and the following redistribution of these electrons in the continuum via “free-free” transitions by absorbing additional photons [140].

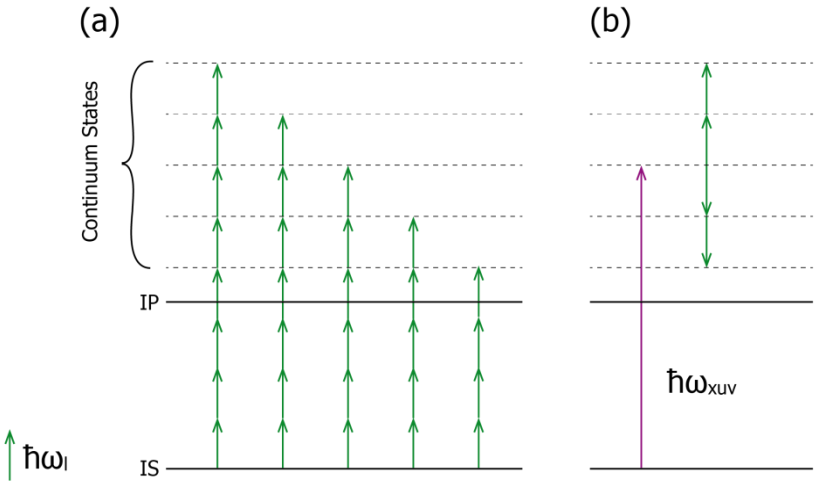

Figure 20. Schematic representation (a) of the ATI process initiated by the pump laser beam with the frequency ω_l and (b) of the LAPE processes initiated by the probe XUV beam with the frequency ω_{XUV} in the presence of the pump laser beam with the frequency ω_l.

After the discovery of ATI by Agostini et al. in 1979 [141], the effect was extensively studied theoretically and experimentally [142-150]. The cutoff for the spectrum of electrons directly emitted to the continuum in the ATI process lies at $2U_p$ [151], and thereby depends on the intensity of the laser field. In general, the condition for ATI can be formulated as a relationship between the ionization potential of the sample E_I, the ponderomotive energy U_p, and the photon energy $\hbar\omega_l$ of the incident light:

$$E_I > U_p > \hbar\omega_l \tag{30}$$

In a TRPES experiment, ATI induced by the pump laser beam with the frequency ω_l leads to the emission of additional energetic photoelectrons with kinetic energy

$$E_{kin} = (n_0 + n')\hbar\omega_l - I_0\,, \tag{31}$$

where I_0 is the (potentially Stark-shifted) ionization potential of the atom, n_0 is the minimum number of the pump laser photons needed to overcome the ionization potential, and n' is the number of additional photons. Signal produced by these electrons can overlap with the signal from photoionization initiated by the XUV probe beam and, therefore, it is important to take ATI into account when performing the experiments.

The second effect deserves more detailed discussion, since it plays an important role in this work, as will be shown in the further chapters. It appears in pump-probe PES experiments by photoionization of the gaseous, liquid or solid samples by a light pulse with high photon energy in the presence of an intense laser field with photon energy significantly lower than the energy of ionizing photons. The effect is referred to as the laser-assisted photoelectric effect or laser-assisted photoemission (LAPE). It was observed for the first time by Glover *et al.* [152] in the photoelectron spectra of helium using a HHG source to ionize the sample in the presence of intense NIR laser light. Apart from the experiments with gases [152, 153], the effect was also studied on the surfaces of solid samples [138, 154, 155]. Analogous to ATI, LAPE can be described in two steps. The first step is represented by a photoemission of the electrons by XUV photons from the initial state in the sample to an excited state in the continuum, where it can be considered as a free electron, under approximation that the influence of atomic potential is neglected. In the second step, a so-called dressing of the exited state by the pump laser field take place (see Figure 20(b)), where the elections undergo free-free transitions. Thus, the elections can be redistributed in the continuum by absorption and emission of laser photons [138]. It leads to the appearance of the side bands in the photoelectron spectrum with kinetic energies shifted by an integer number of photon energies of the pump laser in positive and negative directions from the initial state band, whereas the latter exhibits a depletion of the photoelectron signal. The quantum mechanical treatment of LAPE can be performed by describing the continuum state with a wave function known in the literature as a Volkov function [143]. The Volkov function represents an exact analytical solution of the Schrödinger equation for a free electron in a strong laser field and can be expressed as follows:

$$\psi_{\mathrm{v}}(\boldsymbol{r},t) = \frac{1}{(2\pi)^{\frac{3}{2}}}\exp(i\boldsymbol{p}\cdot\boldsymbol{r})\sum_{n=-\infty}^{+\infty} J_n\left(\frac{\boldsymbol{p}\cdot\boldsymbol{E}_0}{\omega_{\mathrm{l}}^2},\frac{U_{\mathrm{p}}}{2\omega_{\mathrm{l}}}\right)\times \\ \times\exp\left[-i\left(\frac{p^2}{2}+U_{\mathrm{p}}+n\omega_{\mathrm{l}}\right)t\right], \tag{32}$$

where $\boldsymbol{p}$ is the electron drift momentum, $\boldsymbol{E}_0$ is the electric field of the pump laser, U_{p} is the ponderomotive potential, ω_{l} is the frequency of the pump laser, and $J_n(x,y)$ is a generalized Bessel function, where n denotes the number of exchanged laser photons. Transitions from the initial state, described by the electronic wave function Φ_0, to the Volkov states ψ_{v} with a given momentum $\boldsymbol{p}$ can be expressed by the S-matrix:

$$(S-1)_{fi} = -i \int_{-\infty}^{+\infty} \langle \psi_v | \boldsymbol{A}(t) \cdot \boldsymbol{p} | \Phi_0 \rangle \, \mathrm{d}t \,, \tag{33}$$

where $\boldsymbol{A}(t)$ is the vector potential of the laser field. It can be shown that the amplitude A_n of the n^{th} side band, created in the spectrum by absorption or emission of n laser photons, can be described as a ratio of differential cross sections of laser-assisted and field-free transitions, derived from the S-matrix and expressed as follows:

$$A_n = J^2 \left(\frac{\boldsymbol{p} \cdot \boldsymbol{E}_0}{\omega_l^2}, \frac{U_p}{2\omega_l} \right) \tag{34}$$

Assuming the quantum mechanical treatment of the process described above, Saathoff at al. [138] approximated the equation for the amplitude of the first side band as follows:

$$A_1 \propto \frac{I E_{kin}}{\omega_l^4} \tag{35}$$

According to this equation, the amplitude is linearly dependent on laser intensity I and kinetic energy, E_{kin}, of the free electron excited by the XUV photon. Additionally, it follows from the Equation (35) that low-frequency lasers can drive LAPE with a higher efficiency. The relation $A_1 \propto \omega_l^{-4}$ was experimentally demonstrated in [155] on a solid sample.

Since the LAPE requires the simultaneous presence of both the pump and the probe pulses, the effect can be used to define the zero time delay. In practice, it is also widely used to determine the temporal characteristic of the XUV or X-Ray probe pulses via observing their cross-correlation with an IR or a visible laser pulse of known pulse duration.

3.3 Liquid microjet technique

Liquid microjet technique (LMT) represents an experimental approach, which makes it possible to conduct experiments with liquid samples under vacuum conditions. For the first time, PES measurements with liquids in vacuum were reported in 1973 by Hans and Kay Siegbahn [1], where the photoelectron spectrum of $HOCNH_2$ was presented. Later, this technique was elaborated further by Faubel and co-workers [2]. The LMT applied in PES experiments makes the study of the electronic structure and

dynamics of the molecules in solutions possible. This approach is especially valuable for biologically relevant samples, since the liquid phase is their natural environment. Generally, the experimental setup based on LMT consists of a liquid "beam" or a train of liquid droplets, delivered to the interaction region in the experimental vacuum chamber through a thin capillary, and a liquid catcher which prevents the sample from spreading over the entire experimental chamber. In the liquid microjet setup used in the present setup, the liquid sample is pushed through a glass capillary with an orifice of ~20 μm under the pressure of approximately 5-20 bar. These parameters can vary, depending on the viscosity and the vapor pressure of the liquid sample. The stable flow is typically achieved by application of a HPLC or a syringe pump. The liquid enters into the vacuum region with a typical velocity of ~100 m/s, where it forms a ~5 mm long laminar flow region [156]. In this region, the sample acquires a form of a cylinder with a smooth liquid surface, which perfectly suits a PES experiment. After this laminar-flow region, the sample starts to whirl and eventually decays into droplets and becomes unusable. In order to prevent the capillary from clogging, the use of a degasser and micro-particle filters is beneficial for the liquid microjet setup [156]. The liquid introduced to the experimental chamber is usually collected in a cryogenic trap (often called a "cold trap"), where liquid nitrogen is used to cool the steel surfaces of the collector to a cryogenic temperature [157]. Thus, the sample freezes and sticks on the cold surfaces of the trap, alleviating the experimental chamber from its vapors. An application of a vacuum turbo pumps in combination with the cryogenic traps enables us to maintain a pressure in the order of 10^{-5} mbar in the experimental chamber during the operation of the microjet setup. Alternatively to the cold trap technique, the sample can be collected in a liquid microjet recovery system as shown e.g. by Lange *et al*. in Ref. [158]. In such a system, the sample passes through a temperature-controlled copper skimmer with a small orifice of 150 μm, which is connected to a glass reservoir. The skimmer is placed at the end of the laminar flow region of the liquid jet. The construction of the recovery system provides the opportunity to empty the glass reservoir without interrupting the experiment, which is an advantage in contrast to the cryogenic method. The recovery system can be also useful for samples containing expensive materials, since the solution can be reused multiple times. However, in the case of its application to a solvated sample, the concentration of the recovered solution will be changed because of evaporation of solvent in vacuum.

An important aspect of photoemission from the liquid microjet is the influence of the vapor surrounding the liquid jet in vacuum. The spectra obtained from the microjet

include both contributions, from the liquid and from the gas phase of the sample. Depending on the vapor pressure of the liquid, the jet diameter, and the spot size of the incident laser, XUV, or X-ray beams, the contribution of the gas phase can change dramatically. The width of the vapor layer between the jet and the spectrometer entrance is a crucial parameter for detection of the photoelectrons from the liquid phase, since the electrons from the liquid surface can be scattered by the surrounding gas molecules. The necessary condition for effective detection of the photoelectrons from a liquid surface was given by Siegbahn [159], who considered the *Pd* parameter representing the effective vapor layer thickness. Here *P* is the vapor pressure of the sample and *d* is the distance between the liquid surface and the spectrometer entrance. The limiting condition $Pd < 1$ Torr·mm was reported for X-Ray PES and $Pd < 0.1$ Torr·mm for PES with the use of ultraviolet light. For a cylindrical liquid beam, this parameter can be evaluated from the following equation [157]:

$$Pd = \int_{R_{\mathrm{jet}}}^{R_{\mathrm{spec}}} P(r)\mathrm{d}r = P_0 R_{jet}\left(\ln R_{\mathrm{spec}} - \ln R_{\mathrm{jet}}\right), \tag{36}$$

where R_{jet} is the jet radius, R_{spec} is the distance between the center of the jet and the entrance of the spectrometer, and P_0 is the corresponding local equilibrium vapor pressure at the jet surface. In order to decrease the vapor pressure in PES experiments on liquid microjet, the temperature of the sample can be decreased by application of pre-cooling.

The photoelectron emission from the liquid phase of the sample, in turn, has both surface and bulk contribution. This fact leads to the problem related to the possible probing depth in the liquid microjet. The photoelectrons created in the bulk of the sample may undergo a series of elastic and inelastic scattering events [160, 161]. The probability of these events is crucial for determination of the original depth of measured electrons. It varies depending on the sample and the kinetic energy and angular distribution of the photoelectrons. The signal attenuation caused by the elastic and inelastic collisions can be approximately described by an exponential decrease of the photoelectron yield as a function of depth [160]. Two parameters were introduced in the literature to handle the problem quantitatively. The first one is the effective electron attenuation length (EAL), which defines the depth in the bulk from where the yield of photoelectrons maintaining the initial value of the kinetic energy is reduced by a factor of 1/e. The second parameter is the inelastic mean free path (IMFP) – an average length of the path of the electron in the bulk without undergoing an inelastic collision. Thus, the EAL represents the upper

limit for the IMFP. Despite a number of studies being dedicated to this topic [120, 162, 163], the issue is still not completely clarified. However, the recent results of experiments performed with liquid water [120, 163] show that the EAL for the kinetic energies below 100 eV is quite low, of the order of a few nanometers, and not strongly dependent on the value of kinetic energy in this range. Thus, one can expect that the PES experiments with the liquid microjet and the use of UV or XUV light are rather surface sensitive.

Finally, one should mention a problem concerning the practical application of the liquid microjet for PES. The liquid passing the glass nozzle with a high velocity rubs on the nozzle walls, which leads to the charge separation and negative electrostatic charging of the jet. A special type of the surface potential occurs due to this process, called "streaming potential", and contributes to the kinetic energy of the emitted electrons. The streaming potential can be calculated according to following equation [157]:

$$\Phi_{\mathrm{str}} = -\frac{1}{2\pi\epsilon_0}\frac{I_{\mathrm{str}}}{v_{\mathrm{jet}}}\ln\left(\frac{d_{\mathrm{jet}}}{2}\right), \tag{37}$$

where I_{str} is the streaming current, v_{jet} is the streaming velocity of the jet, and d_{jet} is the jet diameter. The electrically isolated nature of the liquid microjet setup can make the influence of the surface potential especially high for experiments with nonconducting samples. By increasing the sample conductivity, this effect can be compensated.

4 Experimental setup and procedure

This chapter presents in detail the experimental setup and procedure used for the data acquisition. The realization of the methods and techniques described in the previous Chapter 3 will be demonstrated. The chapter consists of an overview of the optical pump-probe setup with its main components: Ti:Sapphire laser system, OPA, table-top HHG setup, liquid microjet, and time-of-flight photoelectron spectrometer. A substantial part of this chapter is designated for the characterization of the pump and probe beams in the spatial, spectral and time domain. The measurements of the cross-correlation function of the pump and probe pulses are demonstrated with the use of the gas and liquid samples, where the electron emission energy sidebands originating from LAPE were used for generation of the time-dependent cross-correlation signal. As a final point of this chapter, the experimental procedure is presented stepwise with explanatory comments.

4.1 The optical pump-probe setup

4.1.1 Overview of the optical pump-probe setup

The XUV photoemission spectroscopy measurements were performed with an aqueous solution of $[Fe(bpy)_3]^{2+}$ with the use of the pump-probe technique. A schematic overview of the optical pump-probe setup is presented in the Figure 21. The Ti:sapphire laser system delivers linearly polarized pulses of 800 nm central wavelength, 5 kHz repetition rate, 2.4 mJ pulse energy, and 25 fs duration. The laser output was split into two beams so that a pulse energy of 1.4 mJ was available to pump the HHG process and an energy of 1 mJ per pulse was used to pump an optical parametric amplifier (OPA). The pump power for HHG could be tuned by using a half-wave plate in combination with a thin-film polarizer. A pair of BK7 wedges mounted on two parallel translation stages was introduced into the HHG pump beam for independent optimization of the pulse duration.

A motorized optical delay stage was used in the pump beam path to vary the time delay between the pump and the probe pulses. Since the XUV pulse requires vacuum conditions for its propagation to the interaction region, the HHG setup is connected to the experimental chamber with a vacuum pipe. Fused silica laser windows of UV grade with antireflective coatings were used for transmission of the 800 nm pump beam into the HHG vacuum chamber, where XUV light was generated, and for transmission of the 530 nm beam to the experimental chamber. A rectangular aluminum-coated mirror was positioned in vacuum on an adjustable mirror mount close to the path of the XUV beam. This mirror was used to overlap the optical-pump and the XUV-probe beams on the sample surface with a small angle of ~1° between the beams.

The laser pump beam was focused into the interaction region with the use of a lens of 400 mm focal length. The lens was mounted on a 3-dimensional mechanical translation stage outside the vacuum chamber. Thus, the laser focus position in the experimental chamber could be precisely adjusted with three micrometer screws in the two transversal and the longitudinal directions with respect to the beam propagation axis. Movement of the lens along the laser beam allows the spot size of the pump beam to be adjusted in the interaction region. Since the laser intensity has a square dependency on the beam size, the lens translation provides the possibility to adjust the pump intensity. In contrast to handling the optical pump beam, the spot size of 75 μm (FWHM) of the XUV beam was

fixed and could not be easily adjusted during the experiment due to the constructional features of the HHG setup. A nearly twice larger spot size of 155 μm (FWHM) of the optical beam was typically applied in order to simplify the overlap between the pump and probe spots and to decrease the possibility of distortions arising from the laser pointing instability. To achieve this condition, the focus position of the 530 nm beam was adjusted at a few tens of mm behind the sample. The measurements of the focus spot size of both optical and XUV beams were performed with the use of the razor-blade method described below in 4.4.1.

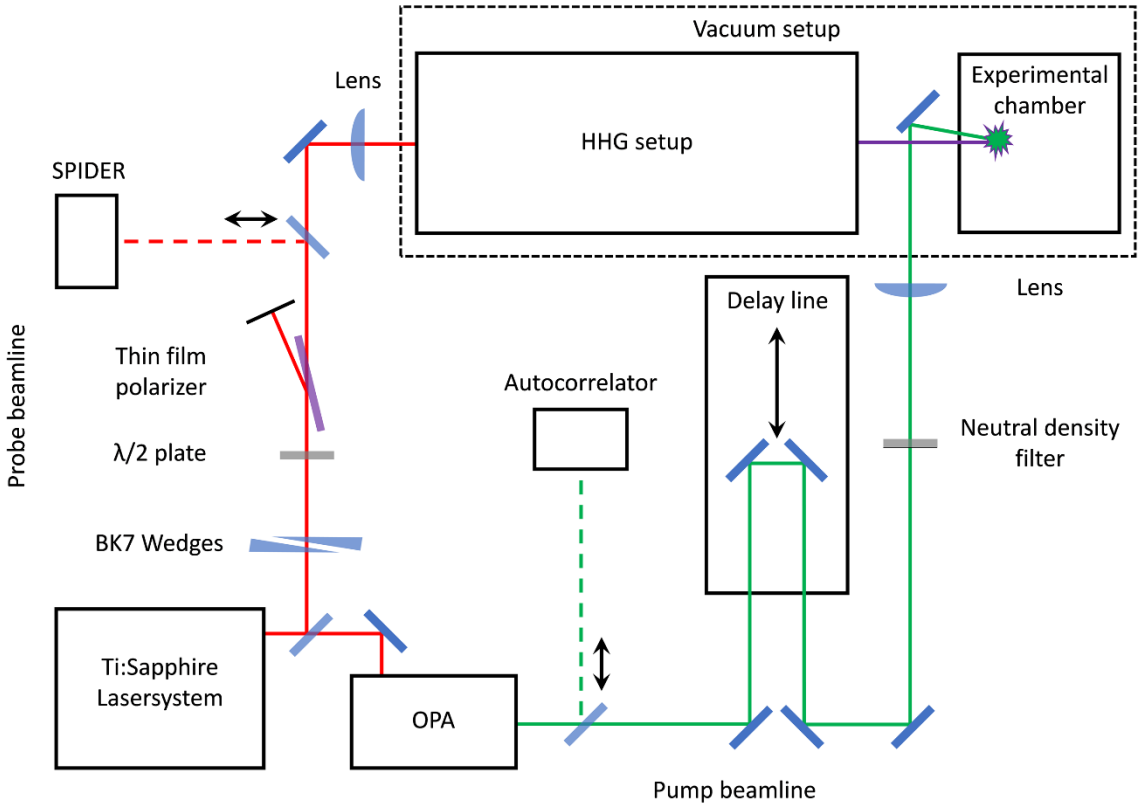

Figure 21. Simplified scheme of the optical pump-probe setup. The red line denotes the path of the 800 nm laser beam, the green line denotes the path of the 530 nm pump laser beam, and the blue line denotes the XUV probe beam.

The polarization of both the OPA pump and XUV probe beams was kept horizontal in the experimental chamber. The pump beam was attenuated by using a metal-coated neutral density filter to obtain an energy flux of 88 W/cm² in the interaction region.

Detailed descriptions of the optical setup, the laser system, the OPA, and the HHG setup, will be presented separately in the following sections.

4.1.2 Laser system

Since the first report on the development of a Titanium-Sapphire (Ti:Sa) laser at the 12th International Quantum Electronics Conference in Munich 1982 [164, 165], this laser technology was continuously improved. Nowadays advanced Ti:Sa laser systems are available, which deliver laser pulses of high intensity and short pulse duration of the order of 10 fs. The properties of these lasers make them a suitable light source for ultrafast time-resolved experiments and for the generation of XUV, UV, visible, and IR ultrashort pulses via frequency conversion in non-linear media. In the experiments presented in this work, a commercial Ti:Sa laser system from Coherent Inc. (Legend Elite Duo) company was used. The laser system consists of two main parts: the oscillator and the amplifier. The oscillator delivers the seed pulse for the amplifier. In this particular laser system, the oscillator named "Vitara" implements the Kerr-lens mode-locking technique. The first oscillator based on this technique was reported in 1991 [166], and initiated a breakthrough in the femtosecond laser technology. The "Vitara" oscillator delivers 775 nm sub-25 fs seed pulses with 80 MHz repetition rate. The chirped pulse amplification technique is employed in the laser amplifier system. First, the seed pulse is stretched with the use of a two-grating stretcher. The stretched pulse is amplified in two stages: first in the Ti:Sa regenerative amplifier and then in the single pass Ti:Sa amplifier. The second harmonic output of 527 nm wavelength of the diode-pumped Nd:YLF laser "Evolution" with an output power of 75 W delivers the energy for both stages of the amplification process. Finally, the amplified 800 nm pulse of 2.4 mJ energy is compressed close to the transform-limited duration of ~25 fs in a two-grating compressor. The compressor can also be tuned to create a positive or negative chirp in the output pulse by varying the grating separation.

4.1.3 Optical parametric amplifier

In the experiments presented here, a commercial OPA from the Light Conversion Ltd. was used to generate ultrashort laser pulses at the wavelengths of 300 nm, 350 nm, and 530 nm, respectively. The wavelength range of OPA is tunable between 240 and 2600 nm. The OPA consists of two amplification stages for the generation of ultrashort signal and idler pulses in the NIR spectral range. Additionally, there are stages for generation of the second harmonic of the signal or idler beam or, alternatively, for the sum frequency

generation (SFG) via mixing of the signal or idler beam with a fraction of the fundamental beam. The fundamental beam is split by beam splitters in four parts, for the seed generation, two amplification stages and for the SFG stage. In the first amplification stage (pre-amplification stage), white light generation was used as a seed. The white light was generated in a sapphire plate by focusing a small amount of the 800 nm light split from the pump beam. A spectral fraction of the generated white light, tuned in the wavelength range between 1100 and 1600 nm, is used for the parametric amplification process. The white light and the pump beam overlap with each other in a non-linear BBO crystal at a small angle, so that the non-collinear residual pump beam can be spatially separated from the generated signal beam, which propagates in the same direction as the white-light seed. The advantage of using the white light as a seed is due to the fact that it contains already a full range of wavelengths available for amplification, so that the required signal wavelength can be chosen straightforwardly just by changing the BBO crystal orientation and by controlling the time overlap between the chirped white-light pulse and the 800 nm pump pulse. The spatial overlap between the pump and seed beams, once optimized, remains constant and does not need to be readjusted.

The signal pulse in the wavelength range between 1100 nm and 1600 nm from the first amplification stage is used as an intense seed for the second amplification stage in the OPA. This allows a high conversion efficiency to be achieved. In the second OPA stage, the seed and the fundamental beams propagate collinearly through the second BBO crystal. The collinear overlap is accomplished with the use of a dichroic mirror. The separation of the signal, idler and residual pump beams after the second amplification stage is also accomplished with the use of dichroic mirrors.

Generation of either 300 nm or 350 nm pulses was implemented in two successive SHG processes. In the former case, the second harmonic of 600 nm wavelength was first generated in a BBO crystal from the 1200 nm signal beam and was subsequently frequency-doubled in a second stage to produce the 300 nm pulses. The 350 nm pulses were generated analogously to 300 nm. The generation of the 530 nm pulses was accomplished via the sum frequency generation between the signal beam of 1570 nm wavelength and the 800 nm fundamental beam, which are mixed in a BBO crystal. The time overlap with the pump pulses is controlled in all stages by employing motorized translation stages in the corresponding delay lines for the pump beam.

4.1.4 Third harmonic generation setup

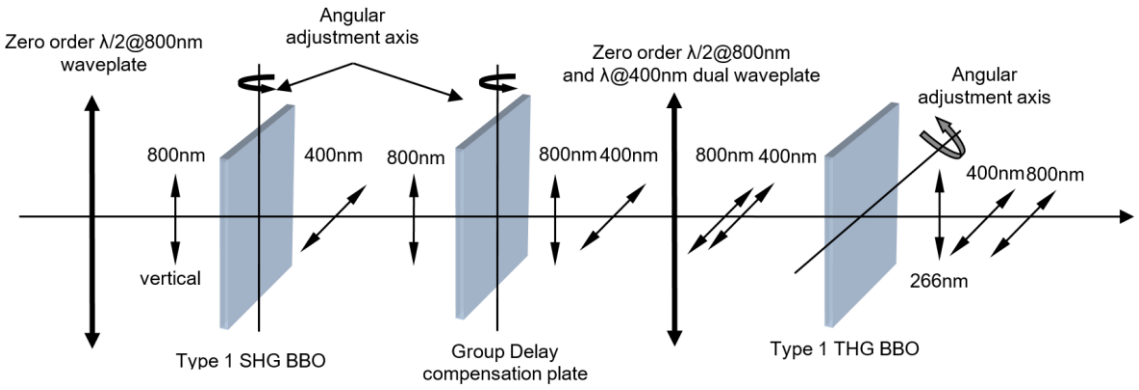

Figure 22. Schematic depiction of the principle of the in-line THG. The picture is reprinted with permission from www.eksmaoptics.com.

The generation of the third harmonic is accomplished via two sequential non-linear processes induced in two BBO crystals with the use of the fundamental (800 nm) pump beam of ca. 4 W average power (corresponding to 0.8 mJ pulse energy). The principle of the in-line THG is presented in Figure 22. In the first step, the second harmonic of 400 nm is generated in a BBO crystal which provides the phase matching of type I and yields the conversion efficiency of ca. 15 %. The intense residual fundamental beam is used in the second crystal for SFG with the 400 nm beam. Both beams are propagating collinearly after the first crystal and the correction of the spatial overlap is not necessary. However, the 800 nm and 400 nm pulses after the SHG in the first stage are separated in time, which is a consequence of the group velocity mismatch in the BBO crystal. Since 400 nm and 800 nm beam polarizations are orthogonal, a birefringent medium can be used to compensate the group delay difference and achieve a perfect time overlap in the second BBO crystal. In the present setup, a calcite plate was used for this purpose. A dual wavelength wave plate was used to rotate the polarization of the fundamental beam by 90° after passing the calcite plate, so that both 400 nm and 800 nm beams have the same polarization axis. This is necessary for the type I phase matching of the SFG process. The third harmonic of the fundamental beam with the wavelength of 266 nm is generated in this process and has a polarization perpendicular to the fundamental beam. A couple of the dichroic mirrors are used to separate the third harmonic from the residual laser light. Such an accomplishment of the THG setup, as compared to the classical setup with the use of a translation stage for achieving of the time overlap in the second crystal, is more simple and economical and it yields comparable conversion efficiency.

4.1.5 High-order harmonic generation setup

The HHG setup represents a tabletop system of vacuum chambers with the XUV optical components placed in vacuum. The vacuum conditions are required for the propagation of XUV light. The main components of the HHG setup implemented in this work are shown in Figure 23. A lens of 600 mm focal length was used to focus the 800 nm laser beam into a gas cell of 16 mm length, where the HHG process was induced. The lens was mounted on the mechanical translation stage, which allows optimization of the focus position in the cell. An aluminum foil was wrapped around the gas cell, so that the pump laser burns the smallest possible input and output apertures by itself. In the experiment, the HHG pump energy was set to 1 mJ per pulse.

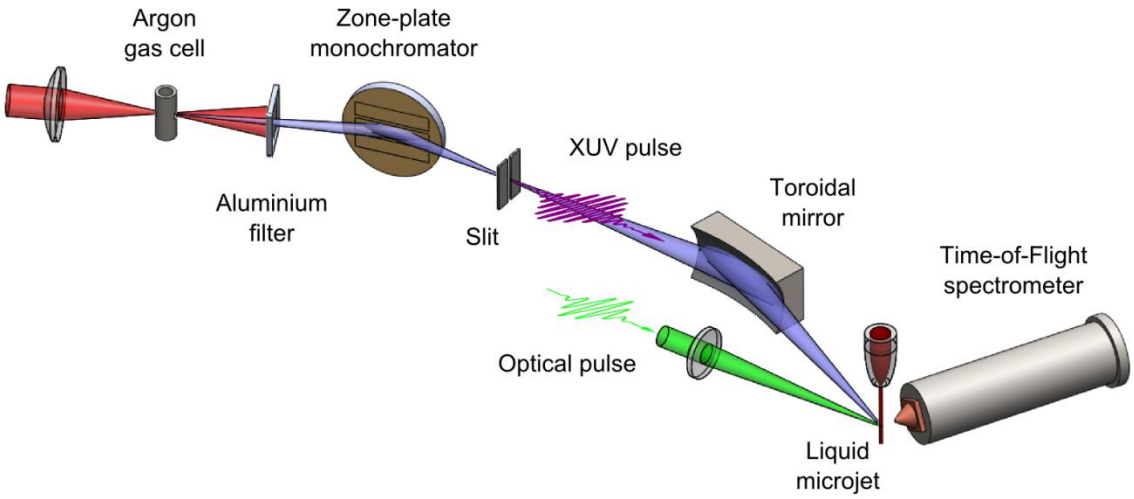

Figure 23. Experimental setup including generation and monochromatization of the XUV probe beam and its delivery optics, laser pump beam, time-of-flight electron spectrometer, and liquid micro-jet.

The gas cell was filled with Argon gas to a ~25 mbar pressure. The argon pressure was adjusted with the use of a dosing valve to the value yielding the maximal XUV photon flux. The photon flux was monitored during the adjustment procedure with the movable photodiode (not shown in the Figure 23) placed behind the slit of the monochromator. The residual pump laser beam was filtered out from the XUV beam with the use of a 150 nm thin aluminum foil.

The peculiar feature of the present setup is the application of the off-axis reflection zone-plate for monochromatization of the ultrashort XUV pulses. The basic principles of the reflection zone plate are presented in Ref. [167]. This type of monochromator facilitates simultaneously the spatial separation (dispersion) of the generated harmonics

and their focus. Thus, the selected harmonic passes a narrow slit positioned at the focal point of the zone plate whereas the other harmonics are blocked by the slit shutters. In contrast to the most common type of monochromators based on the implementation of gratings, the zone plate demonstrates high transmission efficiency combined with relatively low temporal distortions of the monochromatized XUV pulses. The zone plate used in the present HHG setup consists of three gold-coated zone structures created on a single silicone substrate. The structures are designed to select the 17^{th}, 21^{st}, and 25^{th} harmonic of the 800 nm laser beam, respectively. Focusing of the selected harmonic into the interaction region of the experimental setup is accomplished by using a toroidal mirror.

In the experiments presented in this work, the zone plate was applied to select the 21^{st} harmonic with a photon energy of 32.55 eV. The duration of the transmitted XUV pulses was measured to be 45 fs, and the transmission efficiency of the zone-plate monochromator was calculated to be approximately 28% for the 21^{st} harmonic. A detailed description of the HHG setup was presented in Ref. [168].

4.2 Time-of-Flight spectrometer

A commercial TOF spectrometer provided by SPECS GmbH (see Figure 24) was used for the data acquisition. This type of electron spectrometer is suited for experiments with pulsed light sources. The spectrometer employs a multi-element, two-stage (electrostatic) transfer lens for effective collection and transfer of the photoelectrons to the detector. The transfer lens resembles the lenses which are typically used in hemispherical analyses. For the amplification and detection of the photoelectron signal, the spectrometer employs a 3D delayline detector (DLD), which consists of a Chevron multichannel plate array and an in-vacuum readout unit. The readout unit is sensitive to the arrival position of the electron in the detector plane. It consists of two crossed coils, which form together a grid-like structure. Each of the coils enables to record the electron arrival coordinate for one of the two dimensions of the detector surface. The readout unit is connected to external electronic unit for the fast data acquisition. The DLD allows to perform measurements with the count rate up to 5 kHz, limited by the repetition rate of the laser system. Thus, the DLD can directly measure both the arrival time and the position of the electrons on the detector, which can be transformed with the use of a conversion routine to the kinetic energy and angular distributions of photoelectrons.

However, the angular distribution of photoelectrons was not the focus of this work and only their kinetic energy spectra will be considered in the data analysis presented below. The count rate of 5000 events per second corresponds to detection of one electron per XUV pulse. This measure prevented the detector from overloading. Such a count-rate condition could be achieved via selectively reducing the photoelectron signal by applying a retardation voltage on a grid placed in front of the DLD unit.

The spectrometer can be operated in several modes, characterized by different acceptance angles and energy resolutions. Switching between modes and setting of the modes parameters can be performed online by using the software provided with the spectrometer. For the experiments presented in this work, two modes were chosen for the most efficient way of data acquisition.

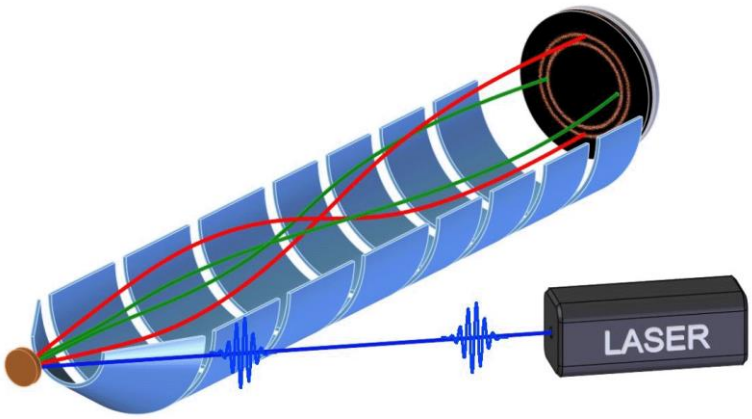

Figure 24. Simplified representation of the time-of-flight spectrometer Themis 600 provided by SPECS, which employs the electrostatic-lens technique. Red and green lines represent the trajectories of electrons with different kinetic energies. The picture is reprinted with permission from www.specs.com.

In the steady-state measurements, the spectrometer was operated in the drift mode, corresponding to the classical field-free design with an electron acceptance angle of ±1°. In this mode the kinetic energy scale is not limited, which allows to record spectra in a wide kinetic energy range involving XUV ionization contributions from both $[Fe(bpy)_3]^{2+}$ and water. For time-resolved measurements, the wide-angle mode (WAM) was applied. In this mode the spectrometer employs a predefined non-uniform electrostatic field, which allows increasing of the electron acceptance angle to ±15° in a given limited spectral range. The larger acceptance angle reduces the acquisition time while achieving a high signal-to-noise ratio. This is a crucial issue for the experiments with liquid samples,

where the data acquisition needs to be fast because of instabilities in the experimental conditions. In the time-resolved measurements, XUV spectra were recorded in a spectral range of 9 eV width, centered at the energy peak originating from ionization of the 3d(t_{2g}) orbitals of $[Fe(bpy)_3]^{2+}$.

4.3 Liquid micro-jet setup

The liquid micro-jet technique was applied to achieve high-vacuum conditions in the experimental chamber. A syringe pump was used to deliver the liquid sample to the interaction region through a quartz nozzle of 18 µm orifice with a constant flow rate of 0.4 ml/min. With this setup, a micro-jet of cylindrical shape was created with a laminar flow length of a few millimeters. The optical pump and the XUV probe beams intersected each other on the micro-jet surface in the region of the laminar flow in front of the skimmer of the time-of-flight (TOF) electron spectrometer. The micro-jet was oriented perpendicular to the XUV beam and to the TOF spectrometer axis. The pump and probe beams were merged in the interaction region at a small angle of ~1°. The spectrometer was equipped with a conical skimmer of 400 µm aperture. A small distance of approximately 0.5 mm between the micro-jet and the skimmer was applied to minimize scattering of photoelectrons by the residual gas molecules.

Refilling of the syringe pump and switching between different samples without disturbing the vacuum conditions was accomplished with the use of an additional HPLC pump. The HPLC pump delivers Milli-Q water to the liquid micro-jet system and could be applied anytime during the measurement in order to temporarily replace the syringe pump.

The sample solution, which was introduced into the interaction chamber during the experiment, was collected in a cryogenic trap filled with liquid nitrogen. The geometry of the cryogenic trap was designed and afterwards improved according to experiences gained during the test phase of the setup. The main parts of the trap are: a double-walled stainless steel collector, a vacuum adapter flange, and an aluminum cylinder serving as the liquid catcher. The trap is placed directly under the liquid jet, so that the liquid beam passes through the center of the cylindrical catcher into the collector reservoir. Thus, the catcher is positioned in the experimental chamber, whereas the collector reservoir is attached to the setup outside this chamber, and the adapter flange between these two parts is used to handle them separately and to simplify the cleaning procedure of the reservoir.

The liquid nitrogen flows from the dewar through a hose connected to the threaded inlet in the upper part of the trap and fills the space between the walls of the collector. A pipe with an open end is provided for the protection of the reservoir against overpressure. Additionally, a PEEK disk was introduced between the aluminum catcher and the flange as a thermal isolation layer to prevent the overcooling caused by liquid nitrogen, which could lead to the formation of a frozen sample near the interaction region and, eventually, to blocking of the catcher aperture. The high mechanical vibration stability of the experimental setup gave rise to the possibility of building of sample icicles, which could grow from the bottom of the collector up to the level of the interaction region. This would lead to blocking of the liquid jet by the icicles. To prevent the growth of long icicles, a cutter blade, rotatable from outside, was introduced into the collector reservoir with the use of a vacuum flange that had a rotation feedthrough. The cutter could break icicles without interrupting the experiment.

A second cryogenic trap was introduced into the experimental chamber to collect the evaporated liquid sample on its surface. The stainless steel surface of this cold-trap was cooled to cryogenic temperatures by filling its reservoir with liquid nitrogen through the opening in the upper part of the trap. Thus, the second trap was serving as an additional vacuum pump. Its pumping efficiency contributed significantly to the pumping speed (1500 l/s) of the turbo-molecular pump used to pump the experimental chamber. During the operation of the liquid micro-jet setup, the two cryogenic traps described above allowed a residual gas pressure of $<2\times10^{-5}$ mbar to be maintained in the interaction region. At the beginning of a measurement session, the cooled setup could hold stable vacuum conditions up to one hour without refilling the traps with liquid nitrogen.

4.4 Pump and probe pulse characterization

4.4.1 Characteristics of the pump beam

Figure 25 represents the spectrum of the 530 nm beam generated in the OPA which was used for excitation of the MLCT states of $[Fe(bpy)_3]^{2+}$. The spectrum was recorded with the use of a commercial compact fiber spectrometer from Ocean Optics Inc. (HR2000+) in order to monitor the spectral properties of the laser pump beam. One can see that the central wavelength of the spectral peak of the pump pulse lies precisely at 530 nm. The fit of the peak profile to a Gaussian function yields the spectral width of 10 nm. This value corresponds to the transform limited pulse duration of 41 fs, assuming that the pulse has a Gaussian shape in the time domain.

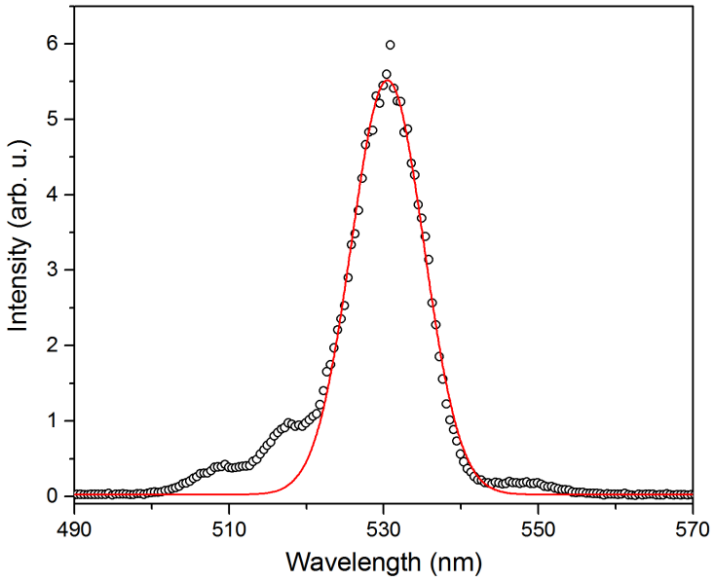

Figure 25. The spectrum of the pump laser beam generated in the OPA. The red curve depicts the Gaussian fit to the spectral peak, lying at the wavelength of 530 nm and exhibiting a spectral width of 10 nm (FWHM).

The focal spot size of the optical beam was measured by scanning a razor blade across the beam and recording the light intensity behind the blade with a photodiode. The razor blade was mounted on a mechanical manipulator in the experimental chamber and was scanned in front of the skimmer of the spectrometer in the interaction region. The dependency of the light intensity on the blade position, recorded by applying this method, has a sigmoid shape. Assuming a Gaussian distribution of laser intensity in the focus, the data can be fitted to an error function, erf(x), where x represents the coordinate of the

razor blade across the focus. The results of such a measurement are presented in Figure 26. For better accuracy, the razor blade scans were repeated several times with the result of (155 ± 5) μm for the focus spot size (FWHM, full width at half maximum) of the 530 nm laser beam.

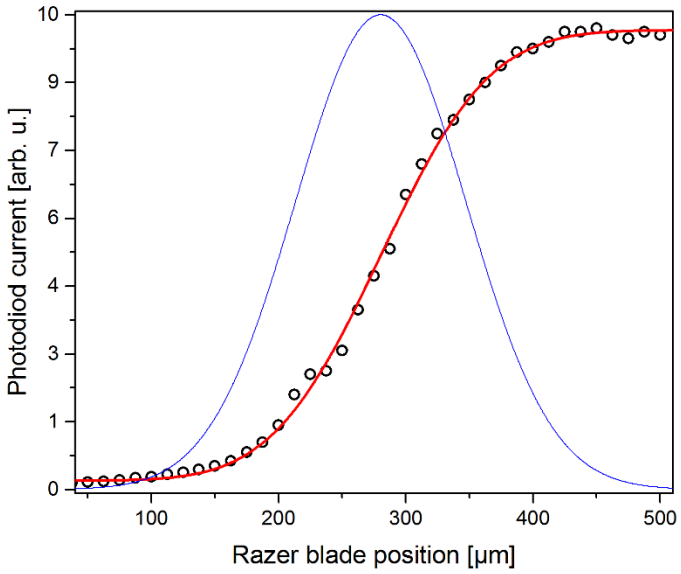

Figure 26. Results of the measurement of the spot size of the 530 nm beam with the use of the razor blade method. The red curve depicts a fit of the dependency of the photodiode current, recorded as a function of the razor blade position, to the error function. The blue curve represents the radial intensity distribution in the laser focus calculated for a Gaussian beam with the width of 155 μm (FWHM) as obtained from the fit.

4.4.2 Spectral characteristics of XUV pulse

The spectral characteristics of the XUV beam were inferred from steady-state photoelectron spectra of Argon. The central XUV photon energy and the bandwidth were obtained from a fit of the Argon spectra to a sum of two Gaussian profiles, associated with the formation of two spin-orbit states of the formed Ar^+ ion. A bandwidth of ~150 meV was obtained by Dr. Jan Metje from the measurement when operating the spectrometer in drift mode [169]. In the wide angle mode, this number increases to ~350 meV as a result of the manipulation of the electron trajectories induced by the electrostatic lens system of the analyzer. This value defines the spectral resolution in the time-resolved experiments presented in this work. Figure 27 demonstrates the photoemission spectrum from the 3p orbitals of Argon recorded in wide angle mode. The fit results are presented by the red curve in the figure. The broadening of the signal in this mode prevents contributions from the two spin-orbit states from being easily distinguished. Therefore,

In the fit routine the difference in the spectral positions of the two Gaussian profiles, representing the spin-orbit splitting, was fixed to the literature value of 0.18 eV [170]. The ratio between the two spin-orbit state contributions was set to 1:2 according to the statistical weights of these states, defined by the degeneracy of states with different magnetic quantum numbers. The FWHM of the full peak, representing the sum of two Gaussian profiles, was found to be typically 0.4 eV. This value was used as a reference for daily monitoring of the bandwidth of the XUV radiation.

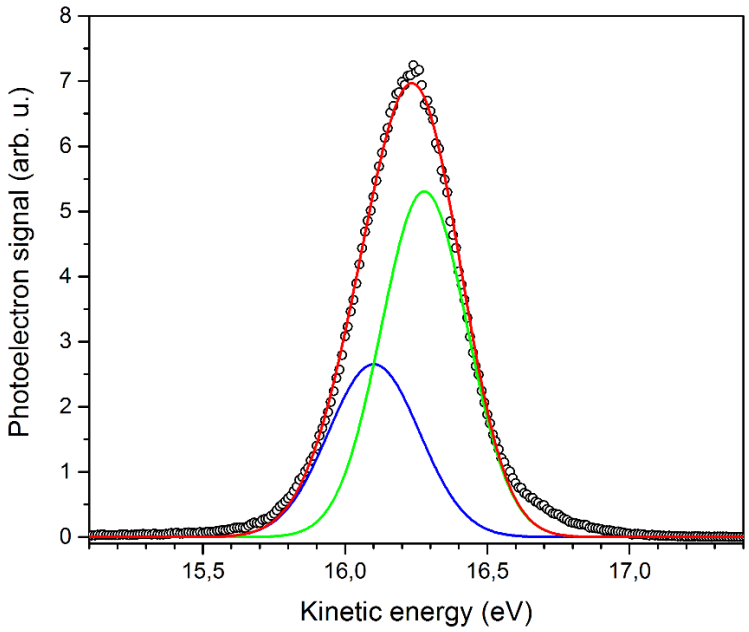

Figure 27. Kinetic energy spectrum generated by ionization of Argon with the 21st harmonic and recorded with the electron spectrometer operating in wide angle mode. The red curve depicts a fit to a sum of two Gaussian profiles originating from the spin-orbit splitting of the ground 3p state of the Ar^+ ion. The individual contributions for the two spin-orbit states are shown by the blue and green curves, respectively.

Besides the bandwidth of the XUV light, the measurement of the argon spectrum also allows the relative contribution of the neighboring harmonics to the ionization signal to be estimated. This is an important issue because the signal produced due to ionization of water by the 23rd neighboring harmonic in the experiment can interfere with the signal from the Fe 3d orbitals produced by the 21st harmonic. The low concentration of $[Fe(bpy)_3]^{2+}$ in the aqueous solution leads to a much higher photoelectron yield from water in comparison to the signal from the solute. This issue can make the influence of the higher neighboring harmonic perceptible in the spectra. Therefore, it is of particular importance to ascertain that the contribution of higher-order harmonics to the ionization signal is sufficiently small. The steady-state measurements of the XUV emission from

the Ar gas have demonstrated that the higher neighboring harmonics were discriminated in the monochromator below 0.07% (see Figure 28). As it will be shown in the Chapter 5, this discrimination value is one order of magnitude lower than the ratio between ionization yields from the $1b_1$ water and the iron-centered orbitals, which implies that the ionization contribution of the higher harmonic to the photoemission spectrum is sufficiently small that it can be neglected.

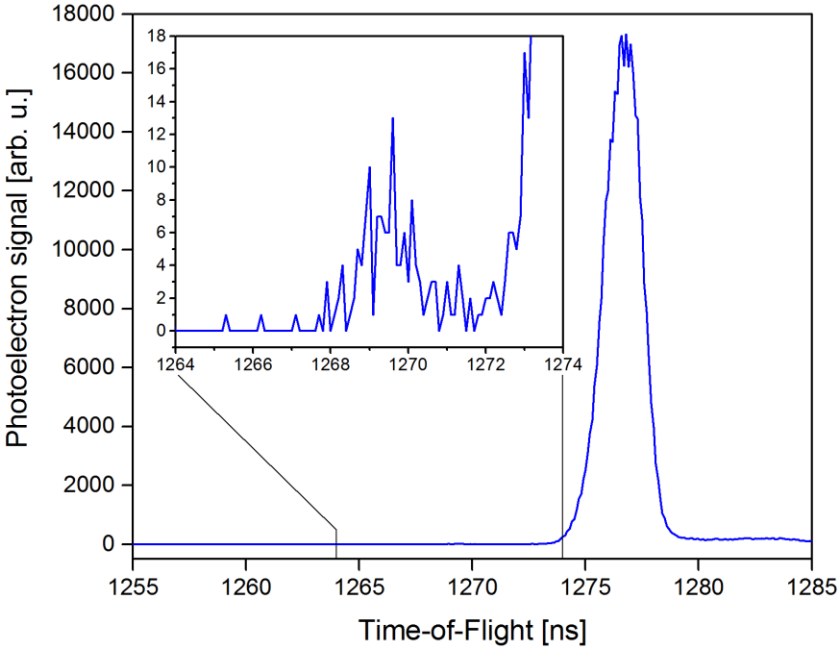

Figure 28. Time-of-flight spectrum generated by ionization of Argon with the 21st harmonic and recorded with the spectrometer operating in the wide angle mode. The slit size of the monochromator was 100 µm. The inset shows the zoomed contribution of the 23th harmonic.

4.4.3 Cross-correlation in gas and liquid

The cross-correlation measurements performed with the gas (argon) and liquid (aqueous solutions) samples were used as a reference for the optimization of the temporal properties of the laser and XUV pulses. The temporal overlap between the pump and probe pulses and the experimental time resolution were determined from the cross-correlation measurements carried out on the liquid jet during the experiment. As described in detail in Section 3.2.7, the cross-correlation signal arises from laser-assisted photoelectric effect (LAPE), induced by XUV light, and was previously reported in the studies on gas [152], solid-state [154], and liquid [171] samples. LAPE leads to the appearance of sidebands in the XUV photoelectron spectrum, shifted on the kinetic

energy scale by the optical photon energy. The photoemission yield integrated over the region of the sidebands and recorded as a function of the time delay delivers a cross-correlation function between the optical and XUV pulses.

The large number of optical elements used in both the pump and probe beam paths unambiguously requires optimization of the temporal characteristics of the visible and XUV pulses. This problem is well known in the optical setups for generation of the ultrashort laser pulses and was previously discussed in Refs. [172-175]. There were two options considered for optimization: (1) adjustment of the compressor of the laser system and (2) introducing of additional optical elements in the beam paths, such as dispersive media or chirped mirrors. Because of the use of dispersive optics in both 800 nm beam paths, which caused a positive chirp of the laser pulse, a negative group velocity dispersion (GVD) was applied in the pulse compressor of the laser system. The difference in the GVD between the HHG and OPA beam lines was compensated by using of a pair of BK7 wedges in the HHG line. The chirp of the 800 nm pulses was optimized to achieve the shortest 530 nm pulse, which was controlled by an autocorrelator in the pump beam path, and to maximize the HHG output monitored by a photodiode behind the zone-plate monochromator. Additionally, the pulse duration and GVD of the 800 nm pulse was controlled by SPIDER in the probe beam path before the entrance to the vacuum chamber of the HHG setup.

Figure 29 demonstrates the experimental results of the cross-correlation measurement with the use of argon gas in the beginning of the chirp optimization procedure (a, d) and in the end of it (b, e). One can see that as a result of chirp optimization, the cross-correlation, which defines the time resolution in the experiment, was reduced by a factor of 1.5 and it acquired a symmetric shape. The latter point is of particularly high importance for the time-resolved experiments presented in this work, since the asymmetric signal arising from LAPE could be difficult to distinguish from the transient signal arising from XUV ionization of the short-lived states excited by the pump pulse. Since the cross-correlation measurement with gas required higher intensity of the pump beam than with liquid samples, in experiments with argon the neutral density filter was removed from the beam path and the laser focus was shifted to the position in front of the orifice of the spectrometer skimmer. This yielded sufficient pump intensity to generate a prominent signal from the first side band, which was used in the measurements.

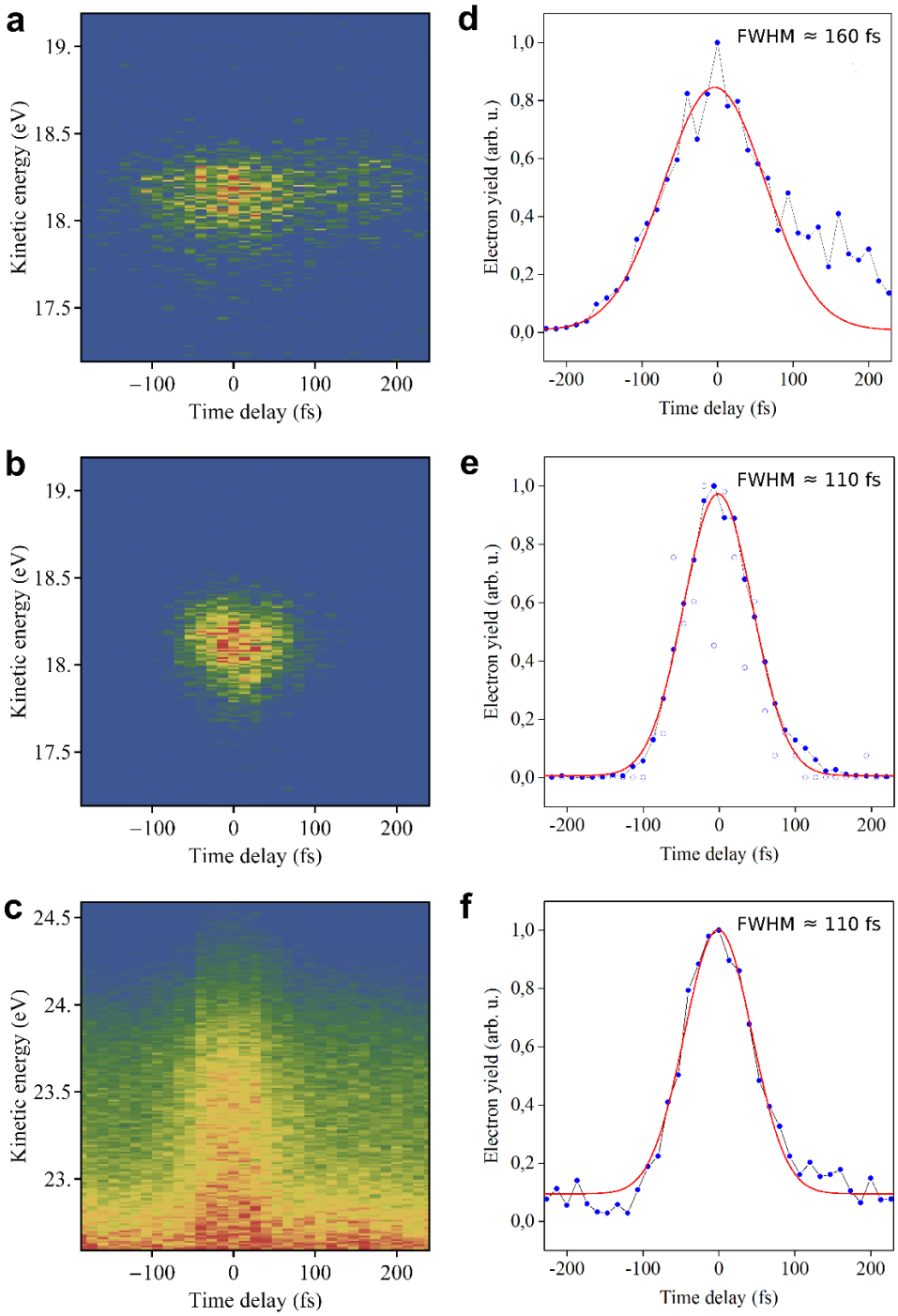

Figure 29. Panels (a), (b), and (c) show the measured signal which contains a cross-correlation contribution from the first side band. The measurements were performed with argon before optimization of the pulse duration (a), with argon after optimization of the pulse duration (b), and with aqueous solution of $[Fe(bpy)_3]^{2+}$ (c), respectively. Panels (d), (e), and (f) represent integrated electron yield from the first side band shown in panels (a), (b), and (c), respectively, as a function of the time delay. The experimental data are shown by connected blue points, whereas the red curves represent the Gaussian fits to the respective data set. The empty circles in (e) denote the integrated electron yield from the second side band (lying beyond the energy range in the panel (b)), occurring in the cross-correlation measurement performed with argon after the optimization of the pulse duration.

The signal from the second side band was also observed, but was rather weak and noisy. However, the fit of the cross-correlation function for the second side band gave approximately the same (slightly smaller) cross-correlation width as for the first side band. The cross-correlation results for the both side bands are compared in the Figure 29(e). Further, the measurements were repeated with the use of an aqueous solution containing 5 mM of NaCl and 50 mM of $[Fe(bpy)_3]^{2+}$. The results of the cross-correlation measurements with the use of the liquid samples (see Figure 29(c,f)) revealed approximately identical value for the cross-correlation width as in the case of argon.

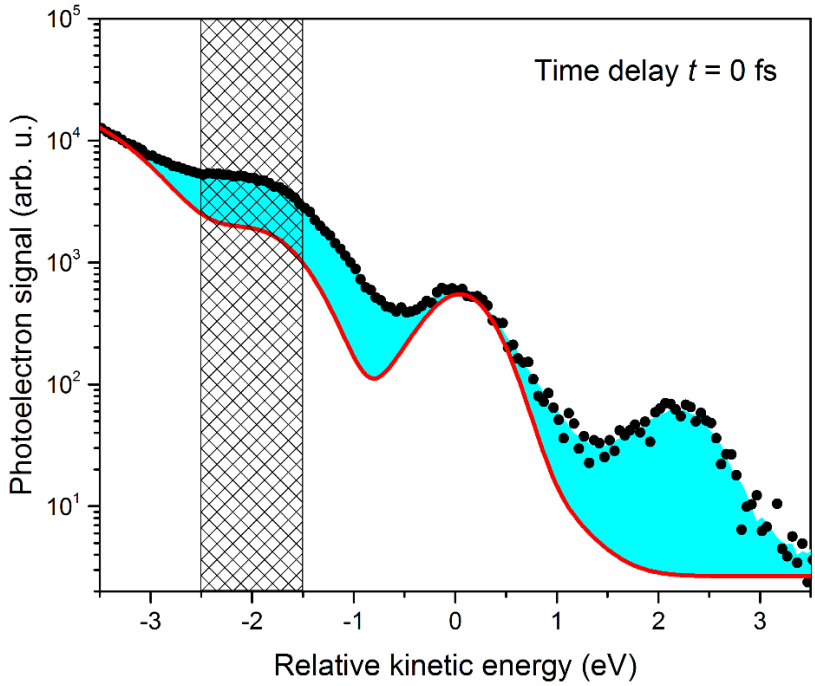

Figure 30. Kinetic energy spectrum of photoelectrons recorded for 50 mM $[Fe(bpy)_3]^{2+}$ (aq) solution in the wide angle mode at the zero time delay between pump and probe pulses. The energy scale is given relative to the emission peak from the Fe 3d(t_{2g}) orbitals of $[Fe(bpy)_3]^{2+}$. The red curve depicts a fit to a kinetic energy spectrum recorded with the use of XUV beam only (presented in detail in Chapter 5). The cross-hatched area represents the integration range on the energy scale, used to define the cross-correlation signal between the laser and XUV pulses. The increase of the emission signal in this range, as compared to un-pumped sample, results from the LAPE of water.

Thus, all further routines of the chirp optimization and of the determination of the zero time delay position and temporal resolution of the experiment were performed with the use of the aqueous $[Fe(bpy)_3]^{2+}$ sample. For the aqueous solution, the signal integration range was chosen between the kinetic energies of 23 and 24 eV (see Figure 29(c)), corresponding to the range between -1.5 eV and 2.5 eV on the relative energy scale with respect to the emission peak from the Fe 3d(t_{2g}) orbitals (see Figure 30). In this

energy range, the first laser-assisted sideband of XUV ionization of water is most pronounced in the spectrum. The cross-correlation signal recorded in each time-resolved measurement was used to account in the data processing for the drift of the zero time delay.

After optimization of the laser compressor, the cross-correlation width was varying between 50 and 60 fs during the experiment. An exemplary cross-correlation trace is plotted in Figure 31. Maximization of the cross-correlation signal was implemented for fine adjustment of the spatial overlap between the laser and XUV beams on the microjet.

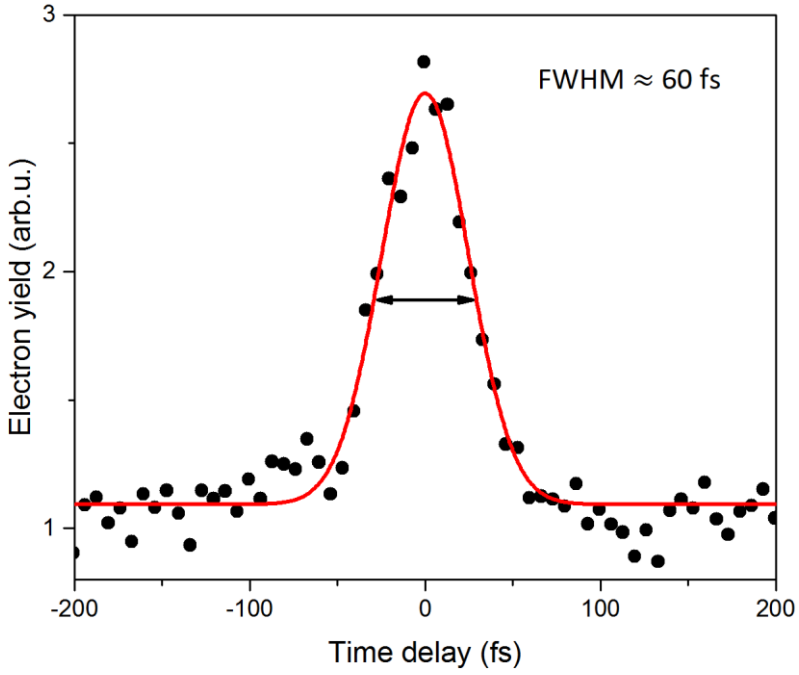

Figure 31. Integrated electron yield of 50 mM $[Fe(bpy)_3]^{2+}$ (aq) plotted as a function of the time delay between 530 nm pump and XUV probe pulses. The red curve represents a Gaussian fit of the recorded data, which represents the cross-correlation between the pump and the probe pulses arising from LAPE of liquid water.

4.5 Experimental procedure

The time-resolved measurements were performed by following a certain routine based on the experience collected in the earlier experiments. According to this routine, the daily procedure can by divided into the following steps:

- Preparation of the sample solution
- Adjustment of the HHG beam line

- Adjustment of the laser beam line
- Adjustment of the laser compressor
- Recording of the Ar 3p spectrum
- Installation of the cryogenic trap and liquid microjet
- Adjustment of the laser spot position at the sample
- Cross-correlation measurement on water
- Cross-correlation measurement on the sample solution
- Fine adjustment of the laser spot position
- Acquisition of the time-resolved data
- Cleaning of the experimental chamber and liquid microjet system

Preparation of the sample solution. The experiments were performed on 50 mM aqueous solution of $Fe(bpy)_3Cl_2$. Milli-Q water was used as a solvent. The concentration of 50 mM lies close to the solubility limit of $Fe(bpy)_3Cl_2$ in water, but the solution is still not saturated. It is important to avoid saturated solutions in liquid microjet experiments, since it leads to the building of solid growth on the tip of the nozzle around its orifice and can block the jet. Since $Fe(bpy)_3Cl_2$ dissociates in water to $[Fe(bpy)_3]^{2+}$ and two Cl^- ions and makes the solution conductive, the addition of salt to the sample is not necessary. Fresh sample was prepared at the beginning of each day of the beam time and filtered with the use of qualitative filter paper. This helped to filter out small particles which could block the jet during the experiment. To protect the light-sensitive solution from the illumination in the lab, the sample was prepared and stored in bottles made of light-protective glass and covered with aluminium foil. Additionally, 5 mM NaCl solution in Milli-Q water was prepared and filtered in the same way as the $Fe(bpy)_3Cl_2$ solution. Both solutions were handled and stored at room temperature.

Adjustment of the HHG beam line. The pathway of the 800 nm pump beam from the laser system to the vacuum window of the HHG chamber was defined using iris apertures. During the beam time, the position of the beam at the apertures was controlled in the beginning of the measurement day and realigned if necessary. After this procedure, the HHG setup was prepared for the measurement. The pressure of argon in the gas cell was adjusted to the maximal signal on the photodiode.

Adjustment of the laser beam line. The preparation of the laser line starts with the control of the OPA performance. The output power was monitored. If necessary, the OPA

was adjusted to achieve the maximum output power. The wavelength of the pump beam was controlled using a compact commercial fiber spectrometer. After this initial step, the beam path from the OPA to the experimental chamber was optimized with the use of iris apertures. The alignment of the beam to the fixed iris apertures enabled us to reproduce the beam path with a high precision.

Adjustment of the laser compressor. The optimal compression of the 800 nm pump pulse for HHG and OPA was achieved by adjusting the compressor of the Ti:Sa laser system, as it was described in 4.6.

Recording of the Ar 3p spectrum. A steady-state measurement was performed in Argon to monitor the spectral characteristics of the HHG beam during the beam time, as described in the Section 4.4.2. For this measurement the empty experimental chamber was pumped over night with the use of the turbo pump. The clean and dry chamber was filled with Argon gas to a pressure of ~10^{-3} mbar. The measurements were performed while operating TOF spectrometer in the wide angle mode. Apart from the determination of spectral properties of the XUV radiation, the photoionization measurements on Argon enabled us to precisely align the HHG beam in the interaction region. The photoelectrons created by photoionization produce a characteristic spatial distribution at the position-sensitive detector, appearing as a broad stripe pointing in the direction of the XUV beam propagation, which allows the vertical position of the beam with respect to the spectrometer aperture to be judged. This acquisition feature was used to optimize the vertical position of the XUV focus via moving of the refocusing mirror with the use of motors controlled by a PC software. The count rate of the photoionization signal measured at a certain gas pressure in the chamber served as an additional reference to monitor the HHG performance. Once the optimal position for the XUV beam was found, it remained fixed until the end of the experimental session.

Installation of the cryogenic trap and liquid microjet. After performing the test measurements on Argon, the setup was rearranged for operation with the liquid sample. The liquid microjet was examined first outside of the vacuum setup with the use of Milli-Q water. If the instabilities in the microjet performance were observed during this test run, the quartz nozzle was exchanged or cleaned in the ultrasonic bath. As the next step, the perfectly running liquid microjet and the cryogenic trap were introduced to the vacuum system. At this stage, the microjet setup was operated with NaCl solution in order to save the $[Fe(bpy)_3]^{2+}$ sample. The position of the microjet in the experimental chamber was optimized manually with the use of the mechanical 3D manipulator, while only the

XUV beam was admitted to the interaction region. The main criterion for the adjustment of the jet in the direction perpendicular to the probe XUV beam axis was the maximization of the count rate. For the optimal alignment along the XUV light propagation direction, a compromise was used between the maximal count rate and the centered image of the photoelectrons at the DLD. The distribution of the detected photoelectrons is monitored in real-time on the PC screen using the data acquisition software. The vertical alignment of the jet was made by eye so that the middle of the laminar flow region was centered with respect to the spectrometer skimmer orifice. During this alignment procedure, the spectrometer was operated in WAM with applied retardation voltage in order to keep the count-rate below 5000 Hz.

Adjustment of the laser spot position at the sample. For this step, the laser beam line was open and the XUV beam was blocked. The use of visible light as the pump beam provided a simple possibility for the rough alignment of the laser spot at the liquid jet using its reflection. The reflection of the 530 nm laser beam from the cylindrical surface of the laminar flow region of the microjet gave a rise to the appearance of a characteristic green line, which one could observe on the spectrometer skimmer (see Figure 32(a)) and on the window of the experimental chamber, using a partially transparent medium as a screen. This line was used as an indicator, showing that the laser beam hits the jet in the interaction region. The further alignment was performed by maximization of the emission signal produced by the slow photoelectrons originating from the MPI process. During this routine, the spectrometer was operated in the drift mode and the retardation voltage was reduced.

Cross-correlation measurement with NaCl solution. The alignment procedure described in the last two steps enabled us to perform a cross-correlation measurement. It consisted of a series of time-resolved measurements in the time delay range where the time overlap of the pump and probe pulses was expected. This range can be roughly determined by verifying the positions of the scattered photon peaks on the TOF scale. The peaks originated from the direct reflections of the laser and XUV light from the jet surface, which could be detected by the DLD. More precise determination of the zero time delay was achieved via observation of the space-charge effect. The delay range was scanned first with large delay steps, and after finding an approximate position of the time overlap the step size was decreased until the signature of the cross-correlation between pump and probe pulse was clearly identified. As was mentioned in the Section 4.4.3, the cross-correlation trace indicates the exact position on the delay stage corresponding to the

zero time delay and provides information about the convoluted pulse duration of the laser and XUV pulses. If the FWHM of the cross-correlation function is not satisfactory (too large), the optimization procedure described in the Section 4.4.3 is necessary before proceeding with the next step.

Cross-correlation measurement with the sample solution. Once the zero time delay and width of the cross-correlation function is known, the $[Fe(bpy)_3]^{2+}$ sample was introduced to the experimental chamber. The cross-correlation measurement was repeated with the sample solution.

Fine adjustment of the laser spot position. After the exact position of the zero time delay is found by means of the cross-correlation measurements, the overlap of the XUV and laser beams at the jet surface could be refined with high precision. The count rate is very sensitive to the beam overlap and rises noticeable due to the additional photoelectron yield induced by LAPE. The highest signal in this case corresponds to the optimal overlap of the pump and probe spots at the sample. The optimization of signal was performed with the delay stage set to the position of the zero time delay which has been already defined in the previous step. The retardation voltage was applied in the spectrometer to cut off the signal from the water bands and, thus, to observe only the signal arising due to LAPE involving emission from the water and Fe 3d(t_{2g}) orbitals. The laser beam was carefully adjusted by moving the lens on the 3D translation stage, while monitoring the count rate. After this optimization step, the setup was ready for data acquisition.

Acquisition of the time-resolved data. For the sub-picosecond measurements, data acquisition was broken in a sequence of multiple time-delay scans. Each scan was carried out with a delay increment of 13.3 fs. The acquisition time per delay position and the total scan time was kept as short as possible in order to maintain the uniform environmental conditions in the experimental chamber. Measurements in the nanosecond range were performed with the delay increment of 13.3 ps within ~45 minutes per scan. All time-resolved measurements were performed while operating the spectrometer in WAM. In the experiments with liquid sample, the retardation voltage was applied to block the major part of the photoelectron yield arising from the ionization of water orbitals to maintain the count rate below 5000 Hz.

Cleaning of the experimental chamber and the liquid microjet system. In the end of experimental session, the cryogenic traps and the microjet were dismounted from the setup. The vacuum setup and cryogenic traps were cleaned from the residual sample. The liquid jet setup was abundantly purged with water. The vacuum setup was pumped

overnight to reach high vacuum in the experimental chamber and, thus, to ensure the optimal conditions for the measurements with Argon in the beginning of the next day.

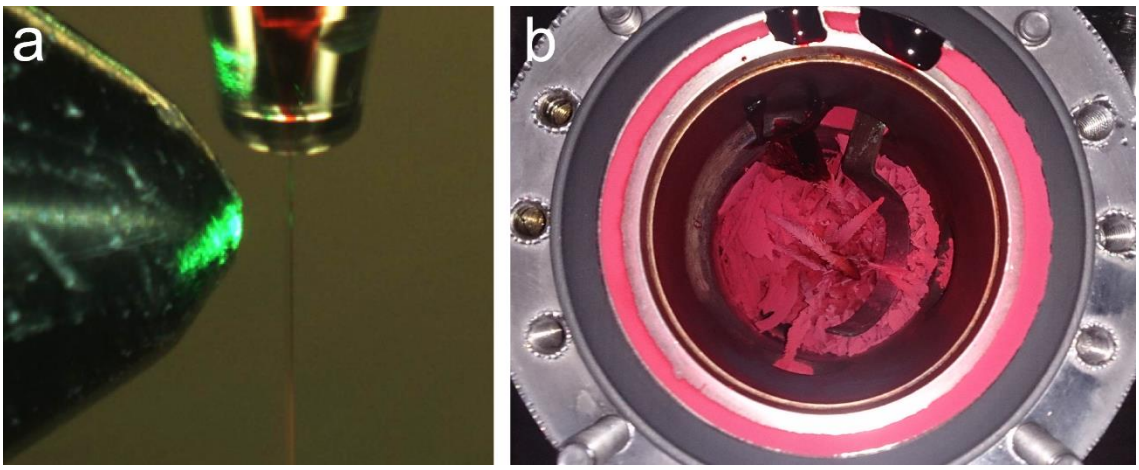

Figure 32. (a) A screenshot of the interaction region made with the monitoring camera during the experiment. The line of green light on the spectrometer skimmer is produced by reflection of the 530 nm pump laser beam from the liquid microjet surface. (b) Frozen $[Fe(bpy)_3]^{2+}$ sample in the dismounted cryogenic trap after an experimental session.

5 Results and discussion of experimental studies

This chapter is partly based on the publication Moguilevski *et. al.* 2017 *ChemPhysChem* **18**, 465 [176].

The results of experimental studies of the photoinduced electron dynamics in an aqueous solution of $[Fe(bpy)_3]^{2+}$ are presented and discussed in this chapter. Before a discussion of the pump-probe spectra, the steady-state XUV spectrum, recorded without applying the optical pump beam, will first be considered in order to determine the binding energies of the molecular orbitals of the solvent and solute in their ground states. The energy of the Fe(II) 3d(t_{2g}) orbitals will be used as a reference to track the electron population dynamics on an absolute energy scale.

The main objective of this work is to reveal the mechanism of the SCO process in $[Fe(bpy)_3]^{2+}$ induced via resonant photoexcitation of the singlet MLCT state at a wavelength of 530 nm. The photoinduced electron dynamics takes place on two rather different time scales, corresponding to the population of the high-spin quintet state and the relaxation of this state to the ground state of the transition metal complex. The SCO transition itself is rather fast and occurs on a time scale of 100 fs, while the relaxation of the high-spin state takes several hundreds of picoseconds. Accordingly, the study involves two different measurements performed on a short- and long-time scale. The short-time scale dynamics will be considered in detail first, including a global fit analysis of the transient spectra with the use of a kinetic model that allows for different de-excitation channels of the resonantly populated singlet MLCT state of $[Fe(bpy)_3]^{2+}$. The results of the data analysis are supported by theoretical calculations carried out in collaboration with the theory group of Prof. Kühn (Rostock University).

5.1 Steady-state photoelectron spectrum of $[Fe(bpy)_3]^{2+}$ in water

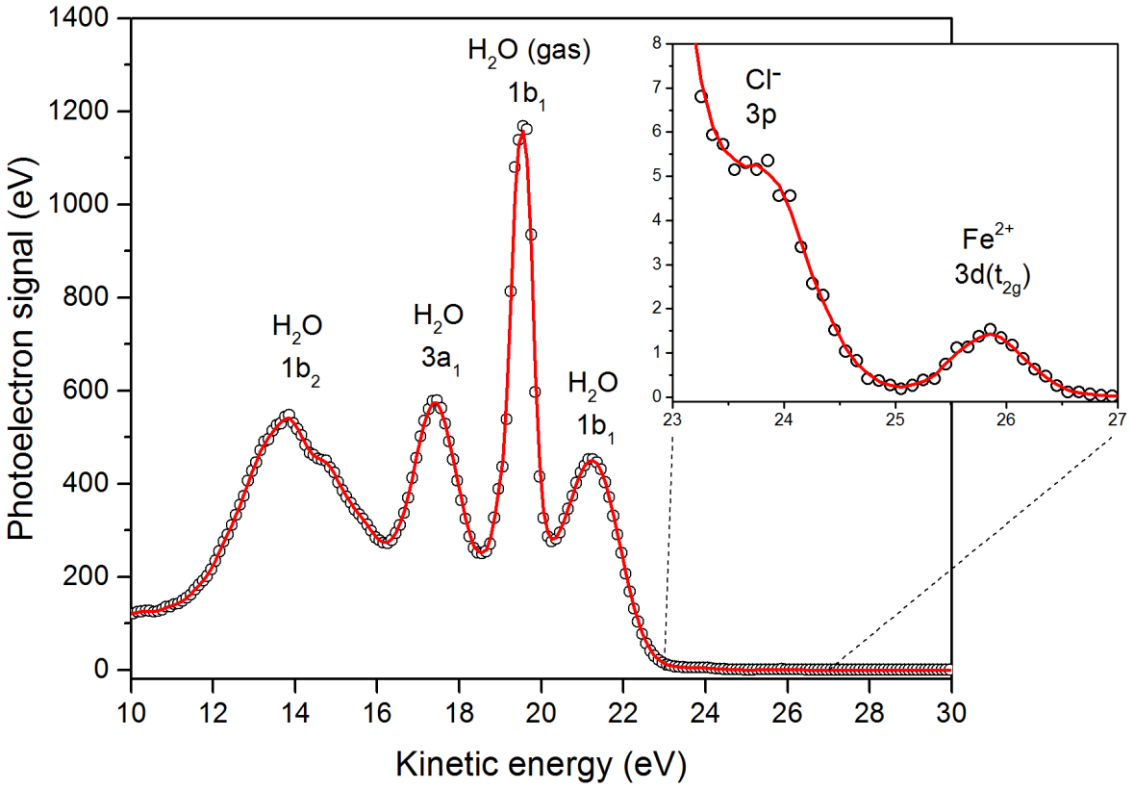

Figure 33. Steady-state energy spectrum of photoelectrons generated by the XUV beam from 50 mM aqueous solution of $Fe(bpy)_3Cl_2$. Spectral peaks are attributed to ionization from the iron-center-localized Fe $3d(t_{2g})$ orbitals, Cl^- 3p, and the $1b_1$, $3a_1$ and $1b_2$ water orbitals. The red curve represents a smoothed envelope of the spectrum.

The steady-state PES study is performed on a 50 mM aqueous solution of $Fe(bpy)_3Cl_2$ by employing the time-of-flight electron spectrometer presented in Section 4.2. The XUV beam with the photon energy of 32.55 eV, generated in the HHG setup, was used to obtain the spectrum shown in Figure 33. The spectrum represents an average of four successive measurements of 15 minutes acquisition time. In this experiment, the spectrometer was operated in the drift mode, which allows detection of electrons with the kinetic energies in the full energy range. In order to prevent saturation of the detector by the large amount of slow electrons ionized from water, a negative auxiliary voltage of -10 V was applied to block off the electrons with kinetic energies below 10 eV. The kinetic energy range between 10 and 30 eV, shown in Figure 33, encompasses the photoemission yield from nearly the full valence shell of water in the liquid- and gas-phase, including the $1b_1$, $3a_1$ and $1b_2$ orbitals. It excludes only photoemission from the lowest $2a_1$ valence orbital. For the liquid-phase water this orbital has a binding energy of 30.9 eV [177],

giving rise to an energy peak at 1.65 eV on the kinetic energy scale. In the experiment this signal is cut by applying of the auxiliary voltage. Photoemission from the $2a_1$ orbital of gas-phase water is not possible with the use of the XUV photon energy of 32.55 eV applied here, since the $2a_1$ binding energy of 32.6 eV [177] exceeds the photon energy.

The difference in binding energies between the gas and liquid water orbitals consists of different contributions. Foremost, the smaller values of the binding energies in the liquid phase originate from electronic polarization by water molecules [177, 178]. This gives rise to the mean liquid-to-gaseous energy difference of 1.4 eV for the $1b_1$, $3a_1$, $1b_2$ and $2a_1$ orbitals, as reported by Seidel, Winter and Bradforth [178]. Secondly, the hydrogen bonding in liquid water also affects the binding energies of the valence-shell orbitals. This effect is much weaker than the first one and leads to the energy difference in the order of 0.1-0.2 eV [177, 178].

The gas components in the water spectrum are highly prominent. One can expect this, since the spot size of ~75 µm of the XUV focus is significantly larger than the size of 22 µm of the liquid jet. Therefore, the ionization contribution from the vapor surrounding the jet is unavoidable. The spectral peaks arising from ionization of liquid and gaseous water are designated in Figure 33. Their assignment is based on the experimental results reported by Kurahashi et al. [179]. The inset of the Figure 33 shows in greater detail the energy range containing the spectral contributions of the solute, $[Fe(bpy)_3]^{2+}$ and the chloride counter ion. The assignment of the chloride contribution in the spectrum is consistent with the value of the $Cl^-(3p)$ binding energy previously reported by Kurahashi et al. [179]. The contribution of the $[Fe(bpy)_3]^{2+}$ in the spectrum is assigned according to the theoretical calculations performed by the group of Prof. Kühn. Electron emission from the iron-center-localized Fe $3d(t_{2g})$ orbital at the kinetic energy of 25.8 eV is well pronounced in the spectrum. The ratio in the photoelectron signal between the $1b_1$ liquid water peak and Fe $3d(t_{2g})$ peak is approximately 300:1. According to the theoretical calculations, photoemission from the ligand π orbitals of $[Fe(bpy)_3]^{2+}$ is overlapping on the energy scale with the $1b_1$ peak from liquid water. Therefore, since the photoelectron yield from the solute is much lower than the signal from solvent, the ionization signal from the π orbitals cannot be distinguished in the steady-state spectrum shown in Figure 33.

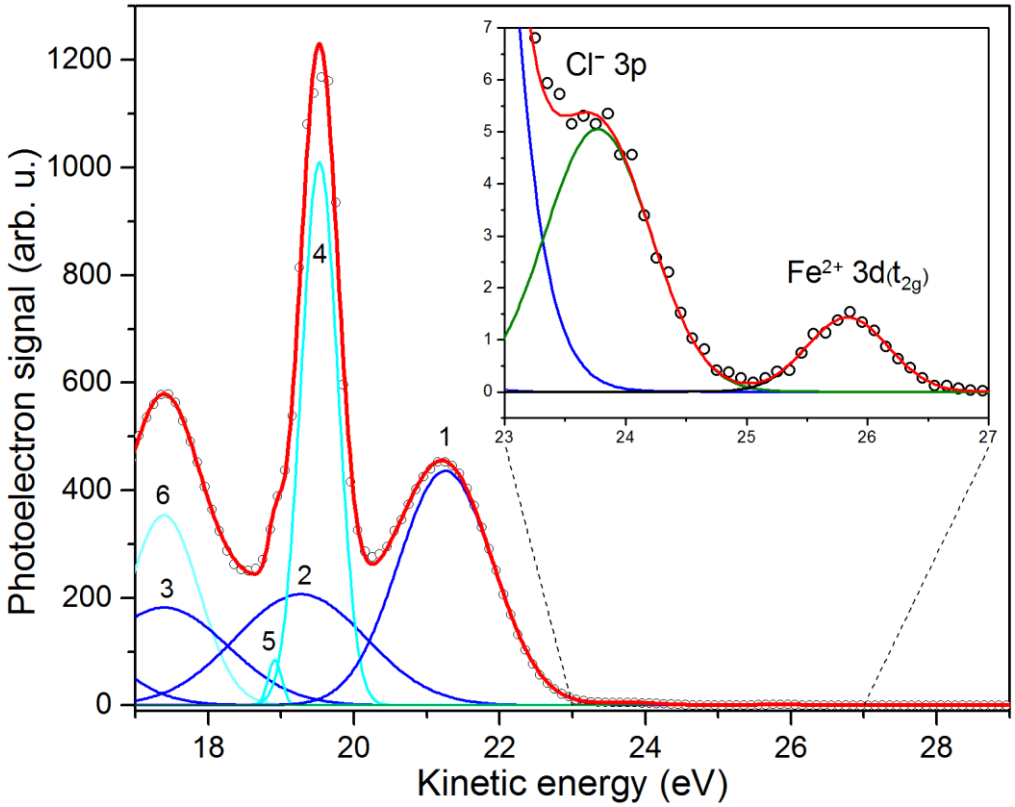

Figure 34. Spectral decomposition of the steady-state energy spectrum of photo-electrons generated by the XUV beam from 50 mM aqueous solution of $Fe(bpy)_3Cl_2$. Red curve presents a fit of the spectrum to a superposition of Gaussian profiles assigned to the Fe $3d(t_{2g})$, Cl^- 3p, and the $1b_1$ and $3a_1$ orbitals of water in gas and liquid phase. The contribution of the liquid water orbitals is represented by the blue lines (1 = $1b_1$, 2 = $3a_1$ H, 3 = $3a_1$ L) and of the gaseous water by the cyan lines (4 = $1b_1$, 5 = $1b_1$ v_1, 6 = $3a_1$).

Figure 34 displays the results of a fit analysis of the XUV photoelectron spectrum presented above. The fit function represents a superposition of Gaussian profiles describing contributions from the $1b_1$ and $3a_1$ orbitals of water in the liquid and gas phase, as well as from the $Cl^-(3p)$ and Fe(II) $3d(t_{2g})$ orbitals. The kinetic energy range between 10 eV and 16 eV is not considered in the analysis. According to the literature, ionization from the $1b_2$ orbitals of liquid- and gas-phase water should contribute to the spectrum in this energy range [177]. However, the shape of the measured spectrum suggests the presence of at least one additional band, besides these two known spectral peaks. Because of the lack of information needed to identify the unknown band structure and since the spectral range between 10 eV and 16 eV is irrelevant for the study of electron dynamics in $[Fe(bpy)_3]^{2+}$, this range was excluded in the fitting procedure. The center energy, the width, and the amplitude of each Gaussian profile were treated as fit parameters in the fit routine. The initial values of the parameters were chosen according to the previous results from photoelectron spectroscopy studies on water [177, 180].

The spectrum of photoelectrons ionized from the $3a_1$ orbital of liquid water consists of two peaks, which were considered in the fit analysis. The origin of this splitting represents a controversial topic. Three different interpretations were reported in literature. In one of them [177], the splitting is explained to arise from the Davydov interaction between two molecules of different orientation, similar to the splitting of the $3a_1$ peak in crystal ice. According to another study, this splitting originates from the interaction with the neighboring $1b_1$ orbital of liquid water [180]. The third study explains the splitting of the $3a_1$ peak as being due to the distortion induced by the hydrogen-bonding, which gives rise to especially strong influence on the $3a_1$ orbital because of its geometrical structure. The latter work describes the splitting of the $3a_1$ state in terms of the bonding and antibonding bands of liquid water, which is similar to ice. However, the variations of the local geometry caused by the anisotropy of liquid water structure lead to the smearing of the peak shape in contrast to ice, where the splitting is more pronounced [181]. The strong influence of the hydrogen-bonding on water molecules explains also the broadening of the spectral peaks in the liquid-phase [178].

In contrast to the liquid-phase, the width of the spectral peaks of the gaseous water allows us to resolve the vibrational excited states of the $1b_1$ orbital. The fit function in the data analysis presented here includes the first vibrational excited state v_1 of the $1b_1$ water orbital in the gas phase [182]. The $Cl^-(3p)$ contribution is represented by a single Gaussian profile, since the spin-orbit splitting of 0,11 eV [183] of the ground state of chloride is much smaller than the energy resolution in the present experiment. The same applies to the spectral contribution of the Fe $3d(t_{2g})$ orbital, which also exhibits a small splitting of ~0.1 eV according to the theory predictions. Its origin was discussed in detail in the Section 2.3.1. The binding energies of the orbitals of H_2O, Cl^-, and $[Fe(bpy)_3]^{2+}$ listed above were obtained by calculating the difference between the energy of the XUV photon and the central kinetic energies of the Gaussian peaks. The results are summarized in the Table 1, where the binding energies are compared with the literature values. One can see that the results obtained for water and chloride are in a satisfactory agreement with the previously reported results.

For a more accurate determination of the binding energies, a special care should be taken in the experiment regarding the effect of the streaming potential. The streaming potential originates from friction of the liquid flow in the quartz capillary, leading to electrostatic charging of the microjet, and affects the kinetic energy of the ionized

electrons [179, 184]. This effect gives rise to a shift of spectral peaks, which is different for the gaseous and liquid water contributions. A precise determination of the binding energies, however, lies beyond the scope of the present work.

	Fe^{2+} $3d(t_{2g})$	Cl^-	Liquid water			Gaseous water		
			$1b_1$	$3a_1$ H	$3a_1$ L	$1b_1$	$1b_1$ v_1	$3a_1$
E_{kin}	25.8	23.7	21.3	19.3	17.4	19.5	18.9	17.4
$\lvert E_{kin}-E_{ph}\rvert$	6.8	8.9	11.3	13.3	15.2	13.1	13,7	15,2
Nishizawa et al.	-	9.5(2)	11.31(4)	13.08(7)	14.47(7)	12.62	-	14.8
Winter et al.	-	-	11.16(4)	13.50(10)		12.60	-	14.84(2)

Table 1. Electron kinetic energies and corresponding binding energies determined from the Gaussian fit of the steady-state XUV spectrum obtained for an aqueous solution of $Fe(bpy)_3Cl_2$. The streaming potential was not considered in the derivation of binding energies. The literature values are presented for comparison and are taken from Nishizawa et al. [180] and Winter et al [177]. All values are given in eV. The error for the electron kinetic energy E_{kin} was estimated to be ±0.1 eV according to the XUV bandwidth measurement presented in [169].

The experimental value of binding energy for the Fe $3d(t_{2g})$ orbital was not reported to date. Nevertheless, there are two studies reporting on the binding energy of the iron-center localized $3d(t_{2g})$ orbital of another transition metal complex, $[Fe(CN)_6]^{4-}$, in aqueous solution, which possesses the octahedral symmetry and the d^6 low-spin electronic configuration in the ground state. The reported values are 6.1 eV [185] and 6.2 eV [186]. Despite the difference in ligands bound to the central Fe(II) atom, those values are close to the result of the present measurement giving a binding energy of 6.8 eV. The width of the Fe $3d(t_{2g})$ peak is 0.78 ± 0,04 eV, as obtained from the fit.

Since the precise determination of the binding energies was not in the focus of this work, a relative energy scale will be used in the following chapters. The well separated energy peak of the Fe $3d(t_{2g})$ orbital in the XUV spectra serves as a good reference for tracking the transient electron population distribution on the energy scale. Thus, the Fe $3d(t_{2g})$ binding energy of the ground low-spin state of $[Fe(bpy)_3]^{2+}$ is assigned to zero.

5.2 Time-resolved spectrum of $[Fe(bpy)_3]^{2+}$ on a sub-picosecond time scale

5.2.1 First insights

The first time-resolved measurements with a photoexcitation at a wavelength of 530 nm were carried out with the use of TOF spectrometer in the wide angle mode. The optical pump laser beam was loosely focused onto the liquid jet. Figure 35 compares time-resolved spectra of aqueous solutions of 50 mM $[Fe(bpy)_3]^{2+}$ and 500 mM $[Fe(CN)_6]^{4-}$, obtained under approximately equal conditions in two single scans with the same data acquisition time of 20 seconds for each delay stage position. In both cases the pump pulse with the wavelength of 530 nm and the time-averaged energy flux of ~65 W/cm² was applied for the photoexcitation of the samples. The time resolution in the experiment presented in Figure 35 was ~140 fs.

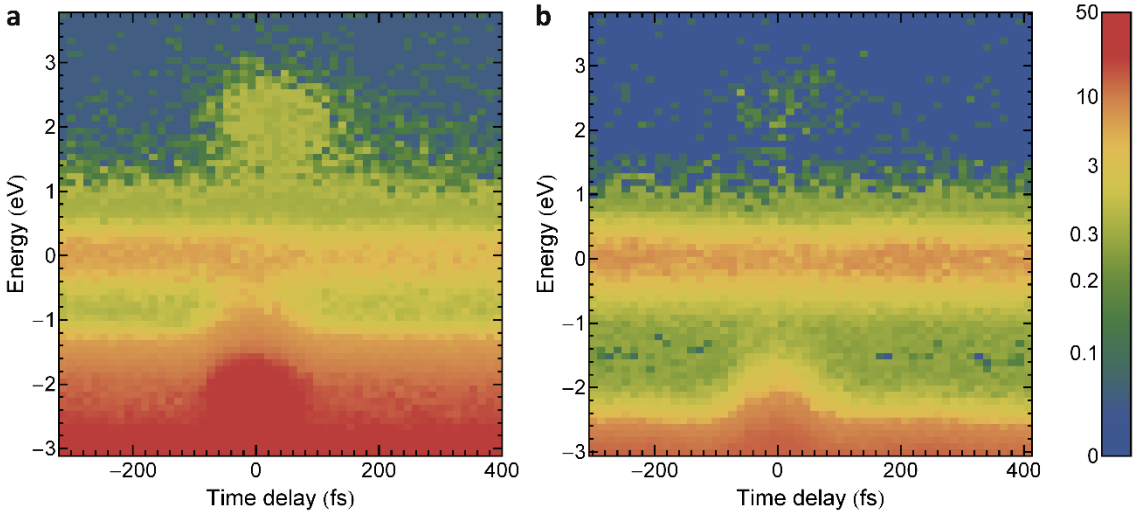

Figure 35. Photoelectron signal as a function of the excitation energy and the time delay between the optical pump and XUV probe pulses. The data are obtained for aqueous solutions of (a) 50 mM $[Fe(bpy)_3]^{2+}$ and (b) 500 mM $[Fe(CN)_6]^{4-}$. In both panels, the vertical scale shows the relative energy with respect to the emission peak from the Fe 3d(t_{2g}) orbitals.

The results of the measurement with $[Fe(bpy)_3]^{2+}$ are presented in Figure 35(a), where a sequence of transient spectra recorded at different pump-probe time delays in the range between -300 and 400 fs is shown on both the time and energy scales. The data reveal a prominent transient signal in the kinetic energy range lying at ~2.3 eV above the

Fe 3d(t_{2g}) ground state peak, which is comparable to the photon energy of the optical pump. A cross-correlation signal of ionization of the Fe 3d(t_{2g}) orbital is also present in the data shown in Figure 35(a). However, one can unambiguously distinguish a longer life time of the transient signal as well as its asymmetric shape with respect to the zero time delay. Moreover, the Fe 3d(t_{2g}) peak exhibits a signal depletion at positive time delays. The depletion appears immediately after photoexcitation of the sample and remains constant within the whole time-delay range in this experiment.

Figure 35(b) shows the results of the measurement performed with $[Fe(CN)_6]^{4-}$. The XUV spectrum of $[Fe(CN)_6]^{4-}$ also exhibits a spectral component of ionization from the Fe 3d(t_{2g}) orbitals. As in the case of $[Fe(bpy)_3]^{2+}$, the center of the emission peak from the Fe 3d(t_{2g}) orbitals of $[Fe(CN)_6]^{4-}$ is assigned to zero on the relative energy scale. In contrast to $[Fe(bpy)_3]^{2+}$, the molecule of ferrocyanide does not possess charge transfer states which can be resonantly excited from the ground state at the wavelength of 530 nm. Therefore, one can see from Figure 35(b) that the transient signal contribution is not present in the pump-probe spectra of $[Fe(CN)_6]^{4-}$. Only a weak symmetric cross-correlation signal of ionization from the Fe 3d(t_{2g}) orbital of $[Fe(CN)_6]^{4-}$ appears at 2.3 eV above the Fe 3d(t_{2g}) peak at short time-delays. The weak signal depletion of the Fe 3d(t_{2g}) peak appears only around zero time delay simultaneously with the rise of the cross-correlation signal. This implies that the phototransition cross section is much lower, which is a consequence of the absence of a resonance condition.

5.2.2 Data acquisition

After the optimization procedure described in the Section 4.4.3, it was possible to perform further experiments with the time resolution of 60 fs. The optical pump laser beam was loosely focused onto the jet. With the pump pulse energy attenuated to 3 µJ, the average intensity was approximately 88 W/cm^2 in the interaction region. The data acquisition was broken in a sequence of multiple time-delay scans in the range between -100 and 500 fs. Each scan was carried out within 15 minutes with a delay increment of 13.3 fs and acquisition time of 10 seconds per delay position.

5.2.3 Data processing

The individual time-delay scans were added together prior to the data analysis. While combining the series, the data sets were corrected for the energy shift and the drift of the zero time delay. The energy shift was caused by the space-charge effect induced by the pump beam in the liquid sample, which was discussed in the Section 3.2.6. This shift was shown to be dependent on the time delay between the pump and probe pulses [133]. Therefore, each spectrum of a given series needed to be corrected separately. The ionization signal from the Fe 3d(t_{2g}) orbital, giving rise to a well distinguished energy peak in each XUV spectrum, was used as a reference since less than 20% of the $[Fe(bpy)_3]^{2+}$ molecules were excited by the pump beam. A Gaussian fit was used to determine the central energy of this peak and the origin of the kinetic energy scale was assigned to the fit value. The energy shift within a chosen single time-delay scan is demonstrated in Figure 36.

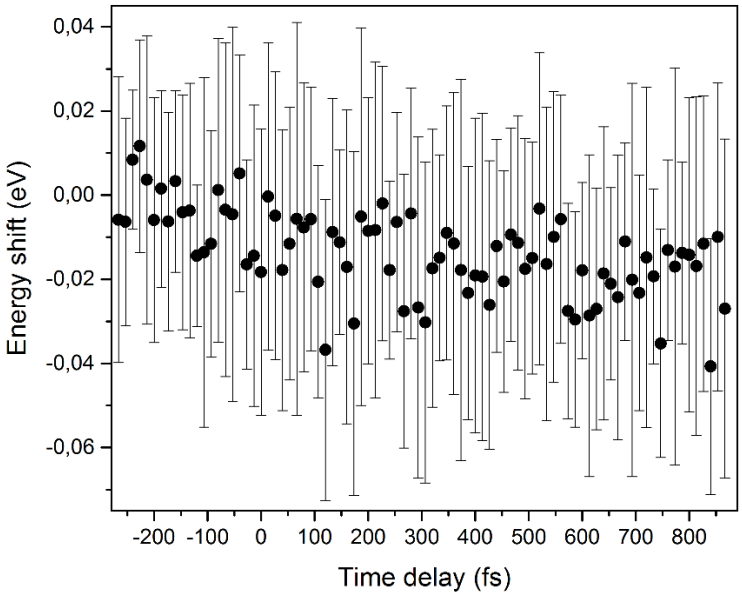

Figure 36. The shift of the central energy of the Fe 3d(t_{2g}) peak caused by the space-charge effect as a function of the time delay. The results are shown for a chosen single time-delay scan.

These results exhibit a rather small energy shift over the time window of the scan, which is much smaller than the effect demonstrated in Figure 18. One should note that the space-charge effect discussed in the Section 3.2.6 was considered on the nanosecond time scale, whereas a much shorter time delay interval in the picosecond range is considered in the present experiment. In addition, the photon energy applied in the present

experiment is considerably smaller than in Ref. [133], whereas the peak intensity of the pump beam in the both experiments is in the same order of magnitude. Therefore, according to the discussion in the Section 3.2.6, the space charge effect should be less pronounced in the present experiment.

The drift of the zero time delay was caused by changes in the environmental conditions in the lab and could reach a value of ~160 fs during the day. This drift was corrected according to the center position of the cross-correlation signal in each time-delay scan.

5.2.4 Time-resolved spectrum

A closer consideration of the spectra in the energy domain reveals more details in the transient signal above and also below the Fe 3d(t_{2g}) peak. Figure 37 presents a series of pump-probe XUV spectra recorded at six chosen time delays of −107 fs, 0 fs, 80 fs, 120 fs, 160 fs, and 307 fs between the pump and probe pulse. As mentioned before, the origin of the energy scale (the horizontal scale in the figure) is assigned to the central energy of the photoemission peak from the Fe 3d(t_{2g}) orbitals of the ground state of $[Fe(bpy)_3]^{2+}$. At the negative delay of −107 fs, the probe pulse interacts with the sample first and the spectrum recorded at this position resembles the steady-state spectrum shown in Figure 33. At zero delay, a significant contribution to the spectrum arises from the cross-correlation yield of the pump and probe beams, which dominates the transient signal in the full energy range considered here. The spectra recorded at positive time delays reveal the photoemission signal from short-lived transient states (marked with blue color). The transient signal appears not only at kinetic energies within 3 eV above the Fe 3d(t_{2g}) peak but also within 4 eV below this peak. The latter is more pronounced on a linear scale of the electron yield presented in the right panel of Figure 37. In this panel, one can also distinguish the population depletion (marked with green color) in the ground electronic state by the pump beam. A logarithmic vertical scale is used instead in the left panel of Figure 37 to pronounce the contribution of the transient signal above the Fe 3d(t_{2g}) peak, since its amplitude is by almost one order of magnitude lower than the ionization yield from the Fe 3d(t_{2g}) orbitals.

A quantitative analysis of the ultrafast evolution of pump-probe spectra is rather complicated, especially in the range of negative energies, because the transient signal is much weaker than the background signal from unexcited $[Fe(bpy)_3]^{2+}$ and water. A

background subtraction was carried out first to sort out only the transient signal and to bare the details hidden in the pump-probe spectra, which are discussed in the next section.

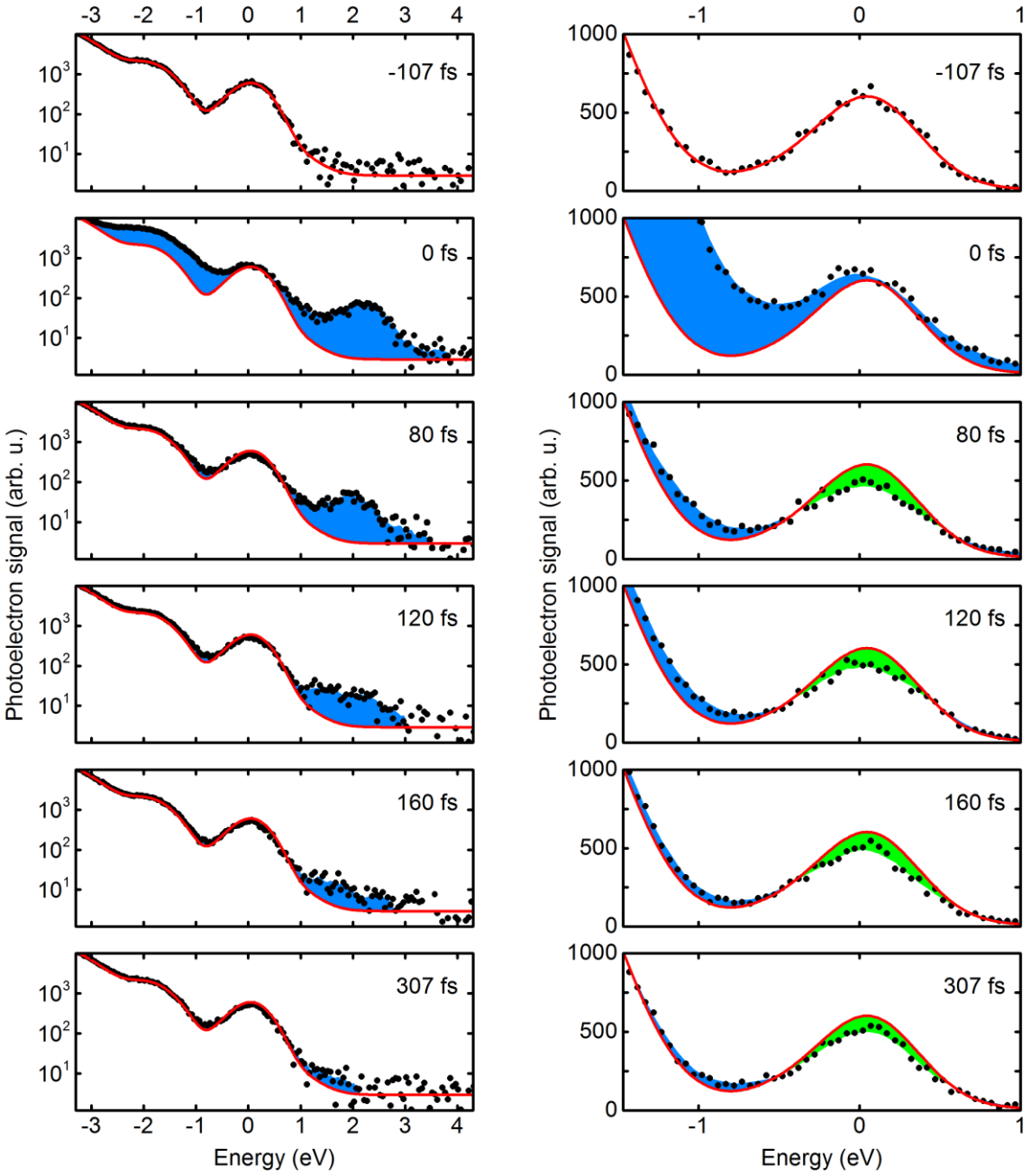

Figure 37. Left column: Photoelectron energy spectra for the selected time delays between the pump and probe pulses: −107, 0, 80, 120, 160, and 307 fs. The photoelectron signal is plotted on a logarithmic scale. The red curve represents the fit to the XUV ionization yield when the pump beam is not applied (see Figure 33). The transient emission signal is marked by blue color. The kinetic energy is given with respect to the emission peak of the Fe 3d(t_{2g}) orbitals. Right column: The photoelectron signal is plotted on a linear scale, enabling us to reveal in greater detail the transient signal (blue) at negative energies with respect to the Fe 3d(t_{2g}) emission peak, and the decrease (green) of this peak due to depletion of the ground state of the metal complex by the pump beam.

5.2.5 Transient signal

The transient signal was derived by subtracting the XUV negative-delay spectrum as a background from pump-probe spectra. To define the background signal, the spectra recorded at negative time delays below -80 fs were combined together. This subtraction yielded the transient signal which was analyzed in terms of kinetic models presented below in the Section 5.2.6. The two-dimensional plot in Figure 38 shows the transient signal dependency on the excitation energy and the time delay. The negative value of the transient signal at kinetic energies corresponding to the Fe 3d(t_{2g}) peak position (that is at zero energy since the origin is assigned to this peak) arises due to the above mentioned depletion of the ground state. The negative signal also appears in an energy interval around -4 eV at short time delays within 100 fs. As will be discussed later, ionization from the ligand-donated π orbital of the ground state of $[Fe(bpy)_3]^{2+}$ contributes to the energy spectrum of photoelectrons at this energy interval. Thus, the negative signal around the energy of – 4 eV appears also due to the depletion of the ground state.

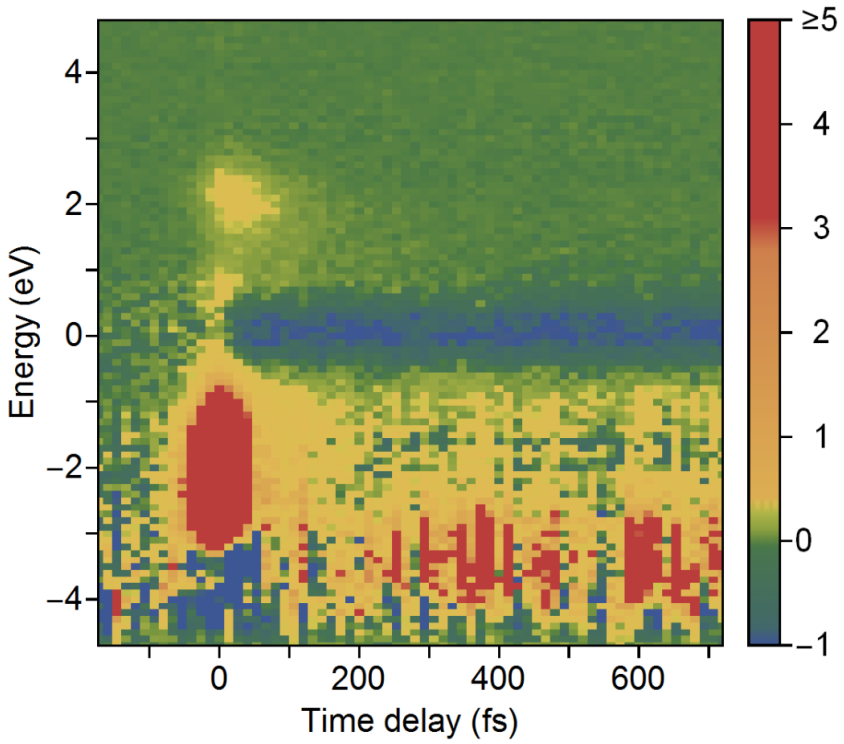

Figure 38. Transient signal as a function of the excitation energy and the time delay. The transient signal was derived by subtracting the XUV negative-delay spectrum shown in the upper panel of Figure 38 from the pump-probe spectra.

However, ionization of the transient excited states, which are formed during electron relaxation following the photoexcitation event, also contributes to the spectral range at -4 eV. As a result, the transient signal at this energy acquires the positive sign on the short time scale of 100 fs, which reflects the ultrafast character of the relaxation dynamics.

Changes in the electronic structure caused by intersystem crossings and internal conversion as well as geometrical relaxation and vibrational cooling lead to different signatures in the photoelectron spectra. One should note that the difference in photoelectron signals resulting from various electronic states possessing the same unrelaxed nuclear geometry is mainly due to exchange energy contribution, whereas geometrical relaxation leads to substantial lifting of orbital degeneracies. In addition, the ionization from a given state can lead to the formation of ion states with different electronic configurations and multiplicities, giving rise to a number of features in the photoelectron spectrum. All these issues were taken into account by the global fit model, presented in next section, to reveal the individual contributions from the transient states. The possibility of both the sequential and direct transition to the quintet state was considered in the data analysis. Independent of the model applied, the global fit reveals ionization contributions from at least three short-lived intermediate states characterized by decay time constants of approximately 10, 60, and 80 fs.

A contribution from the long-lived quintet state is also apparent in the transient signal shown in Figure 38 at energies between −4 and −2.5 eV below the Fe 3d(t_{2g}) peak. In fact, the formation of this state leads to the recovery of the negative signal caused by the depletion of the initial ground state. The life time of 650 ps of the quintet state was inferred from an additional measurement where the time delay was scanned in the nanosecond range. Details of this experiment will be presented later in the Section 5.3.

5.2.6 Kinetic models

In the previous studies, presented in the Sections 2.3.3 and 2.3.4, the singlet, two triplet, and quintet electronic states of $[Fe(bpy)_3]^{2+}$ were denoted considering the octahedral symmetry nomenclature as $^1A_{1g}$, $^3T_{1g}$, $^3T_{2g}$, and $^5T_{1g}$, respectively. Triplet and quintet states have near triple degeneracy and their symmetry is not octahedral in the reality. To simplify the description of the electronic states while considering the reduction of symmetry, these states will be denoted according to their multiplicity and cardinal

number with labels S_0, T_1, T_2, and Q_1 in the following text. To distinguish between the vertically populated, vibrationally hot quintet state from the adiabatically cooled but not yet equilibrated quintet state, further notations of Q_1^{**} and Q_1^{*} will be used for these states, respectively.

A global fit of different kinetic models was carried out to analyze the experimental data. By applying a statistical F-test, we have found that an additional short-lived transient state needs to be considered in the SCO mechanism, as compared to both direct (I) and the sequential (II) mechanisms discussed in the Chapter 2. Both model I and II, involving population of one intermediate state in the de-excitation pathway from the ^{1,3}MLCT states to the relaxed quintet state Q_1, can be expressed as:

$$S_0 \xrightarrow{P(t)} {}^{1,3}\mathrm{MLCT} \xrightarrow{k_1} X \xrightarrow{k_2} Q_1^{*} \qquad (38)$$

where P(t) denotes the photoexcitation rate of the ^{1,3}MLCT states from the ground S_0 state, X represents the triplet state T_2 in model II and the vibrationally hot quintet state Q_1^{**} in model I, respectively, and k_i are the corresponding transition rates. Equation (38) describes a "nested" model for the two extended models considered below. In one extended model we consider that the ^{1,3}MLCT state relaxes to the quintet state via a cascaded population of two triplet intermediate states, as described in Ref. [82]:

$$S_0 \xrightarrow{P(t)} {}^{1,3}\mathrm{MLCT} \xrightarrow{k_1} T_1 \xrightarrow{k_2} T_2 \xrightarrow{k_3} Q_1^{*} \qquad (39)$$

Another model assumes two parallel relaxation channels occurring simultaneously:

$$S_0 \xrightarrow{P(t)} {}^{1,3}\mathrm{MLCT} \begin{cases} \xrightarrow{k_1} T_{1,2} \xrightarrow{k_3} Q_1^{*} \\ \xrightarrow[k_2]{} Q_1^{**} \xrightarrow[k_4]{} Q_1^{*} \end{cases} \qquad (40)$$

where the two triplet states are treated as a single $T_{1,2}$ state because of their ultrafast internal conversion [82].

The global fit routine (see details in the next section) was applied to fit the transient spectral signal with 96 × 68 data points on the energy and time scale, respectively. To compare the extended and the "nested" models, the *F* statistic is calculated, given by

$$F = \frac{(\chi_n^2 - \chi_e^2)(n - p_e)}{\chi_e^2 (p_e - p_n)}, \tag{41}$$

where χ_e^2 and χ_n^2 are the χ^2 values of the extended and "nested" model, respectively, p_e and p_n are the corresponding numbers of fit parameters, and n is the number of data points. The extended model yields always a better (or at least equal quality) fit. However, the smaller χ_e^2 value is statistically significant only if the F statistic exceeds a critical value F_c defined by the F-distribution function. When the criterion $F_c < F$, $F_c = F(p_e - p_n; n - p_e)$ is satisfied, the simpler "nested" model can be rejected with greater than 95% confidence. This criterion is well satisfied when comparing both the cascaded (Equation (39)) and the parallel (Equation (40)) model with the "nested" model. The corresponding inequalities are 3.0 < 133.6 and 2.6 < 89.1 (with p_n = 10 for the "nested" model, p_e = 12 for the cascaded model and p_e = 13 for the parallel model), pointing to the significance of the additional transient state in both extended models. This is illustrated in Figure 39 which shows the residuals for the best fit by different models. The domain where the "nested" model is deficient in reproducing the experimental data is marked in panel (a) by white rectangles. The decay time constants (inverse values of the transition rates) obtained for different kinetic models are summarized in Table 2.

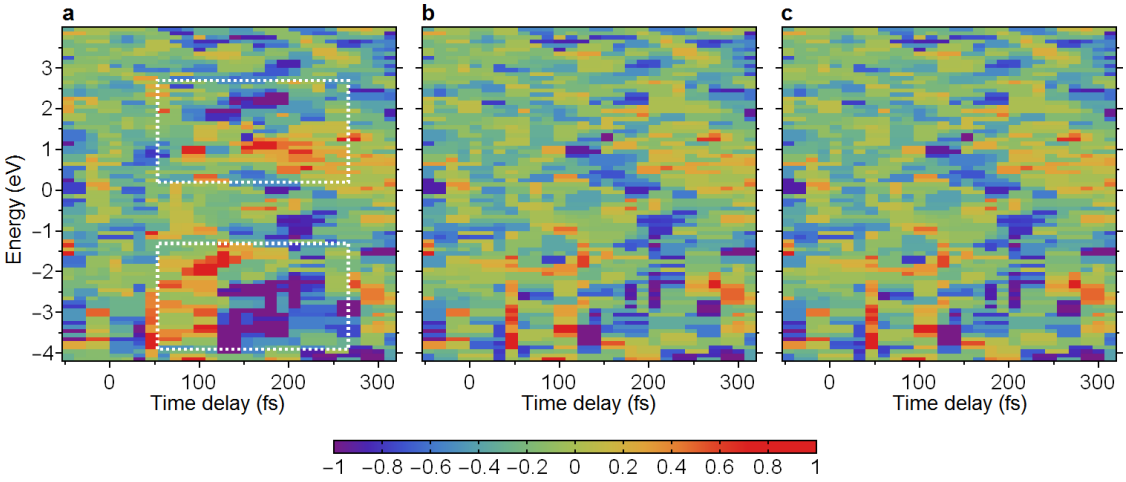

Figure 39. Residuals for the best fit by different models. The difference between the measured transient signal and the global fit results is shown for the "nested" model (a), the model of parallel relaxation (b), and the cascaded model (c). The data are shown in the range of time delays where the difference in residuals is most pronounced. The domain where the "nested" model is deficient in reproducing the experimental data is marked in panel (a) by white rectangles.

Based merely on the F-test results, we cannot judge which extended model is the proper one. Both the parallel and the sequential models yield approximately the same χ^2 value of 2846.6 and 2846.5, respectively, which is smaller than the value of 2965.6 of the "nested" model. The choice of the model is, therefore, made with the help of theoretical calculations. The comparison of predictions with the fit results for the parallel and cascaded models are shown in Figure 44 in the panels (a,b) and (c,d), respectively. Whereas the theory reproduces well the emission band structure of the $T_{1,2}$ and Q_1^{**} states populated in the parallel relaxation process, only the T_2 emission spectrum can be reproduced in the cascaded model. For the T_1 state, the fit results disagree with the predictions in the energy range below the Fe 3d(t_{2g}) peak. Therefore, we reject the cascaded relaxation mechanism.

Extended model: parallel relaxation				
Transition	^{1,3}MLCT→$T_{1,2}$	^{1,3}MLCT→Q_1**	$T_{1,2}$→Q_1*	Q_1**→Q_1*
Lifetime (fs)	20 ± 20	90 ± 25	70 ± 20	35 ± 20
Extended model: sequential relaxation				
Transition	^{1,3}MLCT→T_1	T_1→T_2	T_2→Q_1*	
Lifetime (fs)	25 ± 20	30 ± 20	80 ± 30	
"Nested" model				
Transition	^{1,3}MLCT→X	X→Q_1*		
Lifetime (fs)	25 ± 20	30 ± 20		

Table 2. Fitted model parameters. Time constants, representing inverse values of the corresponding transition rates, obtained from the global fit to different kinetic models. In the "nested" model, the state X represents either the $T_{1,2}$ state or the Q_1^{**} state.

5.2.7 Global fit

As mentioned above, better fit results were obtained by applying a kinetic model that assumes two channels of ^{1,3}MLCT relaxation occurring simultaneously (see Equation (40)). The following system of differential equations describes the corresponding

population dynamics of the initially ($t \rightarrow -\infty$) unpopulated ^{1,3}MLCT, $T_{1,2}$, Q_1^{**}, and Q_1^{*} states:

$$\begin{aligned}
\frac{\mathrm{d}\left[^{1,3}\mathrm{MLCT}\right]}{\mathrm{d}t} &= P(t) - (k_1 + k_2)\left[^{1,3}\mathrm{MLCT}\right] \\
\frac{\mathrm{d}\left[\mathrm{T}_{1,2}\right]}{\mathrm{d}t} &= k_1\left[^{1,3}\mathrm{MLCT}\right] - k_3\left[\mathrm{T}_{1,2}\right] \\
\frac{\mathrm{d}[\mathrm{Q}_1^{**}]}{\mathrm{d}t} &= k_2\left[^{1,3}\mathrm{MLCT}\right] - k_4[\mathrm{Q}_1^{**}] \\
\frac{\mathrm{d}[\mathrm{Q}_1^{*}]}{\mathrm{d}t} &= k_3\left[\mathrm{T}_{1,2}\right] + k_4[\mathrm{Q}_1^{**}] - k_\mathrm{r}[\mathrm{Q}_1^{*}]
\end{aligned} \tag{42}$$

where k_r denotes the relaxation rate of the metastable quintet state Q_1^{*} to the ground S_0 state and other rate constants are introduced in Equation (40). The value of k_r is rather small, so that the Q_1^{*} relaxation is negligible on the subpicosecond time scale considered here. Taking into account that the excitation rate of the ^{1,3}MLCT states from the S_0 ground state is proportional to the pump intensity and assuming a Gaussian temporal envelope of the pump pulse, we have

$$P(t) = \sigma\, I_0 \exp\left(-\frac{t^2}{\tau_\mathrm{pump}^2}\right)[S_0]\,, \tag{43}$$

where σ is the photoexcitation cross section, I_0 is the intensity of the pump laser, and $[S_0]$ is the population of the ground state. Further, the Equation (43) can be evolved to

$$P(t) = B \exp\left(-\frac{t^2}{\tau_\mathrm{pump}^2} - \frac{\sqrt{\pi}}{2} B\tau_\mathrm{pump}\left(1 + \mathrm{erf}\left(\frac{t}{\tau_\mathrm{pump}}\right)\right)\right), \tag{44}$$

where the second term of the exponential function argument describes the depletion of the initial ground state by the pump pulse, τ_pump is the pulse width, erf(x) is the error function of argument x, B is a constant defined by a product of the photoexcitation cross section and the pump laser intensity, and the initial population of the ground state is normalized to unity. The constant B is treated as a fit parameter. The system of differential equations was solved numerically. The fit function describing the dependency of the transient signal on the time delay t and the photoelectron kinetic energy E_kin has the form

$$T(E_\mathrm{kin}, t) = \sum_\mathrm{J} T_\mathrm{J}(E_\mathrm{kin})\,[\mathrm{J}]^{*}(t) - T_{\mathrm{S}_0}(E_\mathrm{kin})\left(1 - [\mathrm{S}_0]^{*}(t)\right) + T_\mathrm{c}(E_\mathrm{kin}, t)\,, \tag{45}$$

where $T_J(E_{kin})$ represents the emission spectrum from the transient state J (J = ^{1,3}MLCT, $T_{1,2}$, Q_1^{**}, or Q_1^*), $T_{S_0}(E_{kin})$ is the emission spectrum from the ground state S_0, $[J]^*(t)$ is the transient population of state J convolved with the Gaussian temporal envelope of the XUV probe pulse:

$$[J]^*(t) = \frac{1}{\sqrt{\pi}\tau_{probe}} \int_{-\infty}^{+\infty} \exp\left(-\frac{(t-t')^2}{\tau_{probe}^2}\right) [J](t')dt' , \tag{46}$$

τ_{probe} is the probe pulse width, $[S_0]^*(t)$ is the time-dependent (due to the depletion) population of the ground state convolved with the temporal envelope of the probe pulse:

$$[S_0]^*(t) = \frac{1}{\sqrt{\pi}\tau_{probe}} \int_{-\infty}^{+\infty} \exp\left(-\frac{(t-t')^2}{\tau_{probe}^2} - \frac{\sqrt{\pi}}{2} B\tau_{pump}\left(1 + \mathrm{erf}\left(\frac{t'}{\tau_{pump}}\right)\right)\right) dt , \tag{47}$$

and $T_c(E_{kin}, t)$ is the cross-correlation yield:

$$T_c(E_{kin}, t) = T_c(E_{kin}) \exp\left(\frac{-t^2}{\tau_{pump}^2 + \tau_{probe}^2}\right), \tag{48}$$

The fit algorithm employs the matrix formalism introduced in Ref. [187], which significantly improves the computational efficiency. Following this approach, the transient signal is represented at the number of $N \times M$ data points on the energy and time scale by the matrix product:

$$T = A\, D^T , \tag{49}$$

where the matrix $A(N, s)$ describes the emission spectra of s transient states at the set of N data points on the energy scale whereas the matrix $D(M, s)$ describes the population of these states at the set of M data points on the time scale. The cross-correlation signal defined by Equation (48) is treated as a transient state as well. Thus, in the model of parallel relaxation the number of states is $s = 6$ (4 transient states, the ground state, and the cross-correlation).

For a given set of rate constants k_i and the constant B, representing the fit parameters, the matrix D is defined via the solution of differential Equations (42) and

from Equations (46), (47), and (48). The fit algorithm can be deduced to minimize the χ^2 value defined by [187]:

$$\chi^2 = \left\| T_{exp} - T_{exp} D^T (D D^T)^{-1} \right\|^2 , \tag{50}$$

where T_{exp} represents the 2D array of the experimental transient signal. Thus, this fit procedure finds the best values of fit parameters which describe the kinetics, whereas the spectral amplitudes can be found by applying the projection of T_{exp} on *D*. This approach was rather efficient in conducting the *F*-test.

To refine the band structure of the photoemission spectra, another fit routine was applied where $T_J(E_{kin})$ were represented by superpositions of Gaussian profiles and the Gaussian amplitudes, positions, and widths were also treated as fit parameters. The lifetimes of the ^{1,3}MLCT, $T_{1,2}$, and Q_1^{**} states were calculated as $(k_1 + k_2)^{-1}$, k_3^{-1}, and k_4^{-1}, yielding the values of 16 ± 13, 70 ± 20, and 35 ± 10 fs, respectively (see also Table 2). The branching ratio of $4.5^{+4.8}_{-1.5}$ between the relaxation channels of the ^{1,3}MLCT state to the $T_{1,2}$ and Q_1^{**} states, respectively, was inferred from the ratio of k_1 to k_2. The asymmetric error bar was inferred from the dependency of χ^2 as a function of k_1/k_2.

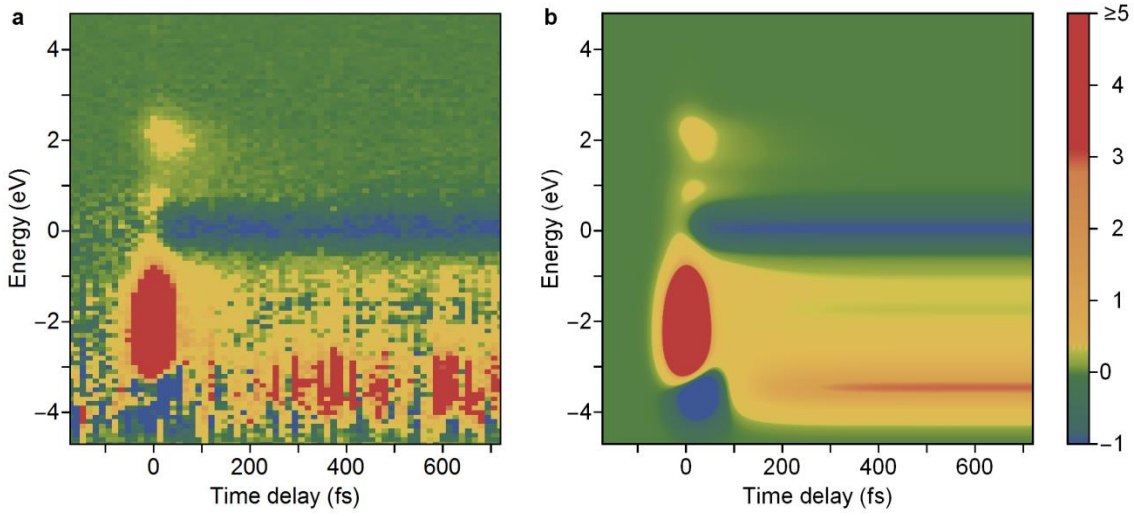

Figure 40. (a) Measured transient signal as a function of the excitation energy and the time delay. (b) Reproduction of the experimental data by a global fit with the use of the model that assumes parallel depopulation of ^{1,3}MLCT via formation of the Q_1^{**} and $T_{1,2}$ states, respectively.

The global fit results obtained with the use of the model described above are shown in Figure 40(b). One can see a very good agreement of the fit results with the experimental data, which have been shown in the Figure 38 and are reproduced in Figure 40(a) for

comparison. In addition to the contour plot shown in the Figure 40, time traces as well as energy traces at specific time delays and kinetic energies are shown in Figure 41 and Figure 42, respectively. The graphs incorporate the decomposition of the transient signal to the individual contributions from the involved states obtained from the fit in the energy and time domains. As already mentioned in Section 5.2.5, the depletion of the ground state gives rise to negative transient signal also at energies between -4.2 and -3.2 eV. This feature disappears within <100 fs due to the formation of the Q_1^* state contributing to the spectrum in the same energy interval. This provides the evidence that the SCO transition occurs on a sub-100 fs time scale.

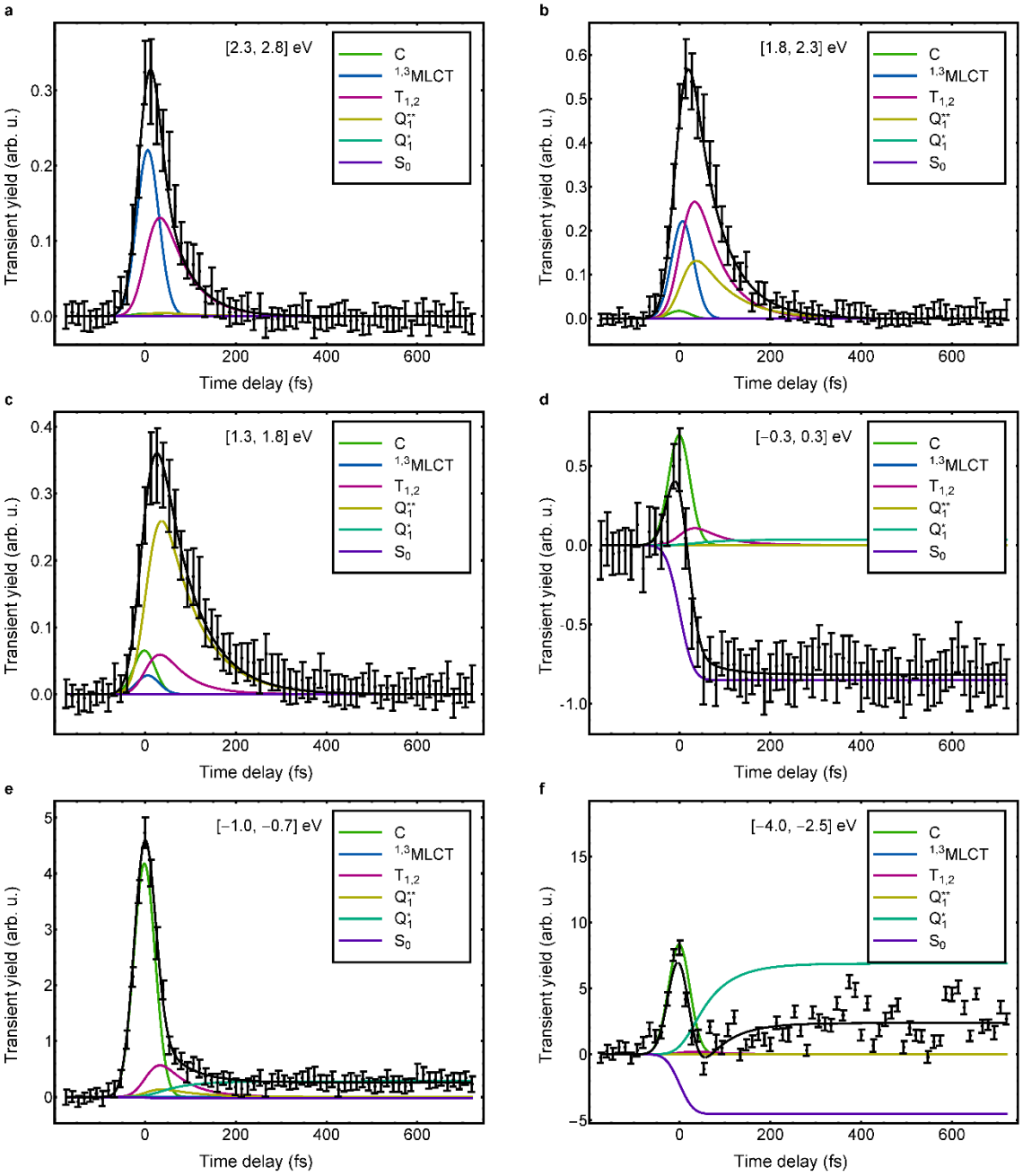

Figure 41. (a) Time dependency of the transient signal at different excitation energies. The signal integrated within the energy interval between 2.3 and 2.8 eV (dots with error bars). The black solid line represents the global fit result. The color lines show the signal decomposition to individual contributions from the ^{1,3}MLCT (blue), $T_{1,2}$ (red), Q_1^{**} (yellow), Q_1^{*} (cyan), and S_0 (violet) states as well as the cross-correlation contribution C (green). (b, c, d, e, f) The same as in (a) shown for the energy intervals (b) [1.8, 2.3] eV, (c) [1.3, 1.8] eV, and (d) [−0.3, 0.3] eV, (e) [−1, −0.7] eV, and (f) [−4, −2.5] eV, respectively. Note that the contribution from the S_0 state is of negative value due to the depletion of the ground state.

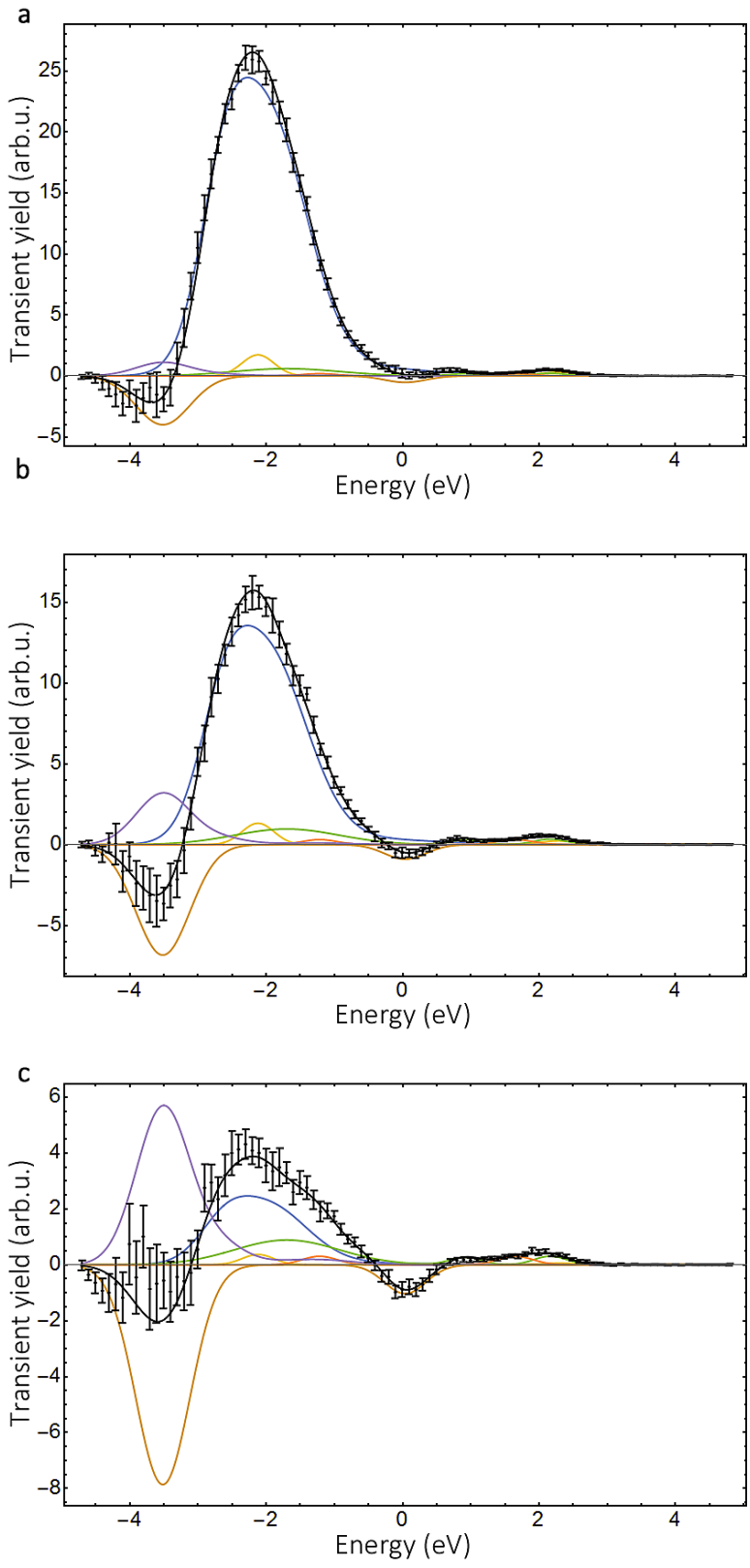

Figure 42.1. Energy distribution of the transient signal at different pump-probe time delays. The signal is integrated within the time-delay intervals between (a) [-10, 10] fs, (b) [10, 40] fs, (c) [40, 70] fs (dots with error bars). The black solid line represents the global fit result. The color lines show the signal decomposition to individual contributions from the ^{1,3}MLCT (yellow), $T_{1,2}$ (green), Q_1^{**} (orange), Q_1^{*} (violet), and S_0 (brown) states as well as the cross-correlation contribution C (blue). Note that the contribution from the S_0 state is of negative value due to the depletion of the ground state.

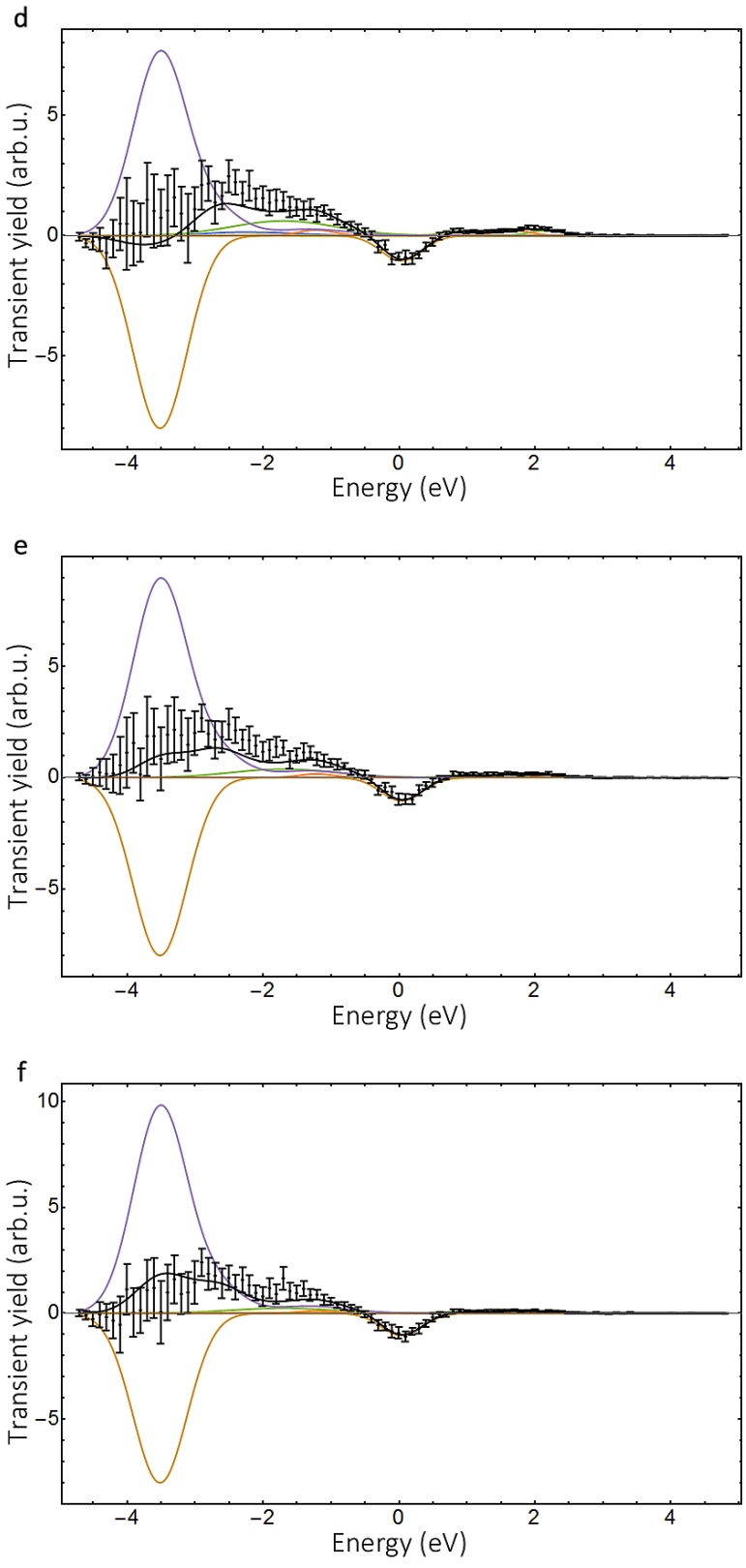

Figure 42.2. Energy distribution of the transient signal at different pump-probe time delays. The signal is integrated within the time-delay intervals between (d) [70, 90] fs, (e) [90, 120] fs, and (f) [120, 150] fs (dots with error bars). The black solid line represents the global fit result. The color lines show the signal decomposition to individual contributions from the ^{1,3}MLCT (yellow), $T_{1,2}$ (green), Q_1^{**} (orange), Q_1^{*} (violet), and S_0 (brown) states as well as the cross-correlation contribution C (blue). Note that the contribution from the S_0 state is of negative value due to the depletion of the ground state.

5.2.8 Comparison with theoretical data

In order to facilitate the interpretation of the experimental results, the theoretical calculations performed by the group of Prof. Dr. Kühn from the University of Rostock were used. The photoelectron spectra were calculated for an isolated molecule of $[Fe(bpy)_3]^{2+}$.

Using the strong orthogonality approximation for the basis set of wave functions, $\langle \psi^{\mathrm{el}} | \phi_l^k \rangle = 0,\ k = (1, \dots, \mathrm{N})$, where ψ^{el} and ϕ_l^k are the wave functions of the photoelectron in the final continuum state and of the bound orbitals, respectively, the ionization intensities can be represented by

$$f_{\mathrm{FI}} \propto \left| \langle \Psi^{\mathrm{el}} | \hat{d} | \Phi_{\mathrm{FI}} \rangle \right|^2 , \tag{51}$$

where

$$\Phi_{\mathrm{FI}} = \sqrt{\mathrm{N}} \int \Psi_{\mathrm{F}}^{\mathrm{N}-1}(x_1, \dots, x_{\mathrm{N}-1})^* \times \Psi_{\mathrm{I}}^{\mathrm{N}}(x_1, \dots, x_{\mathrm{N}}) dx_1 \dots dx_{\mathrm{N}-1} \tag{52}$$

is the Dyson orbital for the transition between the initial N-electron state $\Psi_{\mathrm{I}}^{\mathrm{N}}$ and the final $\mathrm{N} - 1$ electron state $\Psi_{\mathrm{F}}^{\mathrm{N}-1}$, and $\hat{d}$ is the dipole operator. The final state of the photoelectron can be represented by a plane wave expanded in terms of spherical waves [188]:

$$\psi^{\mathrm{el}}(\mathbf{r}) = \sum_{l=0}^{\infty} \sum_{m=-l}^{l} i^l \sqrt{\frac{2}{\pi}}\, j_l(\mathbf{k} \cdot \mathbf{r})\, Y_{l,m}(\mathbf{r})\, Y_{l,m}^*(\mathbf{k}) , \tag{53}$$

where $j_l(\mathbf{k} \cdot \mathbf{r})$ are spherical Bessel functions, l and m are the angular momentum quantum numbers of the outgoing electron, and $Y_{l,m}(\mathbf{r})$, $Y_{l,m}^*(\mathbf{k})$ are the spherical harmonics in the position and the momentum space, respectively. The calculations gave the theoretically simulated spectra for the singlet, triplet and both vibrationally hot and adiabatically cooled quintet states. In Figure 43 the photoelectron spectrum recorded at negative time delay by applying a wide angle mode is compared with the results of theoretical calculations. Negative time delay represents the case, where the probe pulse reaches the sample before the pump pulse and one can consider the spectrum as a steady-state spectrum. The theory predicts a strong signal from Fe 3d(t_{2g}) orbitals, which was

also observed in the experiment. The 3d(t_{2g}) orbitals demonstrate a small splitting of ~0.1 eV, which means that one of the three orbitals is lying energetically higher than the other two. This small splitting originates from the slightly distorted octahedral symmetry of the complex. The reduction of symmetry is caused by the structure of the bipyridine ligands, which consists of two pyridine molecules bound with each other. At the same time, each of six pyridine molecules is bound with the Fe(II) ion. Though the octahedral symmetry group O_h is commonly used in the literature in order to simplify the presentation of the structure, which leads to the threefold degeneracy, the actual point symmetry group of the $[Fe(bpy)_3]^{2+}$ is D_3, where the triple degeneracy is impossible. The contribution of the ligand orbitals to the photoemission spectrum is predicted to lie on the energy scale below -3 eV. As mentioned before, in the experiment this region is covered by the strong signal arising from ionization of the $1b_1$ liquid water orbital.

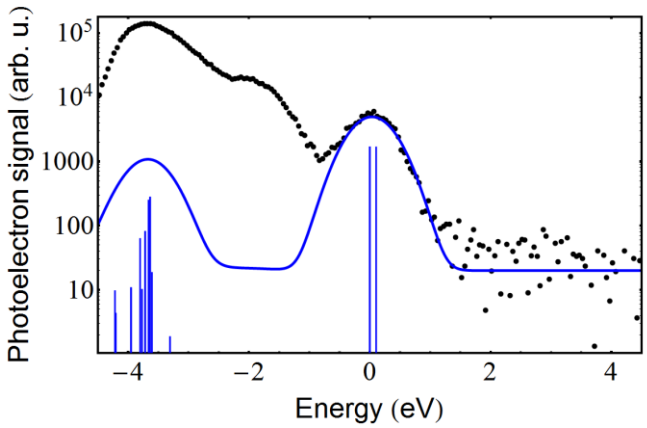

Figure 43. Comparison of the photoemission spectrum of the S_0 ground state of $[Fe(bpy)_3]^{2+}$ recorded at the negative time delays (black dots) with results of theoretical calculations (blue curve). To account for the finite bandwidth of states and for the experimental energy resolution, the calculated stick spectra (blue vertical lines) are broadened by convolution with a Gaussian profile of 0.8 eV width (FWHM).

The decision about which of the two extended models better reproduce the electron dynamic of the SCO process in $[Fe(bpy)_3]^{2+}$(aq), was achived qualitatively assessing and comparing the results obtained from the global fit and from the theoretical calculation. The emission spectra of the Q_1^{**} and $T_{1,2}$ states, inferred from the fit to the model of parallel relaxation, are compared in Figure 44(a) and (b) with the corresponding spectra predicted by the theory (the S_0 emission spectrum was subtracted for consistency with the transient signal plot). One can see that the theory qualitatively reproduces the spectral band structure originating from a superposition of ionization channels leading to the

formation of $[Fe(bpy)_3]^{3+}$ with different electronic configurations and multiplicities. One should note that the theoretical method can contain possible systematic errors, for example, due to the incomplete account for dynamic correlations, which can result in energy shifts of the photoelectron features of the order of 0.5 eV [189, 190]. Thus, results presented in Figure 44(a) and (b) demonstrate a reasonable compromise between the fit stability and the accuracy of the reference theoretical data. Considering the fit results from the cascaded relaxation model, they are compared with the corresponding predictions by theory in panels (c) and (d) of Figure 44, where the emission spectra of T_1 and T_2 states are presented (again, the spectrum of S_0 is subtracted for consistency). This comparison demonstrated that the T_2 spectrum can be reasonably reproduced by theory. However, for the T_1, there is a large discrepancy at ca. -4 eV. In this energy region the global fit routine calculates positive transient yield, whereas negative transient yield is expected due to depletion of the ground state. This gives us grounds to conclude that the parallel relaxation model best describes the data.

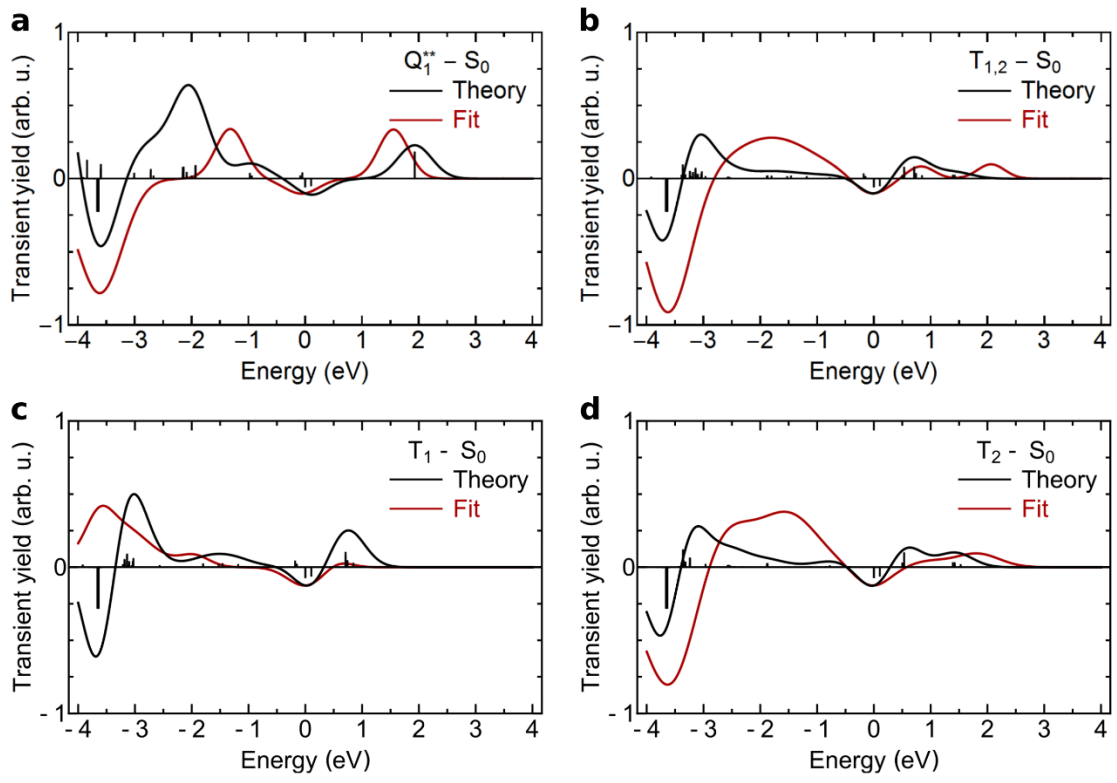

Figure 44. (a, b) Comparison of the photoemission spectra of the Q_1^{**} (a) and $T_{1,2}$ (b) states obtained from the global fit to the experimental results for the parallel model with the spectra predicted by theory. (c, d) Comparison of global fit results for the cascaded model and the theory. Photoemission spectra of the triplet T_1 (c) and T_2 (d) states, considered in the cascaded model are shown. To account for the finite bandwidth of states and for the experimental energy resolution, the calculated stick spectra (vertical lines) are

broadened by convolution with a Gaussian profile of 0.7 eV width. The S_0 emission spectrum is subtracted for the sake of consistency with the transient spectra.

5.2.9 Wave packet dynamics in the quintet state

The application of the XUV laser harmonics to ultrafast PES studies of molecular wavepacket dynamics was successfully demonstrated by Fushitani and Hishikawa [191] in an experiment with samples in gas phase. For a given population of a transient state, the periodic nuclear motion leads to modulations in the XUV emission yield due to the periodic changes in the Franck-Condon conditions of the ionization transition. In the present experiment, the signal attributed to ionization from the quintet state appears to exhibit oscillations which one may be distinguished despite a low signal-to-noise ratio.

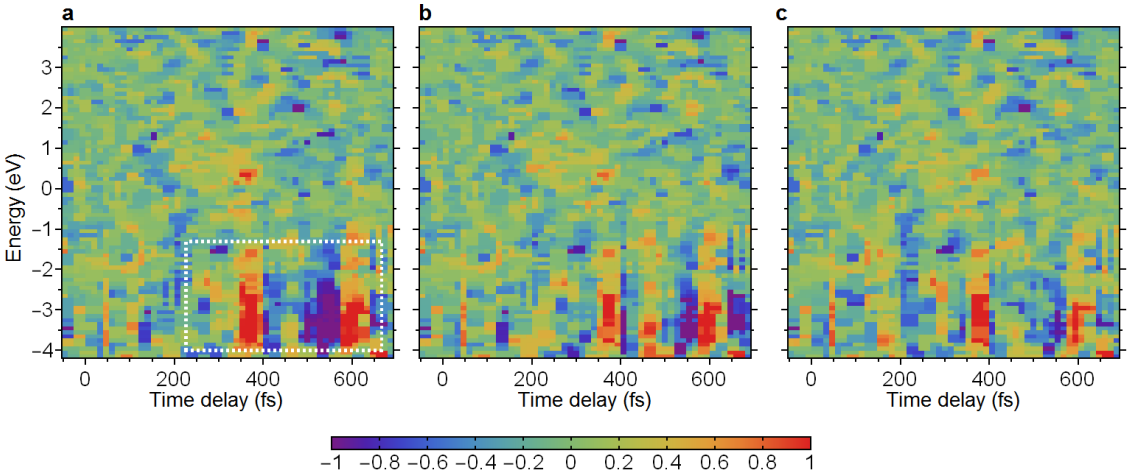

Figure 45. Residuals for the best fit by models allowing for the wave packet dynamics in the Q_1^* state. The difference between the measured transient signal and the global fit results is shown for the models of parallel relaxation: without taking the wave packet oscillations into account (a), allowing for one oscillation mode (b), and for two modes (c). The domain where the extended models improve significantly the fit to the experimental data is marked in panel (a) by the white rectangle.

To account for these oscillations in the probe step, the transient population of the quintet state $[Q_1^*](t)$ was empirically convoluted as

$$[Q_1^*]^*(t) = \int_{-\infty}^{+\infty} \exp\left(-\frac{(t-t')^2}{\tau_{\text{probe}}^2}\right) \times \left(1 + \sum_j a_j\big(1 + \cos\big(\omega_j(t-t') + \varphi_j\big)\big)\right)[Q_1^*](t')\mathrm{d}t' , \tag{54}$$

where j is the index of the oscillation mode of frequency ω_j, amplitude a_j, and phase φ_j. An F-test (s. Equation (41)) was carried out to reveal the significance of adding successively one, two, and three modes in the parallel relaxation model. For the first two modes, the criterion $F_c < F$ was found to be well satisfied: 2.6 < 129.8 (p_n = 13, p_e = 16) and 2.6 < 50.8 (p_n = 16, p_e = 19), respectively. However, an opposite inequality 2.6 > 0.3 (p_n = 19, p_e = 22) was obtained when adding the third mode, indicating that only two modes need to be considered. Figure 45 demonstrates the improvement in reproduction of the experimental data when one and two oscillation modes are taken into account. Their oscillation periods, inferred from the global fit, are 270 ± 20 and 130 ± 10 fs. Figure 46 highlights these oscillations in the population dynamics of the quintet state in the integrated transient signal over the corresponding energy range between −4 and −2.5 eV as a function of the time delay. These oscillations appear immediately after the pump and are analogous to the oscillations reported in previous studies [71, 72, 98], where they had been assigned to impulsively excited vibrational spectator modes. A detailed study of the wave packet dynamics was not in the focus of the present work. Nevertheless, the present results provide a good motivation for the future experiments, employing HHG, to study the ultrafast nuclear wavepacket dynamics in liquids.

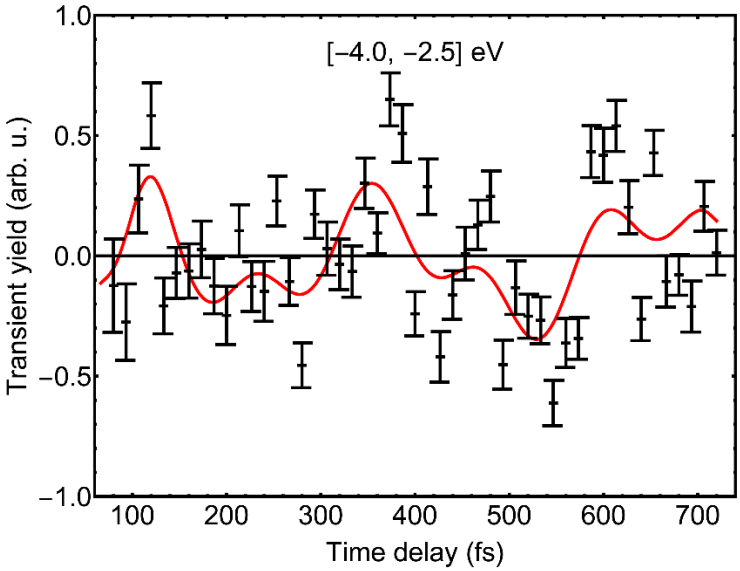

Figure 46. Oscillation in the transient signal from the metastable quintet state Q_1^*. The vertical axis displays the difference between the results of experiment and the global fit (presented in Section 5.2.7), normalized to the transient population of Q_1^* obtained from the fit. Note that the wave packet dynamics are disregarded in the kinetic model. The signal was integrated over the energy interval between −4 and −2.5 eV encompassing the emission band of Q_1^*. The red solid line shows the difference in the fit results when two oscillation modes are allowed for in the model. The oscillation periods of 270 ± 20 fs and 130 ± 10 fs were obtained from the global fit.

5.3 Transient spectrum on a nanosecond time scale

The back relaxation of the electron population to the ground S_0 state was measured by scanning the pump-probe time delay over 1.2 ns with a delay increment of 6.7 ps. The single scan on the nanosecond time scale requires more cumulative data acquisition time than the measurements on the short time scale presented above. The larger increment size was chosen in order to keep the same stable experimental conditions in the interaction region during the scan as it was done in other measurements. With the acquisition time of 10 s per delay stage position the total scanning time was ~35 minutes. This time was sufficient to run the experiment without interruption for the refilling of the cryogenic trap, which could lead to the instability of the pressure in the experimental chamber and, thus, could influence the results. An energy flux of 110 W/cm^2 of the optical pump was applied in this measurement.

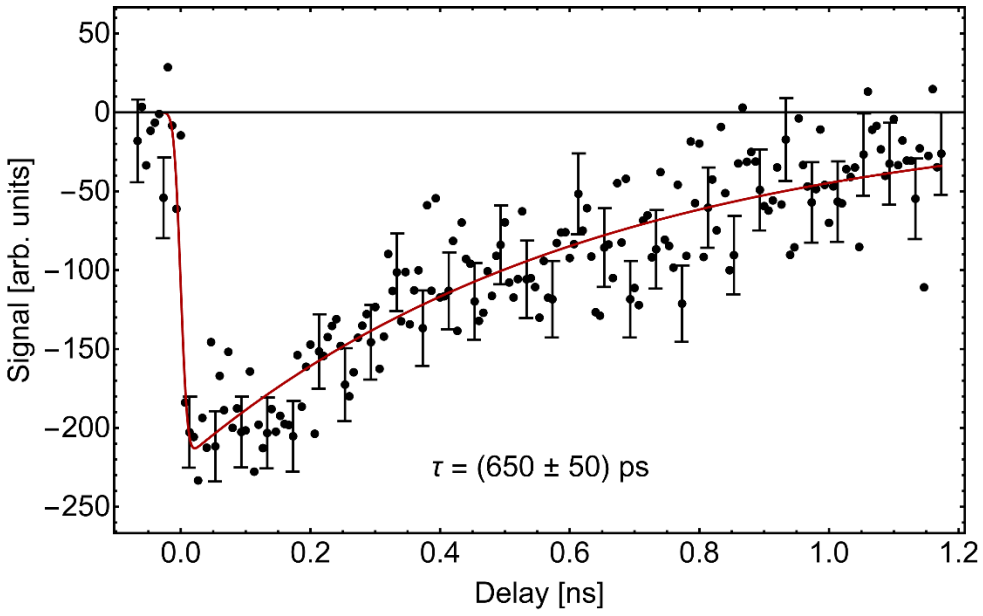

Figure 47. Depletion of the ground state as a function of the time delay. The vertical scale represents the background-subtracted signal, integrated over the emission band of the Fe 3d(t_{2g}) orbitals. The red curve shows results of a fit where the initial depletion of the ground state by the pump beam and its re-population from the Q_1^* state during the photocycle are considered (see Equation (55)). The re-population is described by an exponential function with the fitted time constant of 650 ± 50 ps.

The integrated and background-subtracted photoelectron yield from the Fe 3d(t_{2g}) orbitals is shown in the Figure 47. The relaxation of the negative signal unambiguously demonstrates an exponential character. In order to determine the time constant for the

relaxation, a fit routine was carried out. Considering that the relaxation time τ is much (orders of magnitude) longer than the laser pulse duration as well as the time scale of the SCO dynamics, the relaxation process can be described with the following function, which was used as the fit function in the data analysis:

$$R(t) = -D \cdot \mathrm{erf}\frac{t - t_0}{\tau_l} \cdot \exp\left(-\frac{t - t_0}{\tau}\right), \tag{55}$$

where D is the depletion amplitude, the error function describes the depopulation of the Fe 3d(t_{2g}) orbitals due to the photoexcitation by the laser pulse with the pulse duration τ_l, and the exponential function describes the exponential recovery of the Fe 3d(t_{2g}) orbitals of the ground state with the time constant τ. Since the time width of the cross-correlation signal is very short compared to the relaxation time of the ground state of $[Fe(bpy)_3]^{2+}$, the cross-correlation signal was not considered in the fit routine. Nevertheless, the starting position of the delay stage was chosen in the experiment so that during the scan one spectrum is recorded directly at the center of the Gaussian profile of the cross-correlation. This spectrum gives rise to a single positive data point in the integrated photoelectron yield, appearing at 0 ns on the time-delay scale. This data point served only to confirm the zero time delay position and was removed from the data set in order to simplify the fit routine. The fit results presented in the Figure 47 show an exponential relaxation into the S_0 state with a time constant of (650 ± 50) ps. This result is in a good agreement with the previously reported value from the diverse studies [70, 71, 74, 78, 98].

5.4 Intensity dependency study

The depletion of the S_0 ground-state population of $[Fe(bpy)_3]^{2+}$ was measured as a function of the energy flux of the optical pump beam in the range between 15 and 130 W/cm^2. This measurement was performed in order to exclude the contribution of the multiphoton processes in the time-resolved spectra, such as multiphoton ionization or excitation of the other charge-transfer states of $[Fe(bpy)_3]^{2+}$ by absorbing more than one photon of the pump beam. For example, the absorption of two photons of the pump beam with the wavelength of 530 nm can excite the band of ligand-centered transition in the UV region. Three photons of the pump beam would lead to ionization of the Fe 3d(t_{2g}) orbitals, according to the binding energy of 6.8 eV of these orbitals, as measured in the above presented steady-state experiment.

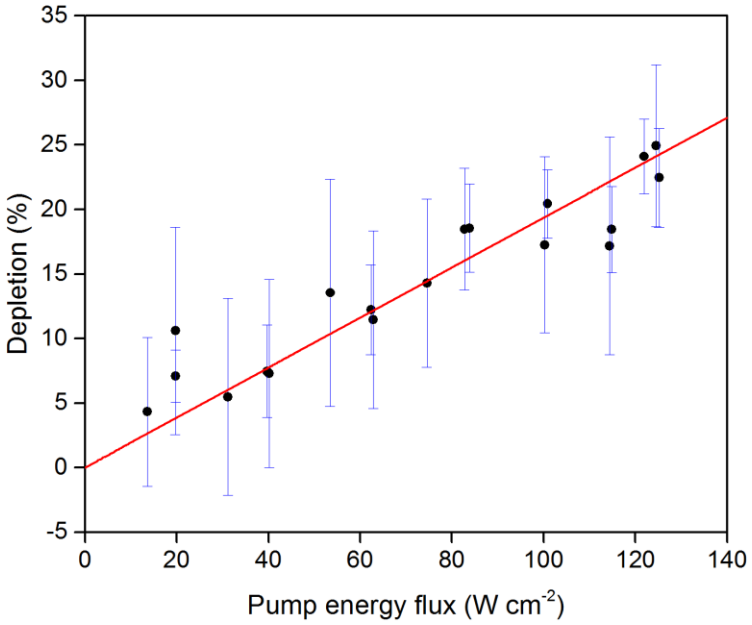

Figure 48. Measured depletion of the ionization yield from Fe 3d(t_{2g}) orbitals of the ground state of $[Fe(bpy)_3]^{2+}$ as a function of the pump energy flux. The red line represents the linear fit to the measured data.

The depletion of the S_0 population is represented by the depletion coefficient of the 3d(t_{2g}) peak in the pump-probe spectra (the coefficient D in Equation (55)). This depletion coefficient D was calculated directly from the measured data as

$$D = \frac{Y_0 - Y}{Y_0}, \tag{56}$$

where Y_0 and Y represent photoelectron yields from the Fe 3d(t_{2g}) orbital at a negative and small positive time delays, respectively. In the case of significant presence of multiphoton processes in the experiment, a nonlinear character of the pump intensity dependency of the photoexcitation from the S_0 ground-state of $[Fe(bpy)_3]^{2+}$ is expected. However, the probability of the one-photon excitation transition can be represented by a linear dependency on the pump beam intensity [133]:

$$W = \sigma \frac{I}{E_{\mathrm{ph}}} \tau, \tag{57}$$

where σ is the photoabsorption cross section, I is the intensity of the pump laser beam, E_{ph} is the photon energy of the pump laser beam, and τ is its pulse duration. This immediately implies that the depletion coefficient should also be linearly dependent on I. The present measurement reveals the linear dependency of the depletion on the pump

beam intensity (see Figure 48). This fact, combined with the observation of the strong transient signal at 2.3 eV within a few tens of femtoseconds after the excitation, suggests that the ^{1}MLCT state is excited in a one-photon transition.

5.5 Conclusions

Concluding this chapter, ultrafast PES was successfully applied to reveal the mechanism of the photoinduced SCO in an aqueous solution of $[Fe(bpy)_3]^{2+}$. The presented experimental setup, based on a table-top HHG setup and a TOF spectroscopy technique, enabled us to probe the electron density distribution in the entire valence shell of both water and $[Fe(bpy)_3]^{2+}$. The results of the steady-state measurements of the XUV photoemission spectra of water are in a very good agreement with the results known from the earlier PES studies. The photoemission spectrum of the solvated $[Fe(bpy)_3]^{2+}$ exhibits a strong well-separated peak associated with the ionization of the $3d(t_{2g})$ orbitals in the ground LS state. The center of this peak was found to lie at a 6.8 eV binding energy, and this value was used as the origin of the relative energy scale to track the electron dynamics of the light-induced SCO process.

The advanced data analysis, including the global fit and the statistical *F*-test, was developed and applied to interpret the background-subtracted transient signal in terms of a kinetic model. Different kinetic models were considered to describe the SCO mechanism, observed in the transient signal. It was found that the statistical method (*F*-test) alone is not sufficient to make a definitive choice between the kinetic models. Therefore, the final consideration was made based on the results of theoretical calculations. The parallel SCO model, where both the direct $^{1,3}\mathrm{MLCT}\rightarrow Q_1^{**}$ and sequential $^{1,3}\mathrm{MLCT}\rightarrow T_{1,2}\rightarrow Q_1^{*}$ transitions are involved, yielded the best agreement with the theoretical predictions. The global fit procedure based on the parallel model delivered the transition time constants, which are summarized in the Table 3.

The findings are partly consistent with the results presented by Chergui and Augböck [72] and by Zhang *et al.* [79], while both research groups proposed only direct or only sequential kinetic models, respectively. Thus, the application of the novel methodology based on ultrafast PES brings a new insight to the SCO mechanism and provides a complete interpretation of this phenomenon.

Transition	^{1,3}MLCT→$T_{1,2}$	^{1,3}MLCT→Q_1**	$T_{1,2}$→Q_1*	Q_1**→Q_1*	Q_1→S_0
Lifetime (Experiment)	20 ± 20 fs	90 ± 25 fs	70 ± 20 fs	35 ± 20 fs	650 ± 50 ps
Lifetime (Literature)	150 ± 50 fs [79]	< 50 fs [72]	70 ± 30 fs [79]	-	665 ± 35 ps [70]

Table 3. Time constants obtained in this work in comparison with the time constants presented in the literature by different research groups.

It is worth resolving the issue of the unity quantum yield of the low-to-high spin transition, which was discussed in Ref. [72]. Taking into account the branching ratio of 4.5:1 between channels II and I and using the predicted value of 1:13 for the branching ratio between the deactivation $T_{1,2} \rightarrow S_0$ and the SCO $T_{1,2} \rightarrow Q_1^*$ channels (see Table 7 in Ref. [82]), the quantum yield was found to be approximately 94%. This value is, indeed, close to unity, and it is a complicated task to detect the repopulation of 6% of the ground state in the experiment.

The time-resolved measurements on the nanosecond time scale delivered the time constant for the recovery of the ground state S_0 of $[Fe(bpy)_3]^{2+}$ (s. Table 3) in an excellent agreement with the results obtained earlier by application of absorption spectroscopy methods [70, 71, 74, 78, 98].

6 Experiments with other iron complexes

The methodology presented in this work, was also successfully applied in a number of other studies on the light-induced relaxation dynamics in iron coordination complexes in aqueous solution, such as ferricyanide, $[Fe(CN)_6]^{3-}$, and nitroprusside, $[Fe(CN)_5NO]^{2-}$. The results of those studies are presented in detail in Refs. [192] and [193], respectively. In this chapter, preliminary results on the photodissociation dynamics in iron pentacarbonyl, $Fe(CO)_5$, obtained with the use of the TRPES, are discussed.

$Fe(CO)_5$ belongs to a large group of metal carbonyls, which are famous for their catalytic properties. $Fe(CO)_5$ can be applied in the synthesis of the metal-carbon nanoparticles, which can be used to obtain new functional materials for electrical engineering or for catalytic synthesis [194]. The complex was extensively studied by application of time-resolved methods in the gas phase [195-200] and in solution [201-204]. Photoexcitation of $Fe(CO)_5$ with the UV light in the gas phase leads to fragmentation of the complex, whereas the iron atom can lose from one CO ligand up to all five CO ligands [196, 197]. The first Fe-CO bond cleavage was found to occur on the time scale of <100 fs [198]. Unlike the fragmentation dynamics in the gas phase, in solution only one CO ligand can be removed from the complex following the photoexcitation. However, the recent study by Wernet and co-workers [204] has revealed interesting dynamics in $Fe(CO)_5$ solvated in ethanol, which was investigated with the use of time-resolved resonant inelastic X-ray scattering employing 266 nm laser pulse as a pump beam and free-electron laser as a source for the probe beam. The experiment, performed with the time resolution of 300 fs, revealed a number of different reaction pathways. They involve relaxation of the excited singlet state of $Fe(CO)_4$ to the triplet $Fe(CO)_4$ state due to IC/ISC and formation of the mono-substituted complex $Fe(CO)_4$-EtOH with the solvent (ethanol) on the time scale of 200-300 fs.

In the present work, the third harmonic of the fundamental 800 nm beam of the wavelength of 267 nm was used as a pump pulse. It was generated in the THG setup, described in Section 4.1.4, which replaced the OPA in the pump-probe configuration used for the experiments with $[Fe(bpy)_3]^{2+}$. As discussed in the literature [198, 204], photoexcitation with 267 nm laser light initiates a MLCT transition, which relaxes to the MC excited state. Figure 49(a) shows the absorption spectrum of 100 mM solution of

$Fe(CO)_5$ in ethanol, obtained in the course of this experiment. The spectrum is consistent with the results known from the literature [205]. Two prominent absorption bands in the region 200 – 350 nm are associated with the MLCT transitions. In contrast to $[Fe(bpy)_3]^{2+}$, direct MC transitions in $Fe(CO)_5$ are also allowed because of the different symmetry. However, the MC bands, which appear in the spectrum at wavelengths higher than 350 nm, exhibit considerably lower absorption cross section than MLCT bands. Similar to other d^8-systems, the trigonal bipyramidal (D_{3h}) geometry is the most stable one for $Fe(CO)_5$.

Since $Fe(CO)_5$ is highly toxic and flammable, the experimental setup and procedure presented in Section 4.5 was optimized according to the safety directives. The sample was handled in the glove-box purged with N_2. The liquid microjet setup was extended with a tubing loop filled with sample and a HPLC pump for the delivery of the sample to the interaction region. Both, the loop and the pump were placed in the glove-box. The syringe pump filled with ethanol was included in the system with the possibility to switch between the sample and ethanol. This allowed to refill the tubing loop with the sample, while the system was running with ethanol, and, thus, to avoid venting of the experimental chamber. Especially for this experiment, a compact cryogenic trap was constructed in order to facilitate the passage of the filled trap through the airlock of the glove-box, where the sample waste could be handled safely.

The steady-state spectra of the pure solvent and solution are shown in Figure 49 (see panels (b) and (c)). The spectrum presented in Figure 49(b) was recorded in the drift mode of the electron spectrometer, and it shows a rich band structure of the valence shell of ethanol. The results presented in Figure 49(c) were recorded in the wide angle mode. They demonstrate contribution of the ionization yield of $Fe(CO)_5$ to the steady-state XUV spectrum of the solution. One can see that the photoemission spectrum of $Fe(CO)_5$ lies on the slope of the emission band of ethanol originating from ionization of its highest molecular orbital. The contribution from $Fe(CO)_5$ is largely hidden in the spectrum because of the dominant ionization yield of ethanol.

Figure 49(d) represents the cross-correlation measurement with 267 nm pump and XUV probe pulses, obtained with the pure ethanol sample. The Gaussian fit of the integrated electron yield in the kinetic energy region of the first side band, recorded as a function of time delay, exhibits the width of 180 fs (FWHM). This width was achieved after the optimization procedure of the laser compressor, as applied in the $[Fe(bpy)_3]^{2+}$ experiment. The larger width of the cross-correlation function originates from the

stretching of the 267 nm pulse due to dispersion in the optical components. This effect, which was tolerable for the visible laser pulses used in the previous experiments, is considerably more crucial for the shorter wavelength. In order to minimize the dispersion and to improve the time resolution of the experiment, it is suggestible to exchange the lenses with the concave mirrors in the future studies.

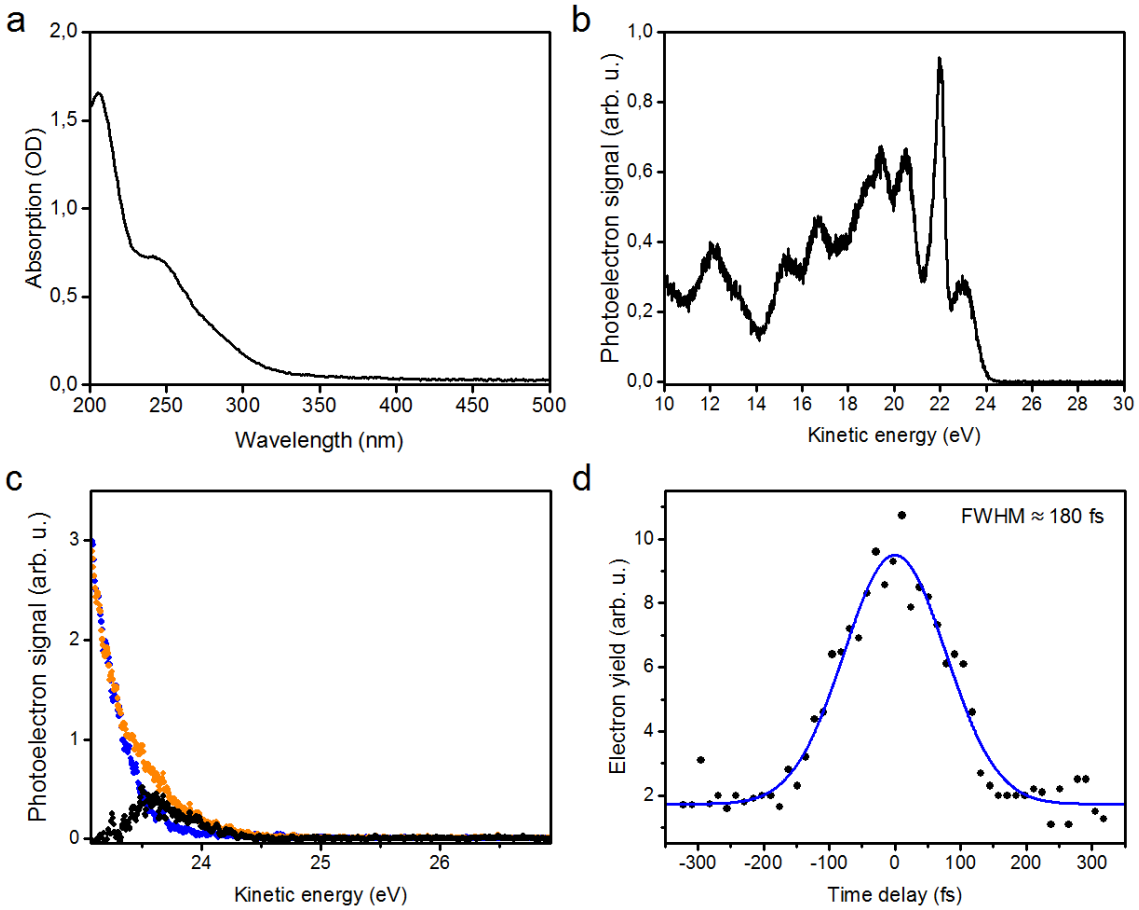

Figure 49. (a) Absorption spectrum of 100 mM solution of $Fe(CO)_5$ in ethanol recorded with the use of a commercial spectrophotometer JENWAY 7315. (b) Steady-state photoelectron spectrum of ethanol obtained with the use of XUV light while operating TOF-spectrometer in drift mode. (c) Steady-state photoelectron spectra of pure ethanol (blue dots) and 0.5 M solution of $Fe(CO)_5$ in ethanol (orange dots) obtained in the WAM. Black dots show results of subtraction of the signal recorded with ethanol from the signal recorded with $Fe(CO)_5$ solution. It originates from the ionization of the 3d orbitals of iron atoms of $Fe(CO)_5$ by the XUV light. (d) Cross-correlation signal of ethanol recorded by applying 267 nm pump and XUV probe pulses. The signal represents photoemission yield integrated over the electron kinetic energy range above 25 eV. The blue curve represents a Gaussian fit of the recorded data, yielding the cross-correlation width of 180 fs (FWHM).

In the main part of this experiment, several series of time-resolved spectra were recorded in the energy range between 23 eV and 30 eV. This range includes the

appearance of the emission band of $Fe(CO)_5$ in the ground state, which has a maximum at ~23.6 eV (see Figure 49(c)), and it is sufficiently broad to reveal a transient signal within one pump photon energy above this band. The scans were performed in the range of time delays extending over 600 fs and 3 ps. The results of the later measurement are demonstrated in Figure 50. A 0.5 M $Fe(CO)_5$ solution in ethanol was used as a sample. The results exhibit the cross-correlation signal, which arises from LAPE of ethanol, and an energy shift of the liquid ethanol edge to lower kinetic energies. The latter is a consequence of the space-charge effect. The transient signal that could be assigned to the photoinduced electron dynamics of $Fe(CO)_5$ is not apparent in the data obtained in this experiment. This can be due to the following reasons:

1. The life times of the MLCT transitions initiated by pump beam are too short in comparison with the width of the cross-correlation signal of ~180 fs.
2. In this experiment, only the kinetic energy range above the highest-lying emission band from liquid ethanol was considered. The transient signal from $Fe(CO)_5$ can be buried under the signal arising due to photoionization of ethanol at the kinetic energies below 23 eV.

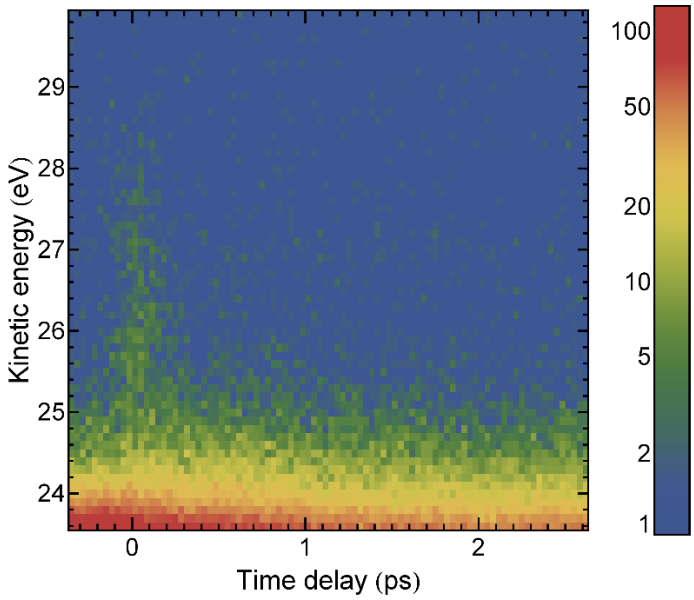

Figure 50. Electron yield as a function of the kinetic energy and the time delay obtained by photoionization of 0.5 M solution of $Fe(CO)_5$ in ethanol.

The later point leads to a technical challenge, since the measurements with the use of the WAM operation mode in the energy region below 23 eV would saturate the detection electronics of the TOF spectrometer with the electrons produced by ionization

of ethanol. A possible solution could be to apply a different mode of the spectrometer operation with a lower collection efficiency or/and to reduce the intensity of the XUV beam. Also, the approach to handle the energy shift caused by the space-charge effect should be reconsidered for this experiment. Since the ionization potential of ethanol lies ~2 eV lower than the ionization potential of water [157] (see also Figure 49(b)), the signal from the 3d orbitals of the iron atom overlaps with the highest occupied orbital of ethanol and cannot be used as a reference, as it was the case in the experiments with aqueous solutions of $[Fe(bpy)_3]^{2+}$ [176], $[Fe(CN)_6]^{4-}$ [133], and $[Fe(CN)_6]^{3-}$ [192].

Nevertheless, this experiment was the first step in the application of the developed methodology, which was successfully applied in the present work to study SCO dynamics in $[Fe(bpy)_3]^{2+}$, to reveal the electron dynamics accompanying the photo-induced dissociation of $Fe(CO)_5$. Despite extensive studies in the past, this photochemical phenomenon is still not unambiguously clarified and has promising perspectives for future research by means of TRPES.

7 Summary

In this work, ultrafast spin crossover (SCO) dynamics was studied in an aqueous solution of $[Fe(bpy)_3]^{2+}$ by means of time-resolved XUV photoemission spectroscopy (PES). For this challenging task, the novel methodology was developed in order to facilitate the experimental procedure and the data analysis. The table-top high harmonic generation (HHG) setup was employed as a source for the ultrashort XUV probe pulses in the pump-probe configuration. The special feature of the HHG setup was the application of the reflection zone-plate for the monochromatizating of the XUV light. This technique facilitated the selection of a single XUV harmonic with a ~45 fs pulse duration and a photon energy and intensity suitable to reveal the electron dynamics of solvated $[Fe(bpy)_3]^{2+}$ with a time resolution of 60 fs. The influence of the space-charge effect and the laser-assisted photoelectric effect (LAPE) to the time-resolved XUV PES were considered in this work. These two accompanying effects are very important issues, and an understanding of their effects and dependencies is crucial for both data acquisition and data analysis. Therefore, they were carefully taken into account in the methodology proposed in the present work.

To maintain stable experimental conditions, crucial for PES measurements with liquid samples, the combination of the liquid microjet technique, a cryogenic trap, and an appropriate experimental procedure was developed and successfully applied.

The steady-state PES spectrum of valence orbitals of water obtained with the use of the table-top HHG setup was demonstrated to be in excellent agreement with the results from previous studies, where synchrotron radiation was employed as a light source instead. The LAPE was found to be beneficial for the characterization of the temporal characteristics of XUV and optical laser pulses and for the precise determination of the zero time delay in the time-resolved experiments. The pump-probe setup configuration combined with the time-of-flight (TOF) spectrometer technique facilitated the tracking of the evolution of the valence orbital population in $[Fe(bpy)_3]^{2+}$, induced by the 530 nm laser pulse, on the femtosecond time-scale.

The kinetic model, which describes the SCO process in $[Fe(bpy)_3]^{2+}$, was chosen with the support of the theoretical calculations performed by the research group of Prof. Dr. Oliver Kühn from Rostock University. Unlike the description of the SCO process reported previously in the literature, the kinetic model proposed in this work incorporates

both the direct and the cascaded relaxation channels which occur simultaneously. The global fit results obtained with the use of this model of parallel relaxation channels demonstrate a very good agreement with the experimental data. The branching ratio between the channels was found to be $4.5^{+4.8}_{-1.5}$, indicating that the population of intermediate triplet states dominates the relaxation dynamics. However, the results of this study also support the possibility of a direct transition from the excited ^{1,3}MLCT states to the quintet state with a time constant smaller than previously reported [75, 79], thus, partially supporting the conclusion by Auböck and Chergui [72]. The recovery time of the ground low-spin state of $[Fe(bpy)_3]^{2+}$ was found to be 650 ± 50 ps, as inferred from the measurements on the nanosecond scale of time delays. This result is in excellent agreement with the results from earlier studies [70, 71, 74, 78, 98]. The time constants of various relaxation transitions involved in the SCO mechanism, obtained from the data analysis, are summarized in Table 3 (see Section 5.5) in comparison with the results from the earlier studies by other research groups.

Summarizing, the present study demonstrates that the sensitivity of previously applied spectroscopies, such as transient absorption and X-ray fluorescence spectroscopy, revealed only one of the possible SCO channels, whereas the ultrafast PES applied here provides insight into the entire electron dynamics and is capable to detect both the direct and the cascaded low-to-high spin transitions. The present tabletop methodology is a robust and convenient tool for detailed characterization of ultrafast electron dynamics with wide applications in photochemistry, photophysics, and photobiology.

Literature

1. Siegbahn, H. and K. Siegbahn, *ESCA applied to liquids.* Journal of Electron Spectroscopy and Related Phenomena, 1973. **2**(3): p. 319-325.

2. Faubel, M., S. Schlemmer, and J.P. Toennies, *A Molecular-Beam Study of the Evaporation of Water from a Liquid Jet.* Zeitschrift Fur Physik D-Atoms Molecules and Clusters, 1988. **10**(2-3): p. 269-277.

3. Neumark, D.M., *Time-resolved photoelectron spectroscopy of molecules and clusters.* Annual Review of Physical Chemistry, 2001. **52**: p. 255-277.

4. Stolow, A., A.E. Bragg, and D.M. Neumark, *Femtosecond time-resolved photoelectron spectroscopy.* Chemical Reviews, 2004. **104**(4): p. 1719-1757.

5. Stolow, A. and J.G. Underwood, *Time-Resolved Photoelectron Spectroscopy of Nonadiabatic Dynamics in Polyatomic Molecules.* Advances in Chemical Physics, Vol 139, 2008. **139**: p. 497-583.

6. Buchner, F., et al., *Time-resolved photoelectron spectroscopy of liquids.* Rev Sci Instrum, 2010. **81**(11): p. 113107.

7. Holmes, R.J., et al., *Blue organic electrophosphorescence using exothermic host–guest energy transfer.* Applied Physics Letters, 2003. **82**(15): p. 2422-2424.

8. Baranoff, E., et al., *Cyclometallated iridium complexes for conversion of light into electricity and electricity into light.* Journal of Organometallic Chemistry, 2009. **694**(17): p. 2661-2670.

9. You, Y. and W. Nam, *Photofunctional triplet excited states of cyclometalated Ir(III) complexes: beyond electroluminescence.* Chemical Society Reviews, 2012. **41**(21): p. 7061-7084.

10. Borgwardt, M., et al., *Injection Kinetics and Electronic Structure at the N719/TiO_2 Interface Studied by Means of Ultrafast XUV Photoemission Spectroscopy.* The Journal of Physical Chemistry C, 2015. **119**(17): p. 9099-9107.

11. Borgwardt, M., et al., *Charge Transfer Dynamics at Dye-Sensitized ZnO and TiO_2 Interfaces Studied by Ultrafast XUV Photoelectron Spectroscopy.* 2016. **6**: p. 24422.

12. Sato, O., *Optically switchable molecular solids: photoinduced spin-crossover, photochromism, and photoinduced magnetization.* Acc Chem Res, 2003. **36**(9): p. 692-700.

13. Létard, J.-F., P. Guionneau, and L. Goux-Capes, *Towards Spin Crossover Applications*, in *Spin Crossover in Transition Metal Compounds III*, P. Gütlich and H.A. Goodwin, Editors. 2004, Springer Berlin Heidelberg: Berlin, Heidelberg. p. 221-249.

14. Gaspar, A.B., et al., *Multifunctionality in spin crossover materials.* Coordination Chemistry Reviews, 2005. **249**(23): p. 2661-2676.

15. Volatron, F., et al., *Spin-Crossover Coordination Nanoparticles.* Inorganic Chemistry, 2008. **47**(15): p. 6584-6586.

16. Bousseksou, A., et al., *Molecular spin crossover phenomenon: recent achievements and prospects.* Chemical Society Reviews, 2011. **40**: p. 3313-3335.

17. Liu, T., et al., *A light-induced spin crossover actuated single-chain magnet.* 2013. **4**: p. 2826.

18. Matsumoto, T., et al., *Programmable spin-state switching in a mixed-valence spin-crossover iron grid.* 2014. **5**: p. 3865.

19. Harvey, J.N., *Spin-forbidden CO ligand recombination in myoglobin.* Faraday Discussions, 2004. **127**(0): p. 165-177.

20. Helbing, J., et al., *Time-Resolved Visible and Infrared Study of the Cyano Complexes of Myoglobin and of Hemoglobin I from Lucina pectinata.* Biophysical Journal, 2004. **87**(3): p. 1881-1891.

21. Ali, M.E., B. Sanyal, and P.M. Oppeneer, *Electronic Structure, Spin-States, and Spin-Crossover Reaction of Heme-Related Fe-Porphyrins: A Theoretical Perspective.* The Journal of Physical Chemistry B, 2012. **116**(20): p. 5849-5859.

22. McCammon, C., et al., *Stable intermediate-spin ferrous iron in lower-mantle perovskite.* Nature Geoscience, 2008. **1**(10): p. 684-687.

23. Antonangeli, D., et al., *Spin Crossover in Ferropericlase at High Pressure: A Seismologically Transparent Transition?* Science, 2011. **331**(6013): p. 64.

24. Cambi, L. and L. Szegö, *Über die magnetische Susceptibilität der komplexen Verbindungen.* Ber. Dtsch. Chem. Ges., 1931. **64**(10): p. 2591-2598.

25. Cambi, L. and L. Malatesta, *Magnetismus und Polymorphie innerer Komplexsalze: Eisensalze der Dithiocarbamidsäuren.* Ber. Dtsch. Chem. Ges., 1937. **33**(20): p. 2024–2054.

26. Figgis, B.N. and M.A. Hitchman, *Ligand field theory and its applications*. Special topics in inorganic chemistry. 2000, New York: Wiley-VCH. 354 pp.

27. *Chemistry. Provided by: OpenStax, located at: http://openstaxcollege.org. Download for free at https://openstaxcollege.org/textbooks/chemistry/get.*

28. Atkins, P.W., et al., *Shriver & Atkins' Inorganic chemistry*. 5th ed. 2010, New York: W.H. Freeman and Company, Oxford University Press. 824 pp.

29. Wagenknecht, P.S. and P.C. Ford, *Metal centered ligand field excited states: Their roles in the design and performance of transition metal based photochemical molecular devices.* Coordination Chemistry Reviews, 2011. **255**: p. 591-616.

30. Montalti, M. and S.L. Murov, *Handbook of photochemistry*. 3rd ed. 2006, Boca Raton: CRC/Taylor & Francis. 664 pp.

31. Gütlich, P., A. Hauser, and H. Spiering, *Thermal and Optical Switching of Iron(II) Complexes.* Angewandte Chemie-International Edition in English, 1994. **33**(20): p. 2024-2054.

32. König, E., *Some Aspects of Chemistry of Bis(2,2'-Dipyridyl) and Bis(1,10-Phenanthroline) Complexes of Iron(II).* Coordination Chemistry Reviews, 1968. **3**(4): p. 471-495.

33. König, E., G. Ritter, and H.A. Goodwin, *Thermally Induced High-Spin ($^5T_2$) ⇌ Low-Spin ($^1A_1$) Transitions in Bis[2-(2-Pyridylamino)-4-(2-Pyridyl)Thiazole]Iron(II) Complexes - a Mössbauer Effect Study.* Chemical Physics Letters, 1976. **44**(1): p. 100-103.

34. Goodwin, H.A., *Spin Transitions in 6-Coordinate Iron(II) Complexes.* Coordination Chemistry Reviews, 1976. **18**(3): p. 293-325.

35. Gütlich, P., *Spin Crossover in Iron(II)-Complexes.* Structure and Bonding, 1981. **44**: p. 83-195.

36. König, E., G. Ritter, and S.K. Kulshreshtha, *The Nature of Spin-State Transitions in Solid Complexes of Iron(II) and the Interpretation of Some Associated Phenomena.* Chemical Reviews, 1985. **85**(3): p. 219-234.

37. Toftlund, H., *Spin Equilibria in Iron(II) Complexes.* Coordination Chemistry Reviews, 1989. **94**: p. 67-108.

38. Gütlich, P. and A. Hauser, *Thermal and Light-Induced Spin Crossover in Iron(II) Complexes.* Coordination Chemistry Reviews, 1990. **97**: p. 1-22.

39. Decurtins, S., et al., *Light-Induced Excited Spin State Trapping in a Transition-Metal Complex - the Hexa-1-Propyltetrazole-Iron (II) Tetrafluoroborate Spin-Crossover System.* Chemical Physics Letters, 1984. **105**(1): p. 1-4.

40. Decurtins, S., et al., *Light-Induced Excited-Spin-State Trapping in Iron(II) Spin-Crossover Systems - Optical Spectroscopic and Magnetic-Susceptibility Study.* Inorganic Chemistry, 1985. **24**(14): p. 2174-2178.

41. Decurtins, S., et al., *New examples of light-induced excited spin state trapping (LIESST) in iron(II) spin-crossover systems.* Journal of the Chemical Society, Chemical Communications, 1985. **7**: p. 430.

42. Hauser, A., *Reversibility of Light-Induced Excited Spin State Trapping in the $Fe(ptz)_6(BF_4)_2$ and the $Zn_{1-x}Fe_x(ptz)_6(BF_4)_2$ Spin-Crossover Systems.* Chemical Physics Letters, 1986. **124**(6): p. 543-548.

43. Herber, R. and L.M. Casson, *Light-Induced Excited-Spin-State Trapping - Evidence from VTFTIR Measurements.* Inorganic Chemistry, 1986. **25**(6): p. 847-852.

44. Herber, R.H., *VTFTIR and Light-Induced Excited Spin State Trapping in $Fe(2,2'\text{-}bpy)_2(SCN)_2$ and Related Spin-Crossover Compounds.* Inorganic Chemistry, 1987. **26**(1): p. 173-178.

45. Poganiuch, P. and P. Gütlich, *Light-Induced Excited-Spin-State Trapping (LIESST) in $[Fe(2\text{-}Y\text{-}Phen)_3]X_2$ Spin-Crossover Compounds.* Inorganic Chemistry, 1987. **26**(3): p. 455-458.

46. Addison, A.W., et al., *New Iron(II) Spin-Crossover Complexes with Heterocyclic Amine-Derived Ligands and STEPS Experiments on Photogenerated Metastable High-Spin States.* Journal of the Chemical Society-Dalton Transactions, 1987(11): p. 2621-2630.

47. Baldenius, K.U., et al., *Light-Induced Excited Spin State Trapping (LIESST) for Fe(II) Complexes - Infrared Studies at ca. 10-298 K.* Journal of Molecular Structure, 1987. **157**(1-3): p. 295-299.

48. Hauser, A., J. Adler, and P. Gütlich, *Light-Induced Excited Spin State Trapping (LIESST) in $[Fe(2\text{-}Mephen)_3]^{2+}$ Embedded in Polymer Matrices.* Chemical Physics Letters, 1988. **152**(6): p. 468-472.

49. Figg, D.C. and R.H. Herber, *Spin Crossover and Light-Induced Excited-Spin-State Trapping in Bis(Thiocyanato)Bis(2,2'-Bi-2-Thiazoline)Iron(II) and Bis(Selenocyanato)Bis(2,2'-Bi-2-Thiazoline)Iron(II).* Inorganic Chemistry, 1990. **29**(11): p. 2170-2173.

50. Letard, J.F., et al., *Critical temperature of the LIESST effect in iron(II) spin crossover compounds.* Chemical Physics Letters, 1999. **313**(1-2): p. 115-120.

51. Hayami, S., et al., *A novel LIESST iron(II) complex exhibiting a high relaxation temperature.* Inorganic Chemistry, 2001. **40**(13): p. 3240-3242.

52. Letard, J.F., *Photomagnetism of iron(II) spin crossover complexes - the T(LIESST) approach.* Journal of Materials Chemistry, 2006. **16**(26): p. 2550-2559.

53. Costa, J.S., et al., *Photomagnetic properties of an iron(II) low-spin complex with an unusually long-lived metastable LIESST state.* Inorganic Chemistry, 2007. **46**(10): p. 4114-4119.

54. Saigo, N., et al., *Direct observation of low-temperature bistability in an iron(III) LIESST compound.* Journal of Inclusion Phenomena and Macrocyclic Chemistry, 2015. **82**(1-2): p. 225-228.

55. Cagle, F.W. and G.F. Smith, *2,2'-Bipyridine Ferrous Complex Ion as Indicator in the Determination of Iron.* Analytical Chemistry, 1947. **19**(6): p. 384-385.

56. Kumar, A., et al., *A $[Fe(bpy)_3]^{2+}$ grafted graphitic carbon nitride hybrid for visible light assisted oxidative coupling of benzylamines under mild reaction conditions.* Green Chemistry, 2016. **18**(8): p. 2514-2521.

57. Dick, S., *Crystal structure of tris(2,2 '-bipyridine)iron(II) bis(hexafluorophosphate), $(C_{10}H_8N_2)_3Fe(PF_6)_2$.* Zeitschrift Fur Kristallographie-New Crystal Structures, 1998. **213**(2): p. 356-356.

58. Lawson Daku, L.M., et al., *Assessment of Density Functionals for the High-Spin/Low-Spin Energy Difference in the Low-Spin Iron(II) Tris(2,2'-bipyridine) Complex.* ChemPhysChem, 2005. **6**: p. 1393-1410.

59. Hanwell, M.D., et al., *Avogadro: an advanced semantic chemical editor, visualization, and analysis platform.* Journal of Cheminformatics, 2012. **4**:17.

60. Neese, F., *The ORCA program system.* Wiley Interdisciplinary Reviews-Computational Molecular Science, 2012. **2**(1): p. 73-78.

61. Kober, E.M. and T.J. Meyer, *Concerning the absorption spectra of the ions $M(bpy)_3^{2+}$ (M = Fe, Ru, Os; bpy = 2,2'-bipyridine).* Inorganic Chemistry, 1982. **21**: p. 3967-3977.

62. Berger, R.M. and D.R. McMillin, *Ultraviolet and visible resonance raman spectroscopy of tris-(2,2'-bipyridyl)iron(II): intensity considerations and band assignments.* Inorganica Chimica Acta, 1990. **177**: p. 65-69.

63. de Graaf, C. and C. Sousa, *Study of the Light-Induced Spin Crossover Process of the $[Fe^{II}(bpy)_3]^{2+}$ Complex.* Chemistry – A European Journal, 2010. **16**: p. 4550-4556.

64. Ceulemans, A. and L.G. Vanquickenborne, *On the Charge-Transfer Spectra of Iron(II)-Tris(2,2'-Bipyridyl) and Ruthenium(II)-Tris(2,2'-Bipyridyl) Complexes.* Journal of the American Chemical Society, 1981. **103**(9): p. 2238-2241.

65. Kirk, A.D., et al., *Picosecond Flash-Photolysis and Spectroscopy - Transition-Metal Coordination-Compounds.* Chemical Physics Letters, 1976. **37**(2): p. 199-203.

66. Creutz, C., et al., *Lifetimes, spectra, and quenching of the excited states of polypyridine complexes of iron(II), ruthenium(II), and osmium(II).* Journal of the American Chemical Society, 1980. **102**: p. 1309-1319.

67. Bergkamp, M.A., et al., *Temperature-Dependence of the Lifetimes of the Ligand-Field States of Tris(1,10-Phenanthroline)Iron(II).* Chemical Physics Letters, 1981. **81**(1): p. 147-150.

68. Hauser, A., *Excited-State Lifetimes of $[Fe(Bipy)_3]^{2+}$ and $[Fe(Phen)_3]^{2+}$.* Chemical Physics Letters, 1990. **173**(5-6): p. 507-512.

69. McCusker, J.K., et al., *Subpicosecond $^1MLCT \rightarrow {}^5T_2$ intersystem crossing of low-spin polypyridyl ferrous complexes.* Journal of the American Chemical Society, 1993. **115**: p. 298-307.

70. Gawelda, W., et al., *Ultrafast Nonadiabatic Dynamics of $[Fe^{II}(bpy)_3]^{2+}$ in Solution.* Journal of the American Chemical Society, 2007. **129**: p. 8199-8206.

71. Consani, C., et al., *Vibrational coherences and relaxation in the high-spin state of aqueous $[Fe^{II}(bpy)_3]^{2+}$.* Angew Chem Int Ed Engl, 2009. **48**(39): p. 7184-7187.

72. Auböck, G. and M. Chergui, *Sub-50-fs photoinduced spin crossover in $[Fe(bpy)_3]^{2+}$.* Nature Chemistry, 2015. **7**: p. 629-633.

73. Field, R., et al., *Spectral Signatures of Ultrafast Spin Crossover in Single Crystal $[Fe^{II}(bpy)_3](PF_6)_2$.* Chemistry-a European Journal, 2016. **22**(15): p. 5118-5122.

74. Gawelda, W., et al., *Structural Determination of a Short-Lived Excited Iron(II) Complex by Picosecond X-Ray Absorption Spectroscopy.* Physical Review Letters, 2007. **98**: p. 057401.

75. Bressler, C., et al., *Femtosecond XANES Study of the Light-Induced Spin Crossover Dynamics in an Iron(II) Complex.* Science, 2009. **323**: p. 489-492.

76. Lemke, H.T., et al., *Femtosecond X-ray Absorption Spectroscopy at a Hard X-ray Free Electron Laser: Application to Spin Crossover Dynamics.* The Journal of Physical Chemistry A, 2013. **117**: p. 735-740.

77. Freyer, B., et al., *Ultrafast inter-ionic charge transfer of transition-metal complexes mapped by femtosecond X-ray powder diffraction.* J Chem Phys, 2013. **138**(14): p. 144504.

78. Bressler, C., et al., *Solvation dynamics monitored by combined X-ray spectroscopies and scattering: photoinduced spin transition in aqueous* $[Fe(bpy)_3]^{2+}$. Faraday Discussions, 2014. **171**: p. 169-178.

79. Zhang, W., et al., *Tracking excited-state charge and spin dynamics in iron coordination complexes.* Nature, 2014. **509**: p. 345-348.

80. Hong, K., et al., *Element-Specific Characterization of Transient Electronic Structure of Solvated Fe(II) Complexes with Time-Resolved Soft X-ray Absorption Spectroscopy.* Accounts of Chemical Research, 2015. **48**(11): p. 2957–2966.

81. Lawson Daku, L.M. and A. Hauser, *Ab Initio Molecular Dynamics Study of an Aqueous Solution of* $[Fe(bpy)_3](Cl)_2$ *in the Low-Spin and in the High-Spin States.* The Journal of Physical Chemistry Letters, 2010. **1**: p. 1830-1835.

82. Sousa, C., et al., *Ultrafast Deactivation Mechanism of the Excited Singlet in the Light-Induced Spin Crossover of* $[Fe(2,2'\text{-bipyridine})_3]^{2+}$. Chemistry – A European Journal, 2013. **19**: p. 17541-17551.

83. Domingo, A., C. Sousa, and C.d. Graaf, *The effect of thermal motion on the electron localization in metal-to-ligand charge transfer excitations in* $[Fe(bpy)_3]^{2+}$. Dalton Transactions, 2014. **43**: p. 17838-17846.

84. Iuchi, S. and N. Koga, *An improved model electronic Hamiltonian for potential energy surfaces and spin-orbit couplings of low-lying d-d states of* $[Fe(bpy)_3]^{2+}$. Journal of Chemical Physics, 2014. **140**(2): p. 024309.

85. Das, A.K., et al., *Inner-Shell Water Rearrangement Following Photoexcitation of Tris(2,2 '-bipyridine)iron(II).* Journal of Physical Chemistry B, 2016. **120**(1): p. 206-216.

86. Hannay, C., et al., *X-ray absorption spectroscopic study of the temperature and pressure dependence of the electronic spin states in several iron(II) and cobalt(II) tris(pyrazolyl)borate complexes.* Inorganic Chemistry, 1997. **36**(24): p. 5580-5588.

87. Yokoyama, T., et al., *Spin-crossover phase transition of a chain Fe(II) complex studied by x-ray-absorption fine-structure spectroscopy.* Physical Review B, 1998. **58**(21): p. 14238-14244.

88. van Koningsbruggen, P.J., et al., *Synthesis, crystal structure, EXAFS, and magnetic properties of catena [μ-tris(1,2-bis(tetrazol-1-yl)propane-N1,N1') iron(II)] bis(perchlorate). First crystal structure of an iron(II) spin-crossover chain compound.* Inorganic Chemistry, 2000. **39**(9): p. 1891-1900.

89. Kusz, J., H. Spiering, and P. Gütlich, *X-ray structure study of the light-induced metastable states of the spin-crossover compound $[Fe(mtz)_6](BF_4)_2$.* Journal of Applied Crystallography, 2001. **34**: p. 229-238.

90. MacLean, E.J., et al., *Structural study of the thermal and photochemical spin states in the spin crossover complex $[Fe(phen)_2(NCSe)_2]$*. Chemistry-a European Journal, 2003. **9**(21): p. 5314-5322.

91. Okamoto, K., et al., *XAFS study on the photoinduced spin transition of $[Fe(2\text{-}pic)_3]Cl_2 \cdot C_2H_5OH$.* Chemical Physics Letters, 2003. **371**(5-6): p. 707-712.

92. Thompson, A.L., et al., *Thermal and light induced polymorphism in iron(II) spin crossover compounds.* Chemical Communications, 2004(12): p. 1390-1391.

93. Hostettler, M., et al., *Challenges in engineering spin crossover: Structures and magnetic properties of six alcohol solvates of iron(II) tris(2-picolylamine) dichloride.* Angewandte Chemie-International Edition, 2004. **43**(35): p. 4589-4594.

94. Oyanagi, H., T. Tayagaki, and K. Tanaka, *Photo-induced phase transitions probed by X-ray absorption spectroscopy: Fe(II) spin crossover complex.* Journal of Physics and Chemistry of Solids, 2004. **65**(8-9): p. 1485-1489.

95. Kusz, J., et al., *The LIESST state of $[Fe(pic)_3]Cl_2 \cdot EtOH$ - the superstructure under continuous irradiation.* Journal of Applied Crystallography, 2005. **38**: p. 528-536.

96. Oyanagi, H., T. Tayagaki, and K. Tanaka, *Synchrotron radiation study of photo-induced spin-crossover transitions: Microscopic origin of nonlinear phase transition.* Journal of Luminescence, 2006. **119**: p. 361-369.

97. Khalil, M., et al., *Picosecond X-ray absorption spectroscopy of a photoinduced iron(II) spin crossover reaction in solution.* Journal of Physical Chemistry A, 2006. **110**(1): p. 38-44.

98. Cannizzo, A., et al., *Light-induced spin crossover in Fe(II)-based complexes: The full photocycle unraveled by ultrafast optical and X-ray spectroscopies.* Coordination Chemistry Reviews, 2010. **254**: p. 2677-2686.

99. Alfano, R.R. and S.L. Shapiro, *Observation of Self-Phase Modulation and Small-Scale Filaments in Crystals and Glasses.* Physical Review Letters, 1970. **24**(11): p. 592-594.

100. Fork, R.L., et al., *Femtosecond white-light continuum pulses.* Optics Letters, 1983. **8**(1): p. 1-3.

101. Cerullo, G. and S. De Silvestri, *Ultrafast optical parametric amplifiers.* Review of Scientific Instruments, 2003. **74**(1): p. 1-18.

102. Kovalenko, S.A., et al., *Femtosecond spectroscopy of condensed phases with chirped supercontinuum probing.* Physical Review A, 1999. **59**(3): p. 2369-2384.

103. Dobryakov, A.L., et al., *Femtosecond pump/supercontinuum-probe spectroscopy: Optimized setup and signal analysis for single-shot spectral referencing.* Review of Scientific Instruments, 2010. **81**(11): p. 113106.

104. New, G., *Introduction to Nonlinear Optics*. 2011, Cambridge: University Press.

105. Burnett, N.H., et al., *Harmonic-Generation in CO_2-Laser Target Interaction.* Applied Physics Letters, 1977. **31**(3): p. 172-174.

106. Mcpherson, A., et al., *Studies of Multiphoton Production of Vacuum Ultraviolet-Radiation in the Rare-Gases.* Journal of the Optical Society of America B-Optical Physics, 1987. **4**(4): p. 595-601.

107. Ferray, M., et al., *Multiple-Harmonic Conversion of 1064 nm Radiation in Rare-Gases.* Journal of Physics B-Atomic Molecular and Optical Physics, 1988. **21**(3): p. L31-L35.

108. Arpin, P., et al., *Enhanced High Harmonic Generation from Multiply Ionized Argon above 500 eV through Laser Pulse Self-Compression.* Physical Review Letters, 2009. **103**(14): p. 143901.

109. Rullière, C., *Femtosecond laser pulses : principles and experiments*. 2nd ed. Advanced texts in physics,. 2005, New York: Springer. 426 pp.

110. Pfeifer, T., C. Spielmann, and G. Gerber, *Femtosecond x-ray science.* Reports on Progress in Physics, 2006. **69**: p. 443.

111. Keldysh, L.V., *Ionization in Field of a Strong Electromagnetic Wave.* Soviet Physics JETP-USSR, 1965. **20**(5): p. 1307-1314.

112. Suga, S. and A. Sekiyama, *Photoelectron spectroscopy: bulk and surface electronic structures*. 2014: Springer-Verlag Berlin Heidelberg. 378 pp.

113. Hüfner, S., *Photoelectron spectroscopy: principles and applications*. 2003: Springer-Verlag Berlin Heidelberg. 662 pp.

114. Winter, B. and M. Faubel, *Photoemission from Liquid Aqueous Solutions.* Chemical Reviews, 2006. **106**: p. 1176-1211.

115. Olivieri, G., et al., *Quantitative ionization energies and work functions of aqueous solutions.* Phys Chem Chem Phys, 2016. **18**(42): p. 29506-29515.

116. Lindle, D.W. and O.A. Hemmers, *Time-of-flight photoelectron spectroscopy of atoms and molecules.* Journal of Alloys and Compounds, 2001. **328**(1-2): p. 27-34.

117. Hemmers, O., et al., *High-resolution electron time-of-flight apparatus for the soft x-ray region.* Review of Scientific Instruments, 1998. **69**(11): p. 3809-3817.

118. Kothe, A., et al., *Time-of-flight electron spectrometer for a broad range of kinetic energies.* The Review of Scientific Instruments, 2013. **84**: p. 023106.

119. Morgenstern, R., A. Niehaus, and M.W. Ruf, *Angular distributions of photoelectrons.* Chemical Physics Letters, 1970. **4**(10): p. 635-638.

120. Thürmer, S., et al., *Photoelectron Angular Distributions from Liquid Water: Effects of Electron Scattering.* Physical Review Letters, 2013. **111**(17).

121. Cavalieri, A.L., et al., *Attosecond spectroscopy in condensed matter.* Nature, 2007. **449**(7165): p. 1029-1032.

122. Wu, G., P. Hockett, and A. Stolow, *Time-resolved photoelectron spectroscopy: from wavepackets to observables.* Phys Chem Chem Phys, 2011. **13**(41): p. 18447-67.

123. Marsi, M., et al., *Transient charge carrier distribution at UV-photoexcited SiO_2/Si interfaces.* Physical Review B, 2000. **61**(8): p. R5070-R5073.

124. Spencer, B.F., et al., *Time-resolved surface photovoltage measurements at n-type photovoltaic surfaces: Si(111) and ZnO(10$\bar{1}$0).* Physical Review B, 2013. **88**(19): p. 195301.

125. Villeneuve, D.M., et al., *Space charge and plasma effects in zero kinetic energy (ZEKE) photoelectron spectroscopy.* Journal of Chemical Physics, 1997. **107**(14): p. 5310-5318.

126. Hellmann, S., et al., *Vacuum space-charge effects in solid-state photoemission.* Physical Review B, 2009. **79**(3): p. 035402.

127. Passlack, S., et al., *Space charge effects in photoemission with a low repetition, high intensity femtosecond laser source.* Journal of Applied Physics, 2006. **100**(2): p. 024912.

128. Zhou, X.J., et al., *Space charge effect and mirror charge effect in photoemission spectroscopy.* Journal of Electron Spectroscopy and Related Phenomena, 2005. **142**(1): p. 27-38.

129. Siffalovic, P., M. Drescher, and U. Heinzmann, *Femtosecond time-resolved core-level photoelectron spectroscopy tracking surface photovoltage transients on p-GaAs.* Europhysics Letters, 2002. **60**(6): p. 924-930.

130. Frietsch, B., et al., *A high-order harmonic generation apparatus for time- and angle-resolved photoelectron spectroscopy.* Review of Scientific Instruments, 2013. **84**(7): p. 075106.

131. Hellmann, S., et al., *Time-resolved x-ray photoelectron spectroscopy at FLASH.* New Journal of Physics, 2012. **14**: p. 013062.

132. Oloff, L.P., et al., *Time-resolved HAXPES at SACLA: probe and pump pulse-induced space-charge effects.* New Journal of Physics, 2014. **16**: p. 123045.

133. Al-Obaidi, R., et al., *Ultrafast photoelectron spectroscopy of solutions: space-charge effect.* New Journal of Physics, 2015. **17**: p. 093016.

134. Siwick, B.J., et al., *Ultrafast electron optics: Propagation dynamics of femtosecond electron packets.* Journal of Applied Physics, 2002. **92**(3): p. 1643-1648.

135. Pietzsch, A., et al., *Towards time resolved core level photoelectron spectroscopy with femtosecond x-ray free-electron lasers.* New Journal of Physics, 2008. **10**: p. 033004.

136. Reed, B.W., *Femtosecond electron pulse propagation for ultrafast electron diffraction.* Journal of Applied Physics, 2006. **100**(3): p. 034916.

137. Collin, S., et al., *Transverse and longitudinal space-charge-induced broadenings of ultrafast electron packets.* Journal of Applied Physics, 2005. **98**(9): p. 094910.

138. Saathoff, G., et al., *Laser-assisted photoemission from surfaces.* Physical Review A, 2008. **77**: p. 022903.

139. Petite, G., et al., *Origin of the High-Energy Electron-Emission from Metals under Laser Irradiation.* Physical Review B, 1992. **45**(21): p. 12210-12217.

140. Muller, H.G., H.B.V. Vandenheuvell, and M.J. Vanderwiel, *Dressing of Continuum States after MPI of Xe in a 2-Color Experiment.* Journal of Physics B-Atomic Molecular and Optical Physics, 1986. **19**(21): p. L733-L739.

141. Agostini, P., et al., *Free-Free Transitions Following Six-Photon Ionization of Xenon Atoms.* Physical Review Letters, 1979. **42**(17): p. 1127-1130.

142. Eberly, J.H. and J. Javanainen, *Above-threshold ionisation.* European Journal of Physics, 1988. **9**(4): p. 265.

143. Freeman, R.R. and P.H. Bucksbaum, *Investigations of above-Threshold Ionization Using Subpicosecond Laser-Pulses.* Journal of Physics B-Atomic Molecular and Optical Physics, 1991. **24**(2): p. 325-347.

144. Paulus, G.G., W. Nicklich, and H. Walther, *Investigation of Above-Threshold Ionization with Femtosecond Pulses: Connection Between Plateau and Angular Distribution of the Photoelectrons.* EPL (Europhysics Letters), 1994. **27**(4): p. 267.

145. Parker, J. and C.W. Clark, *Study of a plane-wave final-state theory of above-threshold ionization and harmonic generation.* Journal of the Optical Society of America B, 1996. **13**(2): p. 371-379.

146. Becker, W., et al., *Above-threshold ionization: From classical features to quantum effects.* Advances in Atomic, Molecular, and Optical Physics, Vol 48, 2002. **48**: p. 35-98.

147. Milošević, D.B., et al., *Above-threshold ionization by few-cycle pulses.* Journal of Physics B: Atomic, Molecular and Optical Physics, 2006. **39**(14): p. R203.

148. Nakajima, T. *Chirp-Dependent Above-Threshold Ionization*. in *2007 Conference on Lasers and Electro-Optics (CLEO)*. 2007.

149. Blaga, C.I., et al., *Strong-field photoionization revisited.* Nat Phys, 2009. **5**(5): p. 335-338.

150. Suárez, N., et al., *Above-threshold ionization and photoelectron spectra in atomic systems driven by strong laser fields.* Physical Review A, 2015. **92**(6): p. 063421.

151. DiMauro, L.F. and P. Agostini, *Ionization Dynamics in Strong Laser Fields.* Advances in Atomic Molecular and Optical Physics, 1995. **35**: p. 79-120.

152. Glover, T.E., et al., *Observation of Laser Assisted Photoelectric Effect and Femtosecond High Order Harmonic Radiation.* Physical Review Letters, 1996. **76**: p. 2468-2471.

153. Hayden, P., et al., *The Laser-assisted photoelectric effect of He, Ne, Ar and Xe in intense extreme ultraviolet and infrared laser fields.* Journal of Modern Optics, 2016. **63**(4): p. 358-366.

154. Miaja-Avila, L., et al., *Laser-Assisted Photoelectric Effect from Surfaces.* Physical Review Letters, 2006. **97**: p. 113604.

155. Miaja-Avila, L., et al., *Ultrafast studies of electronic processes at surfaces using the laser-assisted photoelectric effect with long-wavelength dressing light.* Physical Review A, 2009. **79**: p. 030901.

156. Winter, B., *Liquid microjet for photoelectron spectroscopy.* Nuclear Instruments and Methods in Physics Research Section A: Accelerators, Spectrometers, Detectors and Associated Equipment, 2009. **601**: p. 139-150.

157. Faubel, M., B. Steiner, and J.P. Toennies, *Photoelectron spectroscopy of liquid water, some alcohols, and pure nonane in free micro jets.* The Journal of Chemical Physics, 1997. **106**: p. 9013-9031.

158. Lange, K.M., A. Kothe, and E.F. Aziz, *Chemistry in solution: recent techniques and applications using soft X-ray spectroscopy.* Physical Chemistry Chemical Physics, 2012. **14**(16): p. 5331-5338.

159. Siegbahn, H., *Electron-Spectroscopy for Chemical-Analysis of Liquids and Solutions.* Journal of Physical Chemistry, 1985. **89**(6): p. 897-909.

160. Jablonski, A. and C.J. Powell, *Relationships between electron inelastic mean free paths, effective attenuation lengths, and mean escape depths.* Journal of Electron Spectroscopy and Related Phenomena, 1999. **100**: p. 137-160.

161. Jablonski, A. and C.J. Powell, *The electron attenuation length revisited.* Surface Science Reports, 2002. **47**(2-3): p. 35-91.

162. Ottosson, N., et al., *Photoelectron spectroscopy of liquid water and aqueous solution: Electron effective attenuation lengths and emission-angle anisotropy.* Journal of Electron Spectroscopy and Related Phenomena, 2010. **177**(2-3): p. 60-70.

163. Suzuki, Y.I., et al., *Effective attenuation length of an electron in liquid water between 10 and 600 eV.* Physical Review E, 2014. **90**(1): p. 010302.

164. Moulton, P., *Ti-doped sapphire: tunable solid-state laser.* Optics News, 1982. **8**(6): p. 9-9.

165. Moulton, P., *Spectroscopic and laser characteristics of Ti:Al_2O_3.* Journal of the Optical Society of America B, 1986. **3**(1): p. 125-133.

166. Spence, D.E., P.N. Kean, and W. Sibbett, *60-fsec pulse generation from a self-mode-locked Ti:sapphire laser.* Optics Letters, 1991. **16**(1): p. 42-44.

167. Aristov, V.V., A.I. Erko, and V.V. Martynov, *Principles of Bragg-Fresnel Multilayer Optics.* Revue De Physique Appliquee, 1988. **23**(10): p. 1623-1630.

168. Metje, J., et al., *Monochromatization of femtosecond XUV light pulses with the use of reflection zone plates.* Optics Express, 2014. **22**(9): p. 10747-10760.

169. Metje, J., *Development and Application of a XUV Laser Light Source for Photoelectron Spectroscopy of Solutions*. 2017, doctoral thesis, Freie Universität Berlin.

170. Yamada, C., H. Kanamori, and E. Hirota, *Direct observation of the fine structure transitions in the Ne^+ and Ar^+ ions with diode lasers.* The Journal of Chemical Physics, 1985. **83**(2): p. 552-555.

171. Arrell, C.A., et al., *Laser-Assisted Photoelectric Effect from Liquids.* Physical Review Letters, 2016. **117**(14): p. 143001.

172. Kaindl, R.A., et al., *Generation, shaping, and characterization of intense femtosecond pulses tunable from 3 to 20 μm.* Journal of the Optical Society of America B, 2000. **17**(12): p. 2086-2094.

173. Demirdöven, N., et al., *Dispersion compensation with optical materials for compression of intense sub-100-fs mid-infrared pulses.* Optics Letters, 2002. **27**(6): p. 433-435.

174. Kozich, V., A. Moguilevski, and K. Heyne, *High energy femtosecond OPA pumped by 1030nm Yb:KGW laser.* Optics Communications, 2012. **285**(21): p. 4515-4518.

175. Petrov, V., *Frequency down-conversion of solid-state laser sources to the mid-infrared spectral range using non-oxide nonlinear crystals.* Progress in Quantum Electronics, 2015. **42**: p. 1-106.

176. Moguilevski, A., et al., *Ultrafast Spin Crossover in $[Fe^{II}(bpy)_3]^{2+}$: Revealing Two Competing Mechanisms by Extreme Ultraviolet Photoemission Spectroscopy.* ChemPhysChem, 2017. **18**(5): p. 465-469.

177. Winter, B., et al., *Full Valence Band Photoemission from Liquid Water Using EUV Synchrotron Radiation.* The Journal of Physical Chemistry A, 2004. **108**: p. 2625-2632.

178. Seidel, R., B. Winter, and S. Bradforth, *Valence Electronic Structure of Aqueous Solutions: Insights from Photoelectron Spectroscopy.* Annu Rev Phys Chem, 2016. **67**: p. 283-305.

179. Kurahashi, N., et al., *Photoelectron spectroscopy of aqueous solutions: Streaming potentials of NaX (X = Cl, Br, and I) solutions and electron binding*

energies of liquid water and X^-. The Journal of Chemical Physics, 2014. **140**: p. 174506.

180. Nishizawa, K., et al., *High-resolution soft X-ray photoelectron spectroscopy of liquid water.* Physical Chemistry Chemical Physics, 2010. **13**: p. 413-417.

181. Nordlund, D., et al., *Electronic structure effects in liquid water studied by photoelectron spectroscopy and density functional theory.* Chemical Physics Letters, 2008. **460**: p. 86-92.

182. Potts, A.W. and W.C. Price, *Photoelectron Spectra and Valence Shell Orbital Structures of Groups V and VI Hydrides.* Proceedings of the Royal Society of London Series a-Mathematical and Physical Sciences, 1972. **326**(1565): p. 181-197.

183. Sansonetti, J.E. and W.C. Martin, *Handbook of basic atomic spectroscopic data.* Journal of Physical and Chemical Reference Data, 2005. **34**(4): p. 1559-2259.

184. Preissler, N., et al., *Electrokinetic Charging and Evidence for Charge Evaporation in Liquid Microjets of Aqueous Salt Solution.* The Journal of Physical Chemistry B, 2013. **117**: p. 2422-2428.

185. Seidel, R., et al., *Valence Photoemission Spectra of Aqueous $Fe^{2+/3+}$ and $[Fe(CN)_6]^{4-/3-}$ and Their Interpretation by DFT Calculations.* Journal of Physical Chemistry B, 2011. **115**(40): p. 11671-11677.

186. Siefermann, K.R., et al., *Binding energies, lifetimes and implications of bulk and interface solvated electrons in water.* Nature Chemistry, 2010. **2**: p. 274-279.

187. Fita, P., et al., *Chemistry, photophysics, and ultrafast kinetics of two structurally related Schiff bases containing the naphthalene or quinoline ring.* The Journal of Chemical Physics, 2006. **125**(18): p. 184508.

188. Landau, L.D. and E.M. Lifshitz, *Quantum Mechanics: Non-Relativistic Theory*. 1977, Oxford: Pergamon Press. 688 pp.

189. Kepenekian, M., V. Robert, and B. Le Guennic, *What zeroth-order Hamiltonian for CASPT2 adiabatic energetics of $Fe(II)N_6$ architectures?* The Journal of Chemical Physics, 2009. **131**(11): p. 114702.

190. Bokarev, S.I., O.S. Bokareva, and O. Kühn, *Electronic excitation spectrum of the photosensitizer $[Ir(ppy)_2(bpy)]^+$*. The Journal of Chemical Physics, 2012. **136**(21): p. 214305.

191. Fushitani, M. and A. Hishikawa, *Single-order laser high harmonics in XUV for ultrafast photoelectron spectroscopy of molecular wavepacket dynamics.* Structural Dynamics, 2016. **3**(6): p. 062602.

192. Engel, N., et al., *Light-induced relaxation dynamics of the ferricyanide ion revisited by ultrafast XUV photoelectron spectroscopy.* Physical Chemistry Chemical Physics, 2017. **19**(22): p. 14248-14255.

193. Raheem, A.A., et al., *Ultrafast kinetics of linkage isomerism in $Na_2[Fe(CN)_5NO]$ aqueous solution revealed by time-resolved photoelectron spectroscopy.* Structural Dynamics, 2017. **4**(4): p. 044031.

194. Gurentsov, E.V. and A.V. Eremin, *Synthesis of metal-carbon nanoparticles in pulsed UV-photolysis of $Fe(CO)_5$-CCl_4 mixtures at room temperature.* Technical Physics Letters, 2015. **41**(6): p. 547-550.

195. Whetten, R.L., K.J. Fu, and E.R. Grant, *Photodissociation dynamics of $Fe(CO)_5$: Excited state lifetimes and energy disposal.* The Journal of Chemical Physics, 1983. **79**(10): p. 4899-4911.

196. Bañares, L., et al., *Femtosecond photodissociation dynamics of $Fe(CO)_5$ in the gas phase.* Chemical Physics Letters, 1997. **267**(1): p. 141-148.

197. Bañares, L., et al., *The ultrafast photodissociation of $Fe(CO)_5$ in the gas phase.* The Journal of Chemical Physics, 1998. **108**(14): p. 5799-5811.

198. Trushin, S.A., et al., *Femtosecond Dynamics of $Fe(CO)_5$ Photodissociation at 267 nm Studied by Transient Ionization.* The Journal of Physical Chemistry A, 2000. **104**(10): p. 1997-2006.

199. Ihee, H., J.M. Cao, and A.H. Zewail, *Ultrafast electron diffraction of transient $[Fe(CO)_4]$: Determination of molecular structure and reaction pathway.* Angewandte Chemie-International Edition, 2001. **40**(8): p. 1532-1536.

200. Wernet, P., et al., *Communication: Direct evidence for sequential dissociation of gas-phase $Fe(CO)_5$ via a singlet pathway upon excitation at 266 nm.* The Journal of Chemical Physics, 2017. **146**(21): p. 211103.

201. Snee, P.T., et al., *Triplet Organometallic Reactivity under Ambient Conditions: An Ultrafast UV Pump/IR Probe Study.* Journal of the American Chemical Society, 2001. **123**(10): p. 2255-2264.

202. Snee, P.T., et al., *Dynamics of Photosubstitution Reactions of $Fe(CO)_5$: An Ultrafast Infrared Study of High Spin Reactivity.* Journal of the American Chemical Society, 2001. **123**(28): p. 6909-6915.

203. Ahr, B., et al., *Picosecond X-ray absorption measurements of the ligand substitution dynamics of $Fe(CO)_5$ in ethanol.* Physical Chemistry Chemical Physics, 2011. **13**(13): p. 5590-5599.

204. Wernet, P., et al., *Orbital-specific mapping of the ligand exchange dynamics of $Fe(CO)_5$ in solution.* Nature, 2015. **520**(7545): p. 78-81.

205. Kotzian, M., et al., *Optical spectra of transition-metal carbonyls: chromium hexacarbonyl, iron pentacarbonyl, and nickel tetracarbonyl.* Journal of the American Chemical Society, 1989. **111**(20): p. 7687-7696.

List of publications

1. N. Engel, S.I. Bokarev, A. Moguilevski, A. Raheem, R. Al-Obaidi, T. Möhle, G. Grell, K.R. Siefermann, B. Abel, S.G. Aziz, O. Kühn, M. Borgwardt, I.Yu. Kiyan, and E.F. Aziz
   „Light-induced Relaxation Dynamics of the Ferricyanide Ion Revisited by Ultrafast XUV Photoelectron Spectroscopy “.
   Physical Chemistry Chemical Physics, 19, 14248-14255, (2017).
   DOI: 10.1039/c7cp01288h

2. A. Moguilevski, M. Wilke, G. Grell, S.I. Bokarev, S.G. Aziz, N. Engel, A. Raheem, O. Kühn, I.Yu. Kiyan, and E.F. Aziz
   „Ultrafast Spin Crossover in $[Fe^{II}(bpy)_3]^{2+}$: Revealing Two Competing Mechanisms by Extreme Ultraviolet Photoemission Spectroscopy“.
   ChemPhysChem, 18, 465-469, (2017).
   DOI: 10.1002/cphc.201601396

3. R. Al-Obaidi, M. Wilke, M. Borgwardt, J. Metje, A. Moguilevski, N. Engel, D. Tolksdorf, A. Raheem, T. Kampen, S. Mähl, I.Yu. Kiyan and E.F. Aziz
   „Ultrafast Photoelectron Spectroscopy of Solutions: Space-Charge Effect“.
   New Journal of Physics, 17, 093016, (2015).
   DOI: 10.1088/1367-2630/17/9/093016

4. A. Kothe, M. Wilke, A. Moguilevski, N. Engel, B. Winter, I.Y. Kiyan, and E.F. Aziz.
   Comment on „Charge Transfer to Solvent Dynamics in Iodide Aqueous Solution Studied at Ionization Threshold“.
   Physical Chemistry Chemical Physics, 17, 18193-18194, (2015).
   DOI: 10.1039/c5cp00346f

5. A. Kothe, M. Wilke, A. Moguilevski, N. Engel, B. Winter, I.Y. Kiyan und E.F. Aziz.
   „Charge Transfer to Solvent Dynamics in Iodide Aqueous Solution Studied at Ionization Threshold“.
   Physical Chemistry Chemical Physics, 17, 1918-1924, (2015).
   DOI: 10.1039/c4cp02482f

6. M. Wilke, R. Al-Obaidi, A. Moguilevski, A. Kothe, N. Engel, J. Metje, I. Yu Kiyan, and E. F. Aziz.
„Laser-Assisted Electron Scattering in Strong-Field Ionization of Dense Water Vapor by Ultrashort Laser Pulses“.
New Journal of Physics, 16, 083032, (2014).
DOI: 10.1088/1367-2630/16/8/083032

7. J. Metje, M. Borgwardt, A. Moguilevski, A. Kothe, N. Engel, M. Wilke, R. Al-Obaidi, D. Tolksdorf, A. Firsov, M. Brzhezinskaya, A. Erko, I.Yu. Kiyan, and E.F. Aziz
„Monochromatization of Femtosecond XUV Light Pulses with the Use of Reflection Zone Plates“.
Optics Express, 22, 10747-10760, (2014).
DOI: 10.1364/OE.22.010747

8. A. Kothe, J. Metje, M. Wilke, A. Moguilevski, N. Engel, R. Al-Obaidi, C. Richter, R. Golnak, I.Yu. Kiyan, and E.F. Aziz
„Time-of-Flight Electron Spectrometer for a Broad Range of Kinetic Energies“.
The Review of Scientific Instruments, 84, 023106, (2013).
DOI: 10.1063/1.4791792

9. V. Kozich, A. Moguilevski, and K. Heyne.
„High Energy Femtosecond OPA Pumped by 1030 nm Yb:KGW Laser.“
Optics Communications, 285, 4515-4518, (2012).
DOI: 10.1016/j.optcom.2012.06.077

Abstract

Tracking electron dynamics after photoexcitation is a key element in understanding the mechanisms of light-induced spin crossover (SCO) in condensed-phase transition metal complexes. This effect is of fundamental interest in biology and finds applications in magnetic data storage and the development of functional molecular devices. Following excitation, the large number of accessible excited states and ultrafast kinetics of their relaxation pose stringent experimental requirements for the elucidation of the SCO pathways. This challenge might lead to ambiguous interpretations on the basis of absorption and fluorescence spectroscopies alone, which do not provide unique excitation energy references in ultrafast dynamics studies. A prominent example is the iron(II) tris-bipyridine complex, $[Fe(bpy)_3]^{2+}$. Recently, different detection techniques have yielded controversial results regarding whether the transition from the singlet to the quintet spin state is a direct or a stepwise process involving the triplet ligand field states. In this thesis, it will be demonstrated that ultrafast extreme ultraviolet (XUV) photoemission spectroscopy (PES) in combination with the liquid microjet technique, supported by the theoretical calculations, is capable of tracking the population dynamics of the electronically excited states of aqueous $[Fe(bpy)_3]^{2+}$ with femtosecond time resolution. Mapping the transient electronic states onto the ionization continuum with the use of ultrashort XUV light pulses from a monochromotized, table-top high-order harmonic generation (HHG) setup, it was possible to unambiguously follow the excitation dynamics on an absolute energy scale. This approach revealed both sequential and direct de-excitation pathways from the electronically excited singlet to quintet states, with a branching ratio that was determined to be 4.5:1, respectively. This novel methodology can be widely applied in chemical sciences to track the energy- and time-resolved electron dynamics that occur in condensed-phase molecular complexes following photoexcitation.

Kurzzusammenfassung

Die Verfolgung der Elektronendynamik nach einer Photoanregung ist ein Schlüssel zum Verständnis des Mechanismus von optisch induzierten Spinübergängen (bekannt als Spin Crossover) in den Übergangsmetallkomplexen in festen und flüssigen Aggregatzuständen. Dieser Effekt stellt das grundlegende Interesse für Biologie und Geologie dar. Außerdem hat das Spin Crossover vielversprechende Perspektiven in der Anwendung des Effekts für die magnetische Datenspeicherung und die Entwicklung molekularer Maschinen. Die Anregung mit Licht führt zu einer großen Zahl möglicher elektronischer Zustände, die eine Spin-Crossover-Molekül auf den darauffolgenden ultraschnellen Relaxationswegen annehmen kann. Die Aufklärung dieser Relaxationskanäle stellt strenge experimentelle Anforderungen. Diese komplizierte Aufgabe kann allein auf der Basis von Absorptions- und Fluoreszenzspektroskopie zu unterschiedlichen Interpretationen führen, weil diese Methoden über keine eindeutigen Referenzen auf die Energieskala verfügen. Ein herausragendes Beispiel dafür stellt Esen(II) Tris-Bipyridin ($[Fe(bpy)_3]^{2+}$) dar. Kürzlich lieferte die Anwendung von unterschiedlichen Spektroskopiemethoden kontroverse Ergebnisse bezüglich der Frage, ob der Übergang vom Singulett- zum Quintett-Spin-Zustand direkt oder stufenweise über die Triplett-Ligandenfeld-Zwischenzustände erfolgt. In dieser Dissertation wurde demonstriert, dass die auf der extrem ultravioletten (XUV) Strahlung basierende ultraschnelle Photoelektronenspektroskopie in Kombination mit der Liquid-Microjet-Technik und mit Unterstützung von theoretischen Berechnungen für die Verfolgung der Populationsdynamik von elektronisch-angeregten Zuständen vom in Wasser gelösten $[Fe(bpy)_3]^{2+}$ mit der zeitlichen Auflösung im Femtosekundenbereich geeignet ist. Die Übertragung von transienten elektronischen Zuständen ins Ionisationskontinuum mithilfe ultrakurze XUV Laserpulse, die in einem monochromatisiertem Tisch-Setup zur Erzeugung von höhen Harmonischen (HHG) produziert wurden, ermöglichte der Elektronendynamik auf einer absoluten Energieskala genau zu folgen. Dieser Ansatz hat die Präsenz von beiden, sequentiellen und direkten, Relaxationskanälen im Verhältnis von 4.5 zu 1 aufgedeckt. Diese neuartige Methodik kann weithin in der physikalisch-chemischen Forschung zur Verfolgung der energie- und zeitaufgelösten Elektronendynamik, die durch Photoanregung in der kondensierten Materie entsteht, angewendet werden.

Acknowledgements

I would like to express deepest gratitude and my special appreciations to…

Prof. Dr. Karsten Heyne for his willingness to be my first supervisor and to evaluate my thesis, for scientific consultations as well as for his good advices.

Dr. Iain Wilkinson for the willingness to be my second supervisor and to evaluate my thesis, for helpfulness and for sharing his knowledge with me as well as for the support in the iron-pentacarbonyl experiment.

Prof. Dr. Emad Aziz for the opportunity to make this scientific study, for giving me motivation during the time in the Helmholtz-Zentrum Berlin and for excellent laboratory equipment which largely contributed to the success of the experimental work.

Dr. Igor Kiyan for co-supervising my thesis, excellent care of our laboratory at FU and sharing his huge scientific experience with me and other co-workers.

Dr. Valeri Kozich for advice and support in the field of nonlinear optics and for the practical skills and knowledge, which I gained during my diploma work.

Dr. Martin Wilke for helpfulness, kindness, exchange of ideas, introduction to Mathematica, and support in data analysis.

Nicholas Engel for countless hours, which we spent working together at the experimental setup.

Prof. Dr. Oliver Kühn, **Dr. Sergey Bokarev**, and **Gilbert Grell** from the Rostock University for collaboration in the study of the spin crossover in iron-tris-bipyridine and for scientific consultations.

Furthermore, I want to thank for the technical support and for the useful advises my colleagues from the FU team:

Dr. Mario Borgwardt, Dr. Jan Metje, Dr. Alexander Kothe, Daniel Tolksdorf, Karen Mudryk, Dr. Ruba Al-Obaidi, Azhr A. Raheem, Dr. Christoph Merschjann,

and my colleagues from the synchrotron team:

Dr. Bernd Winter, Dr. Kaan Atak, Dr. Robert Seidel, Dr. Ronny Golnak, Dr. Jie Xiao, Dr. Tim Brandenburg, Dr. Tristan Petit, Dr. Franziska Büchner, Dr. Isaak Unger.

It was a pleasure to work and to celebrate together with all of you.

And, last but not least, I want to express a very special gratitude to my Mother, and to Momoko Inadomi, Dr. Helmut Piazena, and all my friends for being there and for supporting me in the years of my promotion at FU Berlin.

Selbstständigkeitserklärung

Ich erkläre gegenüber der Freien Universität Berlin, dass ich die vorliegende Dissertation selbstständig und ohne Benutzung anderer als der angegebenen Quellen und Hilfsmittel angefertigt habe.

Die vorliegende Arbeit ist frei von Plagiaten. Diese Arbeit wurde in gleicher oder ähnlicher Form noch bei keiner anderen Universität als Prüfungsleistung eingereicht und ist auch noch nicht veröffentlicht.

Alexandre Moguilevski
Berlin, den 09.11.2017